Studies of the ATLAS Muon Spectrometer with testbeam and simulated physics data

A thesis submitted to the Aristotle University of Thessaloniki
for the degree of Doctor of Philosophy

Konstantinos Bachas

June 2008

Department of Physics
Aristotle University of Thessaloniki

Contents

List of Figures

List of Tables

Abstract

In the ATLAS detector, muon related measurements are achieved by a huge Muon Spectrometer installed at the outermost region of the detector. At the LHC energies, high-p_T muons are expected to be measured with a momentum resolution of $\sim 10\%$ at 1 TeV. The main detecting element of the Muon Spectrometer is the Monitored Drift Tube chamber. The reconstruction potential of a BIS type Monitored Drift Tube chamber, in a special setup at the H8 Testbeam experimental area at CERN, is investigated. Data from the BIS muon chamber with both muon and positron beams are taken and the reconstruction of track segments in the chamber is studied. The correlation of the precision coordinate of the reconstructed track segment with the calorimeter cluster barycentre is also studied.

In the ATLAS detector, muons lose parts of their energy in the Calorimetric System before reaching the Muon Spectrometer. As the muon energy increases radiative effects start playing a significant role in the energy loss mechanism and increase the probability for a big muon energy loss, often called as catastrophic. The probability for catastrophic energy losses of 350 GeV muons when they pass through the ATLAS calorimeters is studied with H8 testbeam data.

Information on catastrophic muon energy losses in the calorimeters and also on the isolation of muons can be retrieved by a direct measurement of the calorimeter response. For this reason, a precise energy deposition measurement method in the calorimeters is developed. The method enriches the muon object at the AOD analysis level with information on calorimeter isolation and the collection of calorimeter cells associated with the measurement. The method is applied on single muon and $t\bar{t} \to 4\ell + X$ events.

Finally, the Z boson pair production through the process $pp \to ZZ^{(*)} \to \ell\ell\ell\ell$, where $\ell = e$ or $\ell = \mu$ is of great interest for the LHC physics searches because it constitutes the irreducible background to the observation of the Higgs boson production through the 4 lepton decay. The observation expectations of $pp \to ZZ \to 4\ell$ channel with 1 fb^{-1} of data is investigated and analysis methods on simulated events of signal and $t\bar{t}$ and $Zb\bar{b}$ backgrounds processes are described.

Περίληψη

Στον ανιχνευτή ATLAS, οι μετρήσεις που σχετίζονται με μιόνια πραγματοποιούνται από ένα τεράστιο Μιονικό Φασματόμετρο που βρίσκεται εγκατεστημένο στην εξωτερική περιοχή του ανιχνευτή. Στις ενέργειες του LHC, ακόμα και μιόνια μεγάλης εγκάρσιας ορμής, $\sim 1\ TeV$, αναμένεται να μετρηθούν με διακριτική ικανότητα της τάξης του $\sim 10\%$.

Η βασική ανιχνευτική μονάδα του Μιονικού Φασματόμετρου είναι ο θάλαμος ολίσθησης μιονίων. Μελετάται η ικανότητα ανακατασκευής τροχιών ενός θαλάμου μιονίων τύπου BIS, σε μια ειδική πειραματική διάταξη στην δέσμη ελέγχου H8 στο CERN, με δεδομένα που λήφθηκαν με δέσμες μιονίων και ποζιτρονίων. Επίσης μελετάται η συσχέτιση μεταξύ της συντεταγμένης που μετράται με ακρίβεια της ανακατασκευασμένης τροχιάς όταν προεκταθεί στο θερμιδόμετρο, και του βαρύκεντρου της συστοιχίας κυψελίδων του θερμιδόμετρου από τις οποίες πέρασε το μιόνιο.

Στον ανιχνευτή ATLAS, τα μιόνια χάνουν μέρος της ενέργειας τους στα θερμιδόμετρα πριν φτάσουν στο Μιονικό Φασματόμετρο. Καθώς η ενέργεια των μιονίων αυξάνει, φαινόμενα ακτινοβολίας αρχίζουν να παίζουν σημαντικό ρόλο στον μηχανισμό απώλειας ενέργειας και αυξάνεται η πιθανότητα μεγάλης απώλειας ενέργειας η οποία συχνά αναφέρεται ως 'καταστροφική'. Με δεδομένα από την δέσμη ελέγχου H8, μελετάται η πιθανότητα 'καταστροφικής' απώλειας ενέργειας μιονίων ενέργειας 350 GeV, όταν αυτά διαπερνούν τα θερμιδόμετρα του ATLAS.

Πληροφορίες για 'καταστροφική' απώλεια ενέργειας αλλά και για τον βαθμό απομόνωσης των μιονίων, μπορούν να ληφθούν από απευθείας μέτρηση της απόκρισης του θερμιδόμετρου. Για το λόγο αυτό, αναπτύσσεται μία ακριβής μέθοδος μέτρησης της απόθεσης ενέργειας στα θερμιδόμετρα. Η μέθοδος εμπλουτίζει την ανακατασκευασμένη τροχιά του μιονίου στο επίπεδο ανάλυσης AOD, με πληροφορίες σχετικά με τον βαθμό απομόνωσης του μιονίου από άλλα σωματίδια στα θερμιδόμετρα και με την συλλογή των θερμιδομετρικών κυψελίδων που σχετίζονται με την μέτρηση. Η μέθοδος εφαρμόζεται σε γεγονότα ενός μιονίου και γεγονότα $t\bar{t} \to 4\ell + X$.

Τέλος, η παραγωγή ζεύγους μποζονίων Z μέσω του καναλιού $pp \to ZZ^{(*)} \to \ell\ell\ell\ell$, όπου $\ell = e$ ή μ είναι μεγάλου ενδιαφέροντος για τις μελέτες φυσικής στο LHC γιατί αποτελεί το κυρίως υπόβαθρο με χαρακτηριστικά πανομοιότυπα με το σήμα του μποζονίου Higgs, όταν διασπάται του σε 4 λεπτόνια. Μελετώνται οι προσδοκίες παρατήρησης

To Dina

...for her endless love and support

1 Introduction

The scientific community has, over the last few years, drawn attention to the European Organization for Nuclear Research (CERN) in Geneva, Switzerland, where the construction of the biggest particle physics accelerator of all times is rapidly approaching completion. In the same tunnel that the Large Electron Positron (LEP) was installed, the Large Hadron Collider (LHC), the new hadron circular accelerator, will boost two counter rotating beams of protons to an energy of 7 TeV. At the same time, four big experiments are being installed, in the LHC ring and are expected to exploit the LHC physics potential and provide further insight into our understanding of particles and fundamental interactions. These four experiments are two general purpose experiments ATLAS and CMS, an experiment for heavy ion studies, ALICE and an experiment dedicated to b-quark physics, LHCb. Apart from these four big experiments there are also two smaller ones; the TOTEM which is dedicated to elastic and diffractive cross-section measurements and LHCf which will study forward produced particles as a source to simulate cosmic rays in laboratory conditions.

The main reason why the LHC has been built lies in our current understanding of particle physics which is represented by the so-called Standard Model theoretical framework. The Standard Model (SM) is a quantum field theory which is being developed for almost 50 years and incorporates consistently both quantum mechanics and special relativity, and although it has been verified to a great extent, there are still open questions that have not been addressed experimentally. The mechanism via which all constituents of matter acquire mass, is predicted within the SM framework but requires the existence of the Higgs boson which has not been observed yet by any experiment. The high centre-of-mass energy available at the LHC will allow physicists to search for the Higgs boson in the region allowed by the SM ($\sim 1\ TeV$) and answer the question on its existence. Apart from the Higgs boson though, the LHC will provide the means for precision tests of the SM as well, like the measurement of various production cross-sections or the measurement of the W boson and t-quark mass.

The identification of many physical processes depends on the precise measurement of muons and their momenta. Because of their penetrating nature, muons do not stop in the electromagnetic or hadronic calorimeters of a typical colliding beam experiment, like the rest of the particles. Moreover, it is imperative to measure precisely muons with high transverse momentum which are produced at these very high beam energies. This can be achieved with a large Muon Detector immersed inside a strong magnetic field as the outermost part of the experiment, with trigger capabilities on interesting physics events with muons.

This thesis has taken up various important aspects of muon identification and reconstruction at the LHC and in particular with the ATLAS detector. In ATLAS, muon measurements are realized by a huge Muon Detector which is immersed inside a toroidal magnetic field and can achieve the designed momentum resolution which varies between $\sim 2\%$ at 100 GeV and 10% at 1 TeV muon. The main topics that this thesis focuses on, are outlined below.

- **Track reconstruction capabilities of the muon chambers under different irradiation conditions.**

  The main detecting element of the Muon Spectrometer is the muon tracking chamber composed of aluminium analogue drift tubes. For the above, the track reconstruction capability of a muon tracking chamber in the H8 testbeam at CERN is studied in order to understand the performance in different illuminating conditions and at different particle incident angles. The procedure followed and the results are presented in chapter 4.

- **Measurement of catastrophic muon energy loss using data from the H8 testbeam.**

  A basic requirement which should be taken into account in the muon track reconstruction phase, is the correction for the energy loss in the calorimeters. The correction is usually dealt with analytical methods that account for the physical processes which take place when a muon traverses the material of the calorimeters. For high-p_T muons though, this approach is not always sufficient but has to be complemented by direct measurement of the energy deposited in the calorimeters. Such a case is when a muon deposits a large fraction of its energy in the calorimetric material, also known as catastrophic energy loss. In the context of this thesis, muons with catastrophic energy loss were identified in the H8 combined testbeam data and the probability for such large energy losses was computed for 350 GeV muons and compared to Monte Carlo simulation expectations. This analysis is presented in chapter 5.

- **Energy deposition measurement in the ATLAS calorimeters.**
  The above point implies that combining the information from the Muon Spectrometer and the calorimeter systems is very important during reconstruction and physics analysis. Not only can a measurement in the calorimeters provide the energy loss of the muon itself but it can also provide valuable information on their isolation. Isolation criteria are used online to trigger on interesting physics events but they are also used offline, where variables of the transverse energy deposited around the muon track, accompanies the high level analysis muon objects. Based on these considerations, a precise energy deposition measurement method in the calorimeters around muon tracks, has been developed and is described in detail in chapter 6. An alternative isolation variable is proposed based on Monte Carlo simulation studies of $t\bar{t}$ events. This method is integrated in the official ATLAS software reconstruction chain and provides the measured transverse energy for the isolation related variables in the final analysis muon object.

- **Z boson pair production studies with the ATLAS detector.**
  The production of Z boson pairs in proton-proton collisions is predicted by the electroweak sector of the SM. At the LHC energies, the cross-section measurement of this process is an excellent test of the SM in the high energy regime but at the same time, it is of great interest because it constitutes the irre-

ducible background to the observation of the Higgs boson production through its decay to four leptons. The observation expectations with the ATLAS detector, of Z boson pair production, through the process $pp \rightarrow ZZ^{(*)} \rightarrow \ell\ell\ell\ell$ (where $\ell = e$, μ) is investigated in chapter 7.

Summarizing, this thesis is organised as follows. In chapter 2 the LHC accelerator is described and the main physics research topics are outlined. Chapter 3 focuses on the ATLAS detector where the various sub-detector technologies and the magnet and trigger systems are described, with emphasis on the Muon Spectrometer. In the last sections of this chapter the software framework of the ATLAS experiment which is also used in the current thesis, is also presented. The study on the performance of the muon tracking chamber and in particular of a BIS type chamber follows in chapter 4. Chapter 5 consists of a brief theoretical introduction to the energy loss mechanisms of muons in matter and the investigation on the catastrophic muon energy loss in testbeam data. The ATLAS software tool that has been developed in order to measure the energy deposited in the ATLAS calorimeters around a track, is described in detail in chapter 6 and application on isolated and non isolated muons from Monte Carlo simulated data is presented. In chapter 7 a complete analysis on the diboson production through the decay $ZZ^{(*)} \rightarrow 4\ell$ and its prospects to be measured with 1 fb^{-1} is presented. Finally, in the last chapter 8, the highlights of the work presented in all previous chapters, are summarized.

2

The Large Hadron Collider

2.1 Basic design parameters

The Large Hadron Collider [1] is the next generation circular particle accelerator built in the same underground tunnel that LEP, its predecessor, was built and operated during the period 1989 - 2000. LEP collided electron and positron beams at a centre-of-mass energy of $\sim 90\ GeV$ in the initial phase and 209 GeV in the last data taking period, providing the means for corner stone discoveries in particle physics like the determination of the number neutrino families by the precise measurement of the Z boson width. Nowadays, the LHC ring, which has a total circumference of 26.7 km, will be capable of delivering two counter rotating proton beams at the unprecedented energy of 7 TeV each, hence offering collisions at a center-of-mass energy of 14 TeV. This is by far the highest achievable center-of-mass energy ever, since it is seven times the energy at Tevatron, which is the most powerful accelerator currently operational.

The LHC will actually shoulder the responsibility of increasing the proton beam energy from 450 GeV to the designed 7 TeV. Up to 450 GeV, protons will pass through several accelerating phases in CERN's accelerator complex, a schematic layout of which is illustrated in Fig.2.1. After protons will be extracted from a bottle of hydrogen gas, they will be boosted to 50 MeV by a linear accelerator succeeded by a small circular accelerator (PSB) that will further increase their energy to 1.4 GeV before they are injected into the Proton Synchrotron (PS). In the PS the beam energy will reach 26 GeV and will be passed to the Super Proton Synchrotron (SPS) for the next acceleration phase that will take them up to 450 GeV, the starting point of the LHC. Protons will be accelerated in bunches and the storage ring will contain 2808 bunches with 1.15×10^{11} protons each, in both directions, colliding every 24.95 ns. It is also planned that the LHC will collide beams of heavy ions (lead ions) at a center-of-mass energy of approximately 6 TeV per nucleon.

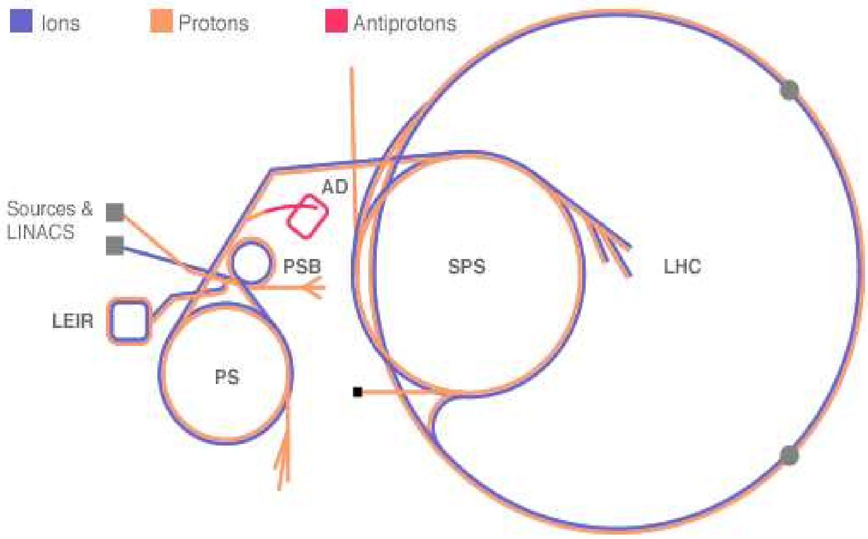

Figure 2.1: **The LHC injection complex** - The linacs, PSB, PS and SPS machines are used as pre-accelerating phases of the two counter rotating proton beams that are finally inserted into the LHC ring.

Preserving the trajectory of such energetic particle beams into circular orbit is very challenging for the magnet system that has to be deployed. The LHC is equipped with 1232 superconducting dipole magnets, 14.3 m long each, placed around the ring, forming a magnetic field of 8.33 $Tesla$. Because there are two separate beam lines of protons moving in opposite directions, each magnet consists of two sets of coils producing opposing fields. Liquid helium is used for cooling of the magnets down to approximately 2 K. A schematic rep-

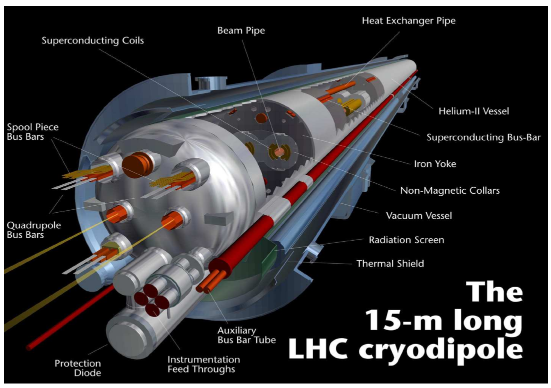

Figure 2.2: **A cryodipole magnet of the LHC**.

Parameter	Value
Proton beam energy	$7\ TeV$
Number of bunches per beam	2808
Number of particles per bunch	1.15×10^{11}
Circulating beam current	$0.584\ A$
RMS of bunch length	$7.55\ cm$
Peak luminosity	$1.0 \times 10^{34}\ cm^{-2}\ s^{-1}$
Collision time interval	$24.95\ ns$
Number of main bends	1232
Field of main bends	$8.33\ T$

Table 2.1: **Basic design parameter values of the LHC machine.**

resentation of an LHC dipole magnet is shown in Fig.2.2. There are also 392 quadrupole magnets which provide the necessary focusing of the beams.

The above and other basic design parameters of the LHC machine are summarized in table 2.1.

2.2 Luminosity

In a colliding beam experiment, apart from the centre-of-mass energy, one of the most important parameters is luminosity. Luminosity is indicative of the particle accelerator's performance because as it can be seen in the following equation 2.1, depends by definition only on machine related parameters:

$$L = \frac{N_1 N_2 f_{col}}{4\pi\sigma_x\sigma_y} \left[\frac{1}{cm^2 s}\right] \tag{2.1}$$

The previous formula shows that L is proportional to the number of particles in each bunch of the two beams N_1 and N_2 and at the same time is proportional to the rate of collisions f_{col}. The geometrical parameters σ_x and σ_y represent the horizontal and vertical size of the bunch in the transverse plane.

What makes luminosity important in particle accelerator experiments is relation 2.2 which connects the number of events per second created in such an experiment with luminosity and the cross-section σ of the particle reaction under study.

$$R = \sigma L \tag{2.2}$$

Many physics processes are very rare, with cross-sections of a few fb, therefore according to equation 2.2, one has to increase the luminosity as high as possible to study such processes with sufficient statistics and within a reasonable time. The amount of data collected within a particular time period is often expressed in units of inverse barns ($1\ barn \equiv 10^{-28}\ m^2$).

At the LHC, where $f_{col} = 1/24.95 = 40.08\ MHz$, $N_1 = N_2 = 1.15 \times 10^{11}$ protons and a typical value of bunch size of a few μm, the luminosity is $10^{34}\ cm^{-2}\ s^{-1}$. This is the design value of the LHC run period which is called 'high luminosity'. However, during the first years of operation luminosity is going to be one order of magnitude lower at $L = 10^{33}\ cm^{-2}\ s^{-1}$ and this is called 'low luminosity' period.

Equation 2.2 also says that high luminosity provides very high interaction rates. Considering a proton-proton interaction cross-section of approximately 100 mb yields 10^9 particle interactions per second. It is expected that in each bunch crossing one interesting physics event will emerge out of 23 other inelastic events on average and the total number of particles will be roughly 1000. This means that particle detectors will be subject to large radiation fluences, therefore radiation tolerance is a basic priority of the construction design concept.

A nice picture of how the cross-section of the different physics processes scales with the centre-of-mass energy, is shown in Fig.2.3. The vertical bands correspond to the centre-of-mass at the LHC and the Tevatron. What is interesting to mention here is the fact that pure QCD processes have many orders of magnitude bigger cross-sections than the processes of high interest like the Higgs production or the production of W and Z bosons.

2.3 The LHC experiments

Four experiments are now under construction around the LHC ring scheduled to switch on in 2008:

ATLAS (**A** **T**oroidal **L**HC **A**pparatu**S**)

A general purpose detector with a broad physics searches program. However

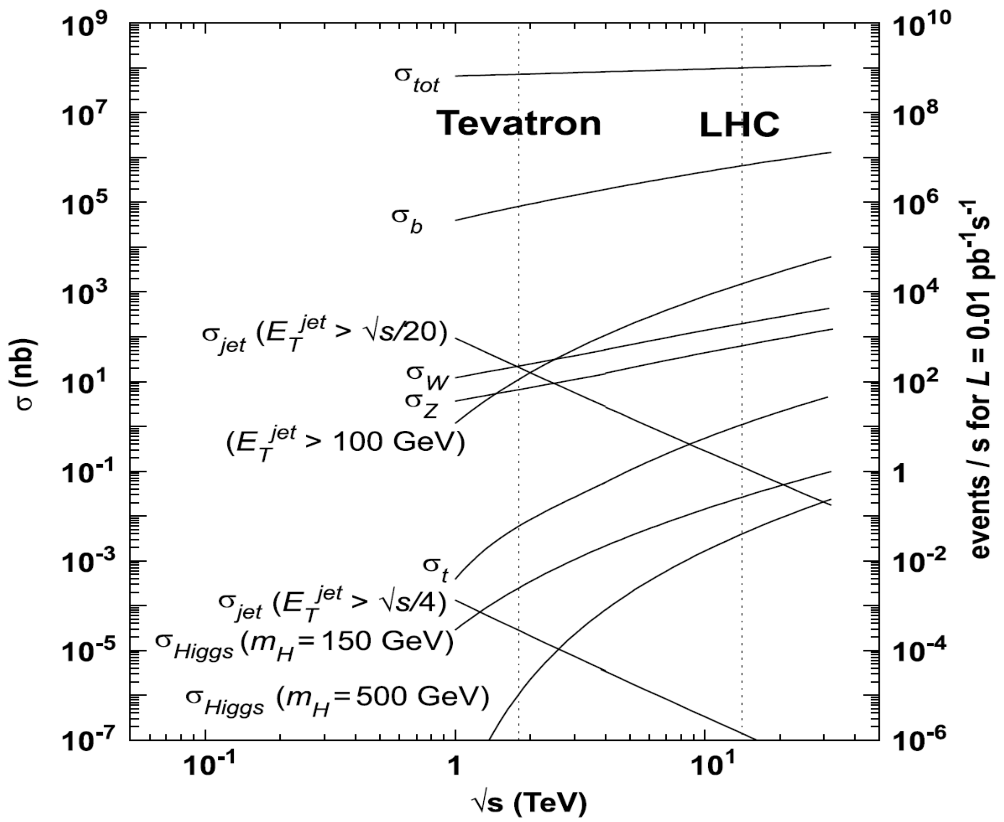

Figure 2.3: **Cross-section of various physics processes in proton-proton collisions as a function of the centre-of-mass energy.**

it will be mainly occupied with the search for the Higgs boson, SUSY particles and CP violation measurements. More detailed description of ATLAS is given in the next chapter.

CMS (**C**ompact **M**uon **S**olenoid)

CMS is the second large experiment constructed at the LHC. It is also a general purpose detector 21 m long and 16 m in diameter and weighs approximately 12500 tonnes. Its physics research area is similar to ATLAS but differs completely from the latter in the design principle. It is also worth mentioning that the biggest part of the construction phase was completed on the surface and then the detector was lowered to its final installation point.

ALICE (**A** **L**arge **I**on **C**ollider **E**xperiment)

ALICE is a detector specialized in heavy-ion physics and is devoted to the search for quark-gluon plasma. The latter is a state of matter where both quarks and gluons are considered as free particles and is expected to be created in heavy-ion collisions.

LHCb

LHCb is a detector that will focus on *b*-quark physics and precise CP violation measurements studies. It is designed to operate at almost two orders of magnitude lower than the nominal luminosity, therefore it is expected to exploit the LHC potential for physics studies already in the first years of operation.

2.4 Physics program

The LHC and the experiments built around its ring are expected to provide further insight into the physics of fundamental particle interactions and the SM. For this reason, an extensive physics program has been compiled by the collaborations of the experiments [2, 3, 4, 5]. Some highlights of the searches planned to be performed at the LHC are described in the sections that follow.

2.4.1 The Higgs boson

In the SM, the Higgs mechanism provides a way to give mass to particles by interacting with a field called the "Higgs-field" which is present everywhere in space. This mechanism requires though the existence of a mediator boson, the so-called Higgs boson, which up to now has not been observed by any experiment. Although within the theoretical context of the SM the Higgs mass is a free parameter, thus it cannot be predicted, a theoretical upper limit can be still set indirectly at 260 GeV if precision measurements of electroweak parameters are taken into account [6]. At the LHC, however, searches for the Higgs will not be confined to this limit but are going to extend up to the TeV scale. At the same time, experimentally the non-observation of the Higgs boson in searches performed at LEP has set a low limit to the Higgs mass at 114.4 GeV [7].

The production mechanisms of Higgs, shown in the Feynman diagrams of Fig.2.4, illustrate the fact that the Higgs boson prefers to couple to the heavy particles like the W and Z vector bosons or to the top quark. These mechanisms are the associated production with W/Z bosons (Higgs-Strahlung), the vector boson fusion mechanism, the gluon-gluon fusion and the associated Higgs production with t-quark. The dominant mechanism of the Higgs boson production is the gluon-gluon fusion process. This is also seen in Fig.2.5 where the cross-sections of the possible production modes of the Higgs boson at the LHC is given as a function of the mass of the Higgs.

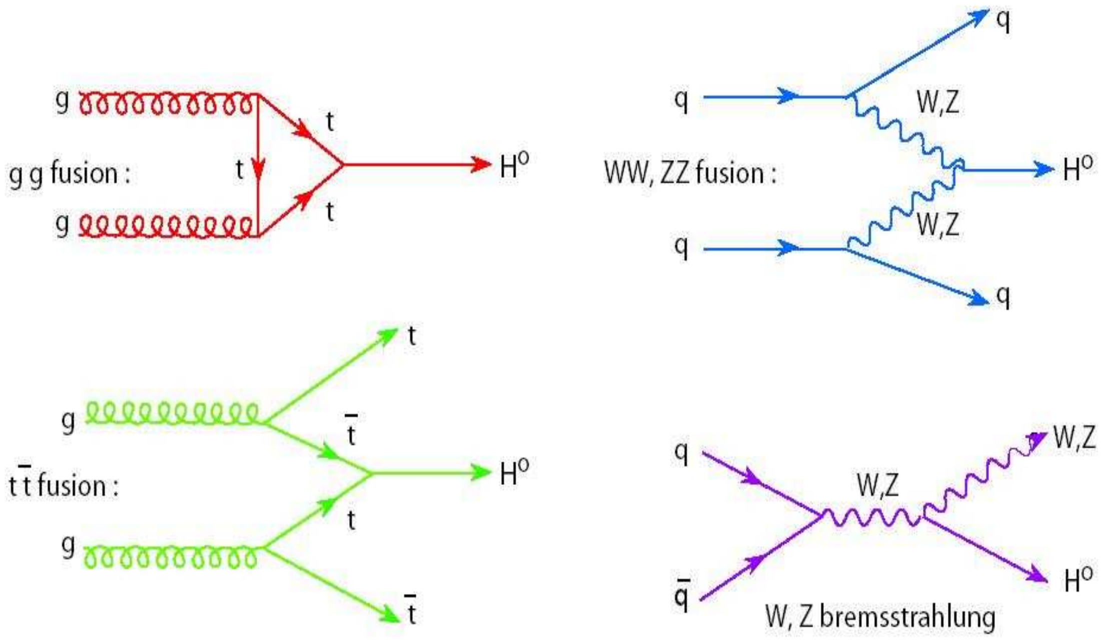

Figure 2.4: **Feynman diagrams of main Higgs production mechanisms** - Four main mechanisms are predicted within the Standard Model. Gluon-gluon fusion, WW/ZZ fusion, associated $t\bar{t}H$ and associated WH/ZH(Higgs-Strahlung).

The observation of the Higgs boson relies on the experimental signature of one of its possible decay modes. The latter depend on the mass of the Higgs, therefore different decay channels are anticipated at different Higgs mass ranges. The branching ratio as a function of the mass of the Higgs is shown in Fig.2.6. Main decay channels are:

- Low mass region, $m_H < 120\ GeV$
  $H \to b\bar{b}$

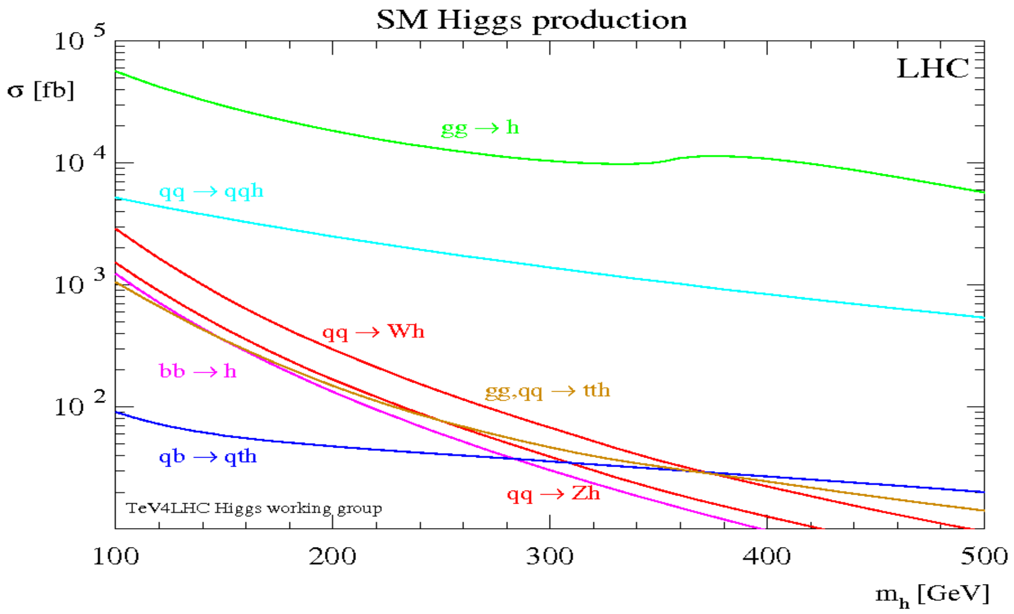

Figure 2.5: **LHC cross-sections of the Higgs boson production mechanisms as a function of its mass.**

$H \to \gamma\gamma$

- Intermediate mass region, $120 < m_H < 600\ GeV$

  $H \to ZZ^{(*)} \to 4\ell$

  $H \to WW^{(*)} \to \ell\nu\ell\nu$

- High mass region, $m_H > 600\ GeV$

  $H \to ZZ \to \ell\ell jj$

  $H \to WW \to \ell\nu jj$

2.4.2 SuperSymmetry

According to SuperSymmetry (SUSY), each elementary particle has a super-partner. The quantum numbers between two super-partners are identical except for the spin. For example, the super-partners of fermions which are spin-$\frac{1}{2}$ particles are particles with spin-0 (s-fermion) and spin-1 bosons have spin-$\frac{1}{2}$ partners (boson-ino).

If SUSY exists, observation or related physics channels is expected already in the first year of running at low luminosity because the cross-sections of such processes are

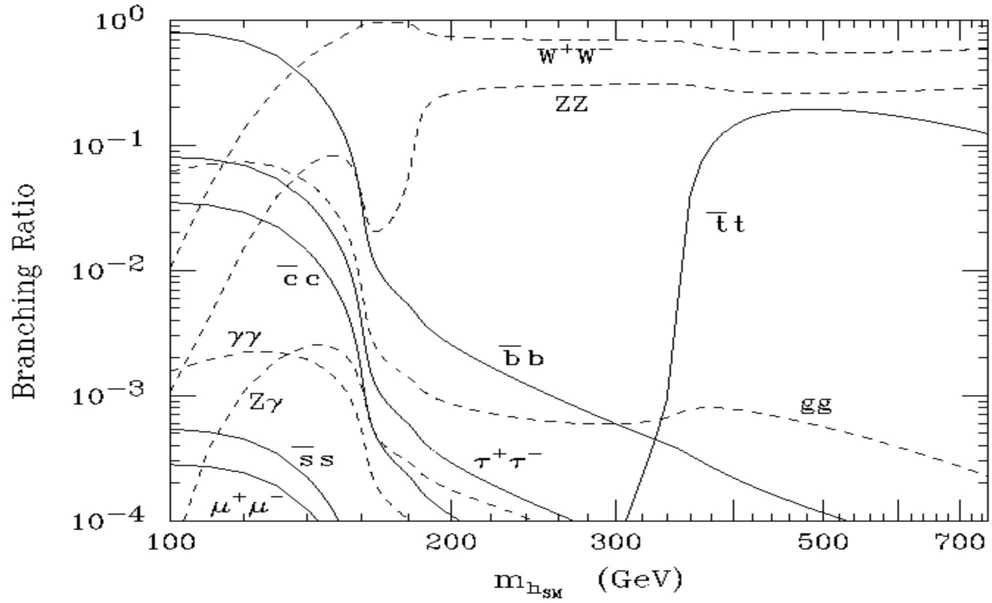

Figure 2.6: **Branching ratio of the Higgs boson as a function of its mass** - The prominent decay modes differ in each mass range which is usually characterized as low, intermediate and high mass range (see text).

big enough to produce sufficient statistics. The striking feature of supersymmetric decays is the large missing transverse energy due to the presence of the lightest supersymmetric particle, neutralino. Neutralino is assumed to be stable and weakly interacting and its existence can be confirmed only indirectly since it escapes the detector.

2.4.3 Top quark physics

From all the quark families the mass of the top quark distinguishes it from the rest because it is almost 35 times heavier than the second heavier, the b-quark. This striking feature raises many questions about its precise role within the SM. Studies at the LHC experiments will focus on the role of the t-quark in the electroweak symmetry breaking mechanism. The t-quark decays almost exclusively through the channel $t \rightarrow Wb$. At the LHC, measurements of the mass of the top and the production cross-section of $t\bar{t}$ pairs and also single top events, have been planned.

The LHC will be a t-quark factory. During the first year of LHC operation and with 10 fb^{-1} of data, millions of $t\bar{t}$ events are expected to be produced. This will provide to studies in this field sufficient statistics for analysis soon after the LHC commences.

2.4.4 B physics

An extensive B-physics program will take place at the LHC. ATLAS and CMS, although not designed as detectors specialized in b-physics, have also scheduled a study program, especially during the first years of operation at low luminosity, which includes CP violation searches through channels like $B_d^0 \to J/\psi K_S^0$, the experimentally harder $B_d^0 \to \pi^+\pi^-$ and the decay $B_d^0 \to J/\psi\phi$. In addition, studies of B_s^0 oscillations and searches for rare decays such as $B_d^0 \to \mu^+\mu^-$ and $B_s^0 \to \mu^+\mu^-$ will be performed.

Definitely, leading role in the exploration of the B-physics sector at the LHC will be played by LHCb, which is completely devoted to these kind of studies and results are expected soon after LHC switches on, since, as it has been mentioned before, this detector is designed to operate at low luminosity.

2.4.5 Physics beyond the Standard Model

The range of physics studies at the LHC will not be exhausted only by SM topics. Several theories of physics beyond the SM will be tested at the experiments.

New heavy gauge bosons W' and Z' could exist with masses up to $\sim 6\ TeV$ therefore they will be accessible at the LHC.

Leptoquarks, as they are called, is another interesting theory beyond the scope of the SM, suggesting that particles which carry both baryon and lepton numbers should exist. They couple to both leptons and quarks and so far searches have been unsuccessful at HERA and Tevatron up to masses of $\sim 170\ GeV$. In the LHC environment however it will be possible to enlarge the mass window up to 3 TeV. Usual decay modes of leptoquarks are the ones with a charged lepton or neutrino accompanied by a quark jet.

New physics searches also include compositeness models suggesting that particles like electrons and quarks are not elementary but enclose some structure at the compositeness scale Λ, which of the order of 1 TeV.

The list of searches for new physics is also enriched with topics like, technicolor resonances, extra dimensions models, excited quark states up to the mass range of 6 GeV and new particles required in Higgs related scenarios. It remains to nature itself and the experimental and theoretical physicists to address these questions when the LHC starts in 2008. To this end, the ATLAS detector will provide the means to perform all these interesting studies. In the next chapter, the ATLAS experiment is described in more detail.

3

The ATLAS Detector

3.1 General design considerations

3.1.1 Basic design properties and requirements

ATLAS [8, 9] is one of the four big experiments of LHC, currently under its commissioning phase at Point-1 experimental area at CERN. Geometrically, ATLAS (Fig.3.1) has cylindrical shape, 4π coverage and dimensions of 25 m height and 44 m length while it weights not less than 7000 tonnes. ATLAS is a multi-purpose detector and as such it is designed to take full advantage of LHC's potential and its compiled physics program covers wide range of physics processes.

The variety of physics research studies and LHC's intrinsic experimental environment, impose some basic design and performance requirements for the ATLAS detector:

- All detecting elements, such as gaseous and solid state detectors, electronics and sensors are required to be radiation-hard in order to tolerate the high particle fluxes expected at the LHC

- Large η and full ϕ coverage

- Excellent calorimetry for both electrons and photons in addition with precise missing transverse energy (E_T^{miss}) and jet energy measurements, which also implies very good detector hermeticity

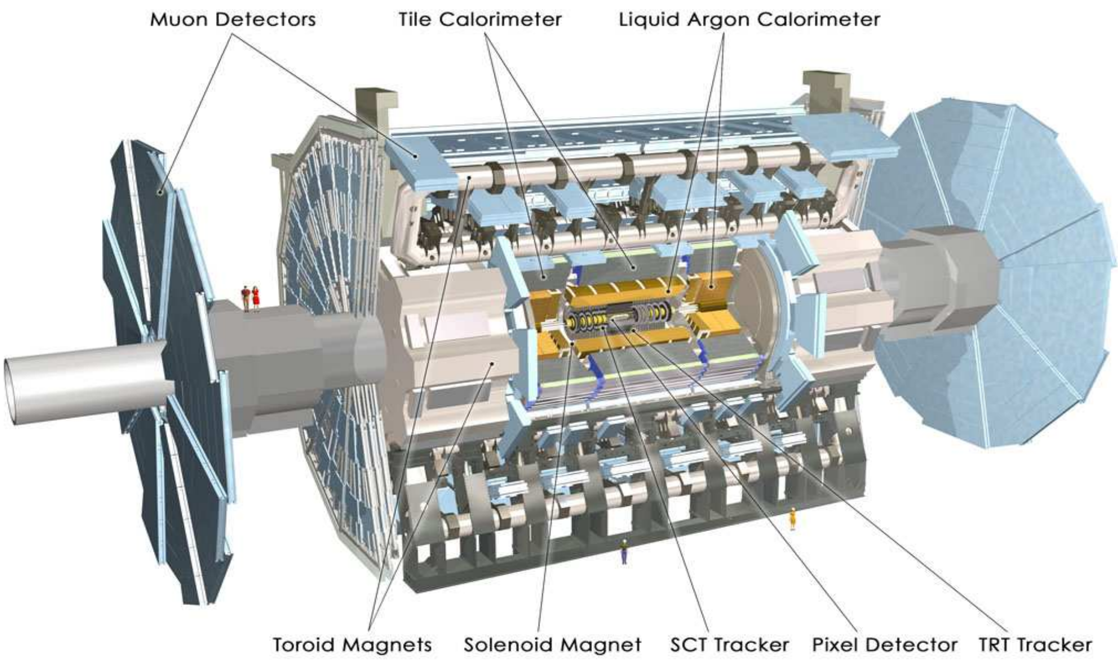

Figure 3.1: **Cut-away view of the ATLAS detector** - Also illustrated are the different detector sub-systems.

- High accuracy in muon momentum measurements over a wide range of momenta
- For offline tagging of τ-leptons and b-jets, vertex detectors close to the interaction region are required to observe secondary vertices
- Highly efficient triggering on low-p_T particles with sufficient background rejection

ATLAS consists of four main sub-systems for which a more detailed description is given in the following sections. In brief these sub-systems are:

- Inner Detector (ID) for tracking, momentum measurements of particles and vertex reconstruction
- Calorimetric System (CS) for energy measurements of both leptons and hadrons
- Muon Spectrometer (MS) for muon momentum measurements
- Magnet System (MagS) for bending of charged particle's trajectory.

3.1.2 The coordinate system

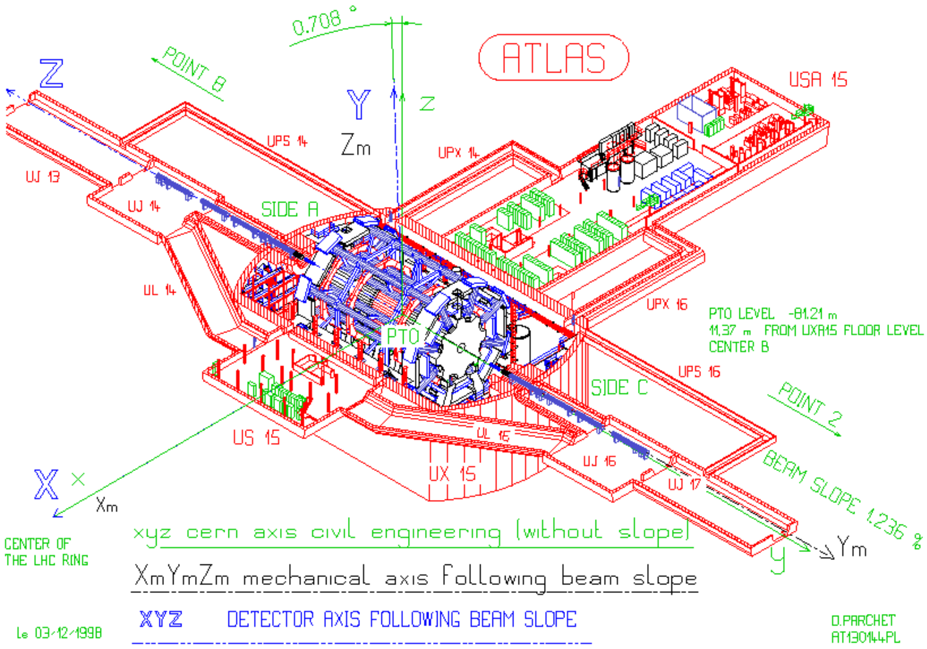

Figure 3.2: **The ATLAS coordinate system** - The transverse to the beam axis plane is defined by the x and y axes.

The coordinate system used in ATLAS is illustrated in Fig.3.2. It is a right handed coordinate system with origin in the very middle of the detector at the interaction point. The z-axis is defined by the beam direction, the positive x-axis points from the origin to the centre of the LHC ring and the y-axis points upwards, hence the xy plane is perpendicular to the beam axis. Using polar coordinates, R is the distance from the origin, $\theta\,[0,\pi)$ is the polar angle from the z-axis and $\phi\,[-\pi,\pi]$ the azimuthal angle which runs around z-axis. Important quantities like momentum and energy are usually given in the transverse plane xy. In this case the transverse component of these two quantities is defined as:

$$p_T = Psin\theta,\; E_T = Esin\theta \tag{3.1}$$

Another important quantity that is widely used in particle physics experiments is the rapidity which is defined by:

$$Y = \frac{1}{2}log\frac{E+p_z}{E-p_z} \tag{3.2}$$

where E is the energy of the particle and p_z is its momentum component in the z-direction. The rapidity Y is a Lorentz-invariant quantity and considering vanishing masses it can be approximated by:

$$\eta \equiv -ln(tan(\theta/2)) \quad (3.3)$$

which is the quantity called pseudo-rapidity and is most commonly used in the experiments when the exact mass and momentum of the particle is not known [10]. The coordinates η and ϕ form a plane where distances are measured by:

$$\Delta R = \sqrt{\Delta\eta^2 + \Delta\phi^2} \quad (3.4)$$

3.2 ATLAS sub-detectors, magnet and trigger systems

3.2.1 The Magnet System

Figure 3.3: **The central solenoid magnet** - The solenoid is 5.8 m long and produces a magnetic field of 2 T at the middle.

ATLAS uses an impressive magnet system [9, 11] in terms of both size and performance, in order to bend the trajectories of charged particles and therefore provide momentum measurements in the ID and the MS sub-detectors. It consists of one superconducting central solenoid placed around the ID cavity and three superconducting toroids, one in the barrel and two in the end-cap regions. The overall diameter of the magnet system is 22 m and extents axially to 26 m while the energy stored is 1.6 GJ.

Central solenoid

The 5.8 m long central solenoid is a single layer coil wounded on the inside of a 12 mm thick support cylinder (Fig.3.3). The solenoid surrounds the ID and forms in its vicinity an axial magnetic field of 2 T, at the centre, and 0.5 T at the edges, while the operation temperature is 4.5 K. It is crucial that the energy loss of all particles traversing the material before the CS is kept minimum, therefore it is chosen to include the solenoid inside the same cryostat that houses the liquid argon electromagnetic calorimeter so that it adds only $\sim 0.66X_0$ of material before the CS.

Air-core toroid

The barrel part of the air-core toroid magnet system is situated around the calorimeters at an inner radial distance from the interaction point of 9.4 m and extends to 20.1 m, while its length is 25.3 m. It consists of 8 coils circularly surrounding the beam axis, which are sitting inside stainless-steel vacuum vessels.

The end-cap toroids are inserted in the barrel at each end of the central solenoid but they are rotated with respect to the barrel in order for the coils to interleave and maximize the bending performance at the transition region between barrel and end-cap.

The toroids are cooled down to 4.5 K by a liquid helium cooling system. The strength of the produced magnetic field in the barrel varies with η and has a peak value of 3.9 T while in the end-caps the peak value is slightly bigger at 4.1 T. A sketch of one of the end-cap toroids is shown in Fig.3.4 whereas an impressive photograph of the barrel toroid system taken during the installation phase of ATLAS, is shown in Fig.3.5.

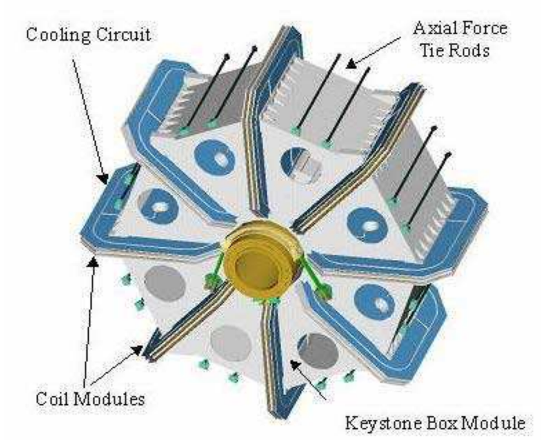

Figure 3.4: **Sketch of an end-cap toroid magnet**

In 2006 a full test of the ATLAS barrel toroid system was performed [12, 13]. During the test, the current of the magnets was raised gradually until the nominal operation value of 20.5 kA. At that point, another 500 kA was added on top of the nominal operation current without any problems, proving that the MagS of ATLAS is capable of taking extra current loads with safety. The second interesting part of the test was a deliberately caused quench in order to check the quench heating system which forces the entire magnet into the normal conducting state within less than two seconds, leading to a very safe global cold mass temperature of about 58 K and a hot-spot temperature in the windings of about 85 K maximum. The success of the test was the summit of a more than 15 year effort which included design, construction, testing and installation.

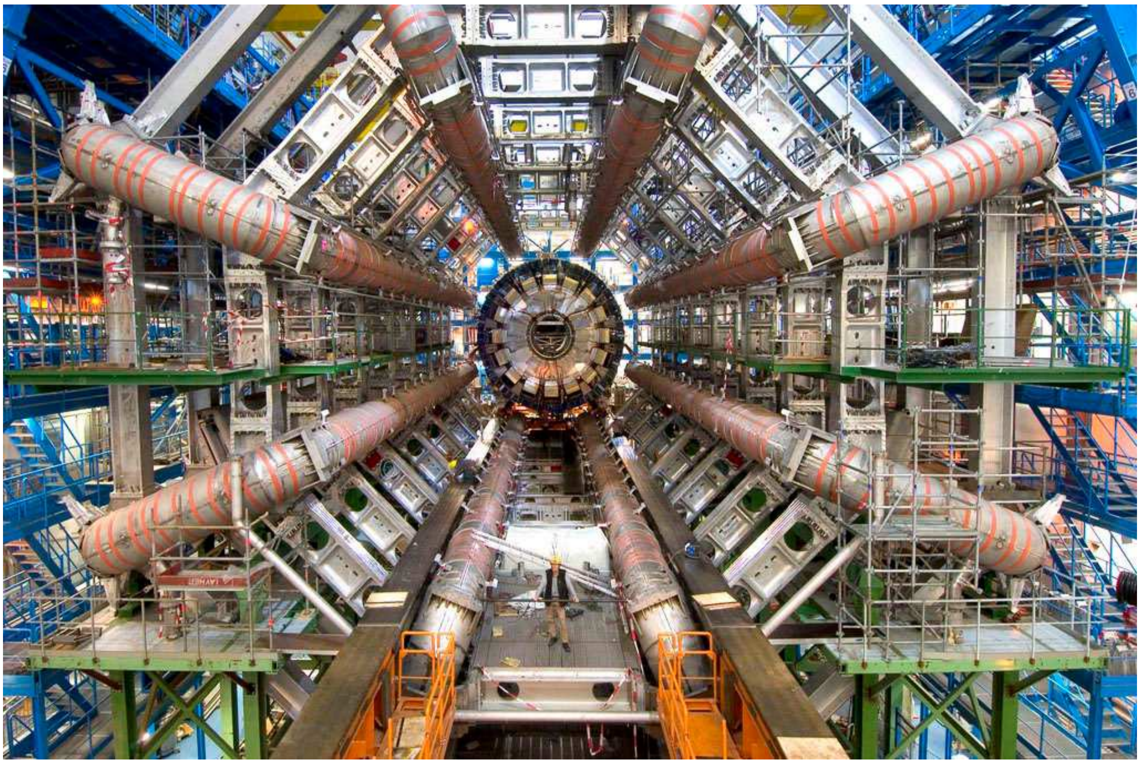

Figure 3.5: **Barrel toroid magnet system** - Photograph of the 8 coils comprising the barrel toroid system as installed in the ATLAS cavern.

3.2.2 Inner Detector

The Inner Detector [9, 14] is the innermost part of the ATLAS detector. It is contained inside a 7 m long envelope with radius of 1.15 m and the whole system is immersed inside the 2 T magnetic field formed by the central solenoid, described in the previous section. It is divided in three systems which, in order of radial distance from the collision point, are: the Pixel Detector, the Semiconductor Tracker (SCT) and the Transition Radiation Tracker (TRT). These three, although technically independent, act complementary to fulfill the basic experimental duties carried out by the ID, which are track reconstruction and vertexing. A schematic representation of the ID and its three sub-systems is shown in Fig.3.6.

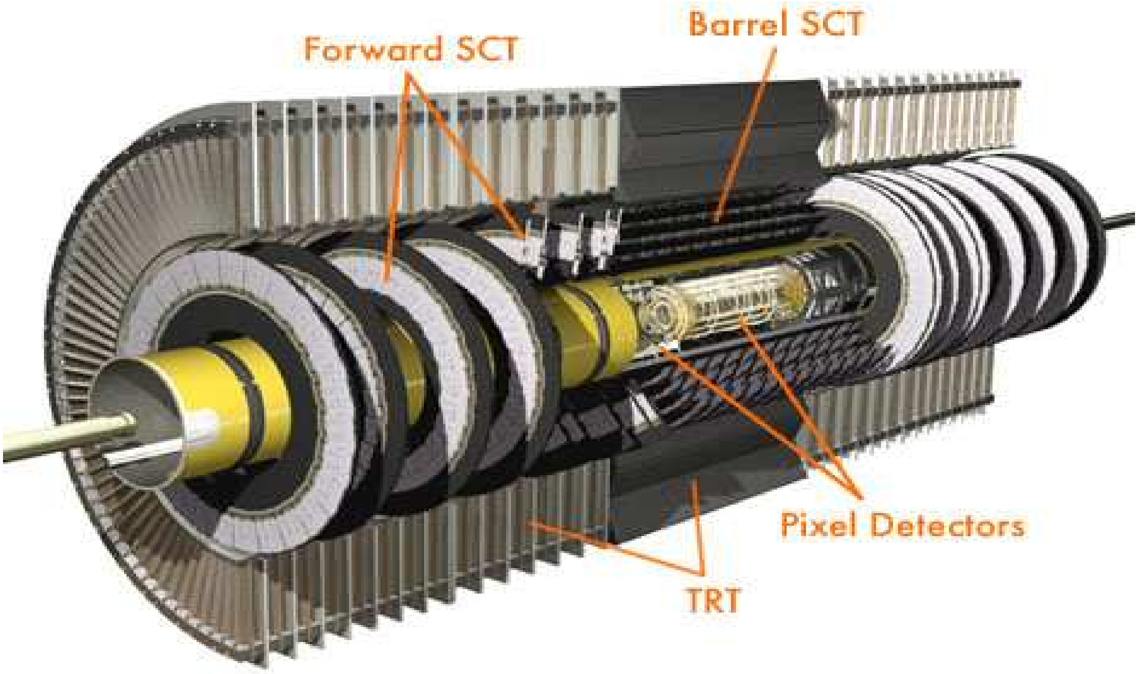

Figure 3.6: **Cut-away view of the ATLAS Inner Detector** - The innermost system is the Pixel Detector while the middle is the SemiConductor Tracker. Both these systems use silicon as the detecting technology. The outermost part is the Transition Radiation Tracker which uses the straw tube technology.

The fact that the ID is installed at the closest distance from the interaction point indicates that special design and performance considerations should be taken into account, because in an environment where about 1000 particles emerge every 25 ns one has to think about radiation tolerance of the detecting elements, efficient pattern recognition and high resolution of momentum and vertex measurements. It is planned that after about three years of operation the first layer of the Pixel Detector from the interaction point (B-layer) is going to be replaced because of radiation damage, whereas the other parts and the SCT and TRT are expected to withstand large particle fluences over ten years at nominal luminosity.

Regarding performance, the ID has very fine granularity to reduce occupancy levels and high efficiency in track reconstruction. Precision measurements are achieved by combination of the three systems in which the Pixel and the SCT provide few space point measurements but with high precision and at the same time TRT improves pattern recognition and momentum resolution by contributing 36 hits per track on average. In the following a more detailed description of the ID's systems is given.

Pixel Detector

The operation principle of the Pixel Detector is based on a modular unit of detector substrates and integrated read-out electronics. The active material is silicon arranged into rectangles (pixels) of size $50 \times 400\ \mu m^2$ and thickness $250\ \mu m$. There are three layers of such units in the barrel region at radial distances from the interaction point of 5.05 *cm*, 8.85 *cm* and 12.25 *cm* while in the end-caps the pixel units are arranged on three disks on each side at distances of 49.5 *cm*, 58.0 *cm* and 65.0 *cm*. The overall rapidity coverage of the pixel detector is $|\eta| < 2.5$.

The B-layer, located closer to the collision point than any other detector element, guarantees optimal impact parameter resolution and, accompanied with the other two layers of pixels, provide high precision space-point measurements of intrinsic accuracy $10\ \mu m$ in $R - \phi$ and $115\ \mu m$ in the z-direction and also the ability to reconstruct tracks of short lived particles and their corresponding vertex. The accuracy is similar in the end-cap region where the disks are present. In total, the Pixel Detector has 80.4 million read-out channels due to its fine segmentation.

Semiconductor tracker

The SCT is the intermediate sub-system of the ID and its basic building block is a module consisting of two layers of silicon micro-strip wafers glued back to back and a hybrid system containing the read-out electronics. In the barrel there are four layers of such modules giving four precise space-point measurements located at radii of 30, 37, 45 and 52 *cm*, while at the end-caps modules are arranged perpendicularly to the beam axis on 9 disks on each side, extending from 85.4 *cm* to 272.0 *cm* in z and with an outer radius of 56 *cm*. In total there are 2112 modules in the barrel and 1976 modules in the end-caps.

Instead of pixels, the SCT uses silicon strip technology with a strip pitch of 80

μm and each layer consisting of 768 strips. The two layers of silicon wafers are rotated by 40 $mrad$ stereo angle with respect to each other to allow for second coordinate measurement. The resolution in the $R - \phi$ plane is 22 μm and in the z-coordinate is 580 μm.

The particle detection principle of both SCT and Pixel is based on the ionization caused by charged particles when they traverse the silicon bulk. Ionisation produces electrons and holes which drift in opposite directions under the influence of an electric field created by a potential difference applied to the sides of silicon wafer. Charges are collected at each end of the detector and after the signal is amplified, is read-out through the electronics. In order to reduce noise from leakage currents emerging in silicon's bulk because of thermal excitation and radiation damage of the detector, the SCT will operate at a temperature of $-7\ ^oC$.

Transition Radiation Tracker

TRT is the sub-detector system of the ID which is further away from the interaction point and uses different technology than the other two systems. It extends radially from 56 cm to 107 cm and is capable of providing on average 36 measurements per track with intrinsic accuracy of 130 μm. It uses straws of only 4 mm in diameter and 144 cm length that are filled with a gas mixture of 70% Xe, 20% CO_2 and 10% CF_4 and have a sense wire in the centre of 30 μm diameter.

The principle of operation of the TRT is based on transition radiation which is the radiation emitted by charged particles in the X-ray range when they traverse the boundary between two substances with different dielectric properties. The intensity of this radiation depends on the particle's energy $E = \gamma mc^2$. When a charged particle traverses the straws ionizes the gas and produces electrons that are collected at the wire. The drift time of electrons to the wire provides discrimination between tracking hits and hits from transition radiation. This enhances the identification of electrons and the discrimination between electrons and pions.

3.2.3 Calorimeters

The ATLAS Calorimetric System [9] is located between the ID and the MS and is divided into electromagnetic, hadronic and forward calorimeter parts. The electromagnetic covers the range $|\eta| \leq 3.2$ and the hadronic, including the forward calorimeter, extends up to $|\eta| \leq 4.9$. The different parts and technologies of the CS are described in more detail in the following sections and a schematic view is given in Fig.3.7.

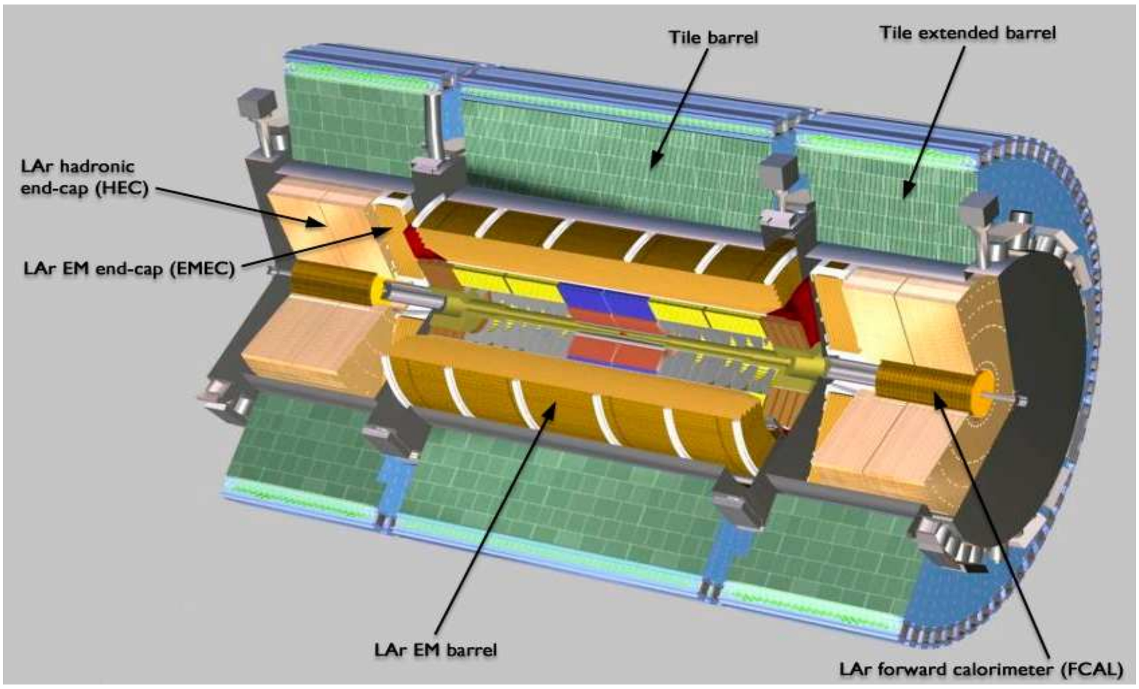

Figure 3.7: **Cut-away view of the ATLAS calorimeter system** - Also visible are the different types of calorimeters in the barrel and end-cap regions.

The objective of the ATLAS CS is to measure as precise as possible the energy of electrons, photons and jets and to provide information on the missing transverse energy (E_T^{miss}), which apart from the necessity of excellent energy measurement resolution, requires very good hermeticity. The latter is realized in the ATLAS CS with a pseudo-rapidity coverage of $|\eta| \leq 4.9$. In addition, the CS can enhance particle identification by providing parameters for the shower shape of particles and the energy longitudinal leakage.

Moreover, calorimetry has fundamental contribution to physics searches and data analysis because it provides particle isolation information. Isolation is an extremely valuable quantity because there are innumerable signatures of physics processes that require isolated leptons in the final state, therefore it can be used for signal selection and background suppression. For example, the "gold-plated" channel for discovering the Higgs is the decay process $H \rightarrow ZZ \rightarrow \ell\ell\ell\ell$, where the four leptons in the final state are required to be isolated.

Calorimetry is also important for muons because although they are measured in the Muon Spectrometer after penetrating through the CS, the precision of the measurement is limited since muons as well lose energy in the calorimeters.

Electromagnetic Calorimeter

The ATLAS Electromagnetic Calorimeter (LArEM) [9, 15] uses liquid argon as active material and steel coated lead (Pb) as absorber. For read-out, Kapton electrodes are utilized with the so-called accordion shape which provides symmetric coverage and lack of cracks in the ϕ coordinate. The choice of liquid argon emerges from its very good intrinsic radiation tolerance and linearity whereas the choice of lead is due to its high atomic number which ensures that the shower development of electrons and photons is sufficient for signal formation.

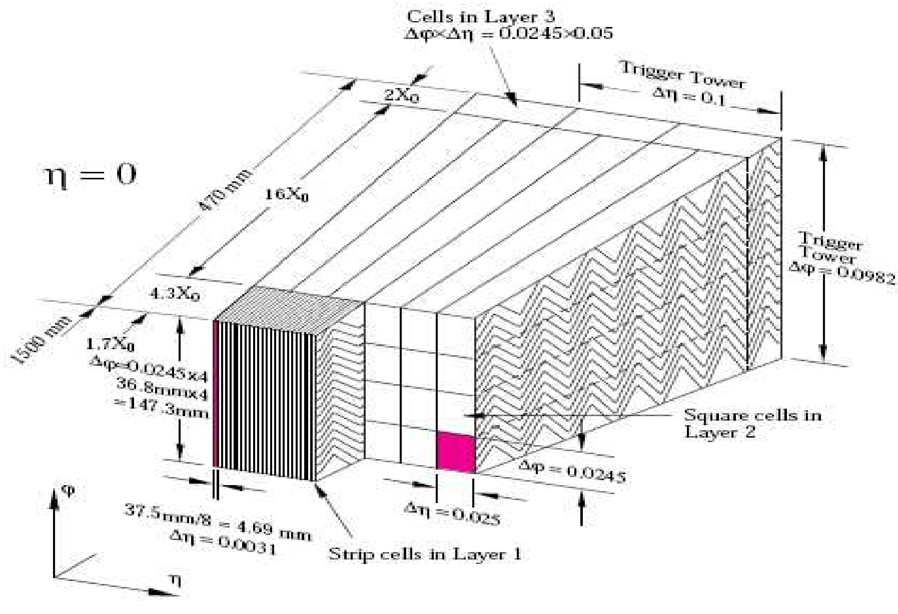

Figure 3.8: **Drawing of a Liquid Argon electromagnetic calorimeter module** - The drawing shows the three samplings comprising the LArEM and their corresponding granularities. The contribution of each section to the total material in units of radiation lengths is also shown.

The LArEM is divided in one barrel part which covers the range of $|\eta| < 1.4575$ and in two end-cap parts extending in the range $1.375 < |\eta| < 3.2$. The barrel shares the same cryostat with the ID minimizing thus the amount of material used, while the end-caps are housed in their own cryostats. The barrel is also divided in two identical parts placed on either side of a 4 mm gap at $z = 0$ which is used by services and cables of the ID. The LArEM, as well as the whole calorimeter, is segmented in square towers or cells of different sizes depending of position and calorimeter type.

In Fig.3.8 a sketch of a LArEM module is shown. In the pseudo-rapidity range -2.5 to 2.5 and longitudinally from the interaction point out, LArEM is segmented in three compartments called front, middle and back. The front sampling consists of narrow strips of 4 mm pitch and cell granularity in the barrel ($|\eta| < 1.4575$) is $\Delta\eta \times \Delta\phi = 0.003 \times 0.1$ while in the end-cap the granularity varies with η. This fine granularity allows precision position measurements along the η coordinate. The thickness of the front sampling in units of radiation lengths X_0 is 6 and is constant with η. The middle sampling has a cell size of $\Delta\eta \times \Delta\phi = 0.025 \times 0.0245$ and is the thickest of the three compartments. Including the material of the ID, cables, cryostat wall and solenoid coil the total contribution of material in X_0 before the CS is roughly 2.3 X_0 and up to the end of the middle compartment is > 24 in the barrel and > 26 X_0 in the end-caps. The third sampling has a granularity of $\Delta\eta \times \Delta\phi = 0.05 \times 0.025$ and the thickness varies between 2 X_0 and 12 X_0 depending on η.

In the region $|\eta| > 2.5$ the calorimeter is divided in two longitudinal samplings and the granularity is coarser serving the objective of jet reconstruction and good measurement of E_T^{miss}.

The material before the CS introduces an uncertainty in the measurement of the energy of the incident particles simply because energy is also lost in the material before the calorimeter. A correction for this energy loss is achieved using of a thin (11 mm in the barrel and 5 mm in the end-caps) active layer of liquid argon just before the front sampling, the presampler. Table 3.1 summarizes the coverage in η of the different compartments of the LArEM and their corresponding cell granularity.

The energy measurement resolution that is expected to be achieved with the

LArEM	Barrel		End-cap	
	$\Delta\eta \times \Delta\phi$	Coverage	$\Delta\eta \times \Delta\phi$	Coverage
Presampler	0.025×0.1	$\lvert\eta\rvert < 1.52$	0.025×0.1	$1.5 < \lvert\eta\rvert < 1.8$
Sampling 1	0.003×0.1	$\lvert\eta\rvert < 1.475$	0.025×0.1	$1.375 < \lvert\eta\rvert < 1.5$
			0.003×0.1	$1.5 < \lvert\eta\rvert < 1.8$
			0.004×0.1	$1.8 < \lvert\eta\rvert < 2.0$
			0.006×0.1	$2.0 < \lvert\eta\rvert < 2.5$
			0.1×0.1	$2.5 < \lvert\eta\rvert < 3.2$
Sampling 2	0.025×0.0245	$\lvert\eta\rvert < 1.475$	0.025×0.0245	$1.375 < \lvert\eta\rvert < 2.5$
			0.1×0.1	$2.5 < \lvert\eta\rvert < 3.2$
Sampling 3	0.05×0.0245	$\lvert\eta\rvert < 1.475$	0.05×0.0245	$1.5 < \lvert\eta\rvert < 2.5$

Table 3.1: **Summary of η coverage, cell granularity and longitudinal segmentation of the ATLAS Liquid Argon Electromagnetic Calorimeter.**

ATLAS LArEM is:

$$\frac{\sigma_E}{E} = \frac{10\%}{\sqrt{E}} \oplus 0.7\% \tag{3.5}$$

Hadronic Calorimeter

The ATLAS hadronic calorimeter [9, 16], similarly to all other sub-detectors, is divided in one barrel and two end-cap sections. The barrel is in turn divided in one central barrel part, extending in $|\eta|<1.0$, and two extended barrel parts which occupy the pseudo-rapidity region $0.8<|\eta|<1.7$, installed in each side of the central barrel. The barrel hadronic calorimeter is made of steel, which acts as absorber while for active material tiles of plastic scintillator are used. This is the reason why the barrel part is also called Tile Hadronic Calorimeter (TileCal). The tiles are only 3 mm thick, placed periodically inside the steel slab and the read-out of scintillation light is handled by optical wave length shifting fibers which are attached at the edges of the tile.

A sketch of one barrel TileCal module is shown in Fig.3.9. Full azimuthal coverage is achieved by installing 64 such modules around the beam axis. The inner radius of the barrel TileCal is 2.28 m and the outer one is 4.25 m. Longitudinally it is segmented in three compartments of 1.5, 4.1 and 1.8 interaction lengths (λ) and 1.5, 2.6 and 3.3 λ in the extended barrel. The TileCal granularity in the first and second compartments is $\Delta\eta \times \Delta\phi = 0.1 \times 0.1$ and 0.2×0.1 in the last one. It should be noted that all TileCal cells are projective i.e. they point towards the interaction point, as it is shown in Fig.3.10 where a sketch of the half TileCal barrel is illustrated.

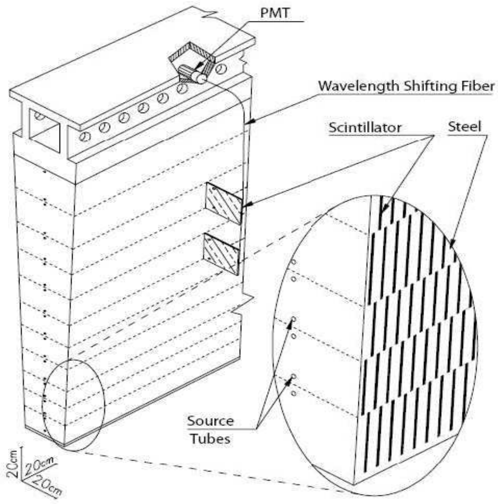

Figure 3.9: **Drawing of one tile calorimeter module** - Note that the scintillating tiles are placed perpendicularly with respect to the beam.

The allocation of TileCal compartments with the particular thickness in interaction lengths is very useful for particle identification and especially muons using calorimeter based criteria which act complementary to the standard muon reconstruction algorithms. This feature of the TileCal is exploited in this thesis for muon identification and estimation of the probability for catastrophic energy loss of muons in the calorimeters. These issues will be discussed in chapters 5 and 6.

Cables and services required by the detectors installed closer to the interaction point than the TileCal, result in the formation of two 60 cm gap regions between the central barrel and the extended barrels. These regions are only partially equipped with detecting material and they are called Intermediate Tile Calorimeter (ITC). They consist of special modules, made of steel-scintillator sandwiches and thin scintillator counters in the sectors where the available space in the gaps is even more limited. This region is also visible in Fig.3.10, where cells denoted as A, BC and D correspond to the first, second and third compartments respectively while D4, C10 and E cells constitute the ITC part.

In the hadronic end-cap calorimeter (HEC) and the region $1.5 < |\eta| < 3.2$, a

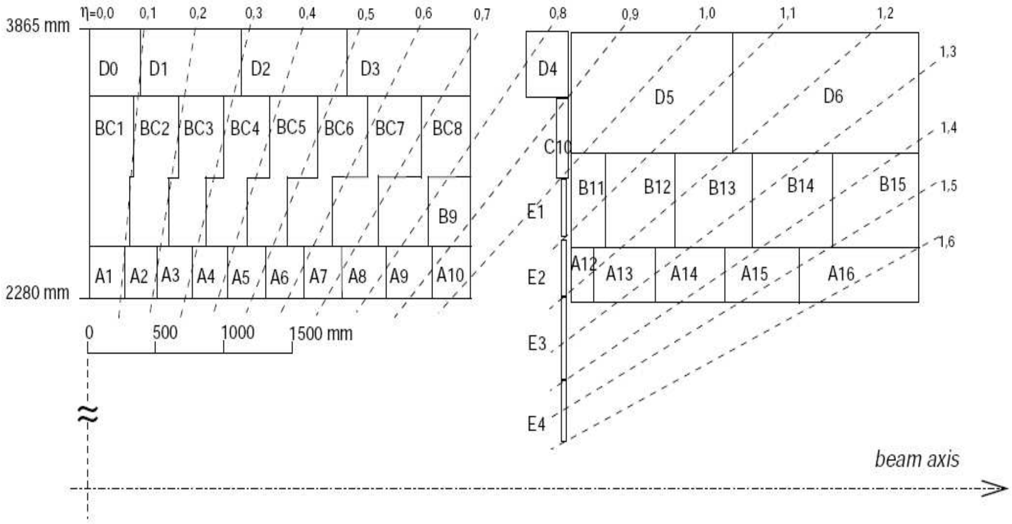

Figure 3.10: **Drawing of Tile Calorimeter half barrel and extended barrel** - The A, BC and D cells correspond to the three compartments of the TileCal. Also visible is the pseudo-rapidity coverage of each of the cells. Note the projective orientation of the cells with respect to the origin.

different technology is chosen because priority here is the radiation tolerance of the detecting devices. Copper is the absorber material and liquid argon is used as the active medium. The cell size here is $\Delta\eta \times \Delta\phi = 0.1 \times 0.1$ until $\eta = 2.5$ and double size in the rest of the HEC η coverage. Table 3.2 summarizes the η coverage, the granularity and radial segmentation of the hadronic calorimeter.

The expected energy resolution in the TileCal and HEC is:

$$\frac{\sigma_E}{E} = \frac{50\%}{\sqrt{E}} \oplus 3\% \qquad (3.6)$$

Forward Calorimeter

The ATLAS Forward Calorimeter (FCAL) occupies the pseudo-rapidity range $3.1 < |\eta| < 4.9$. This implies that FCAL is not used for precision measurements related to reconstructed tracks of charged particles since its coverage is well outside the acceptance of both the ID and MS which is $\eta = 2.5$ and $\eta = 2.7$ respectively. However, FCAL is as important as the rest of the CS system because it provides hermeticity in calorimetry thus reliable measurement of E_T^{miss} in each event and also jet energy measurements in the very forward regions of the detector.

Hadronic Calorimeter	**Barrel**		**End-cap**	
	$\Delta\eta \times \Delta\phi$	Coverage	$\Delta\eta \times \Delta\phi$	Coverage
Sampling 1 and 2	0.1×0.1	$\lvert\eta\rvert < 1.0$, $0.8 < \lvert\eta\rvert < 1.7$ in Extended	0.1×0.1	$1.5 < \lvert\eta\rvert < 2.5$
			0.2×0.2	$2.5 < \lvert\eta\rvert < 3.2$
Sampling 3	0.2×0.1		0.1×0.1	$1.5 < \lvert\eta\rvert < 2.5$
			0.2×0.2	$2.5 < \lvert\eta\rvert < 3.2$

Table 3.2: Summary of η coverage, cell granularity and longitudinal segmentation of the ATLAS Hadronic Calorimeter.

FCAL is installed in same end-cap cryostats with the other end-cap calorimeters and consists of three modules. The first two are made of tungsten and their purpose is measurement of the energy of hadrons while the last one is made of copper and it serves the electromagnetic measurements. Each module holds a metal frame which encloses electrodes placed systematically on the frame. The electrodes consist of rods at high voltage and grounded tubes and have parallel orientation with respect to the beam axis. Again, liquid argon that floods the space between the rod and the tube, is used as the active medium of the calorimeter. Overall, the thickness of FCAL in interaction lengths is $\lambda = 10$.

The expected energy resolution in the FCAL is:

$$\frac{\sigma_E}{E} = \frac{100\%}{\sqrt{E}} \oplus 10\% \tag{3.7}$$

3.2.4 Muon Spectrometer

Muons after passing through the calorimeters, are measured by the outermost ATLAS sub-detector the Muon Spectrometer [9, 17]. The goal of the MS is to detect muons in the pseudo-rapidity range $|\eta| < 2.7$ and trigger on them in $|\eta| < 2.4$. This can be done for muons of momenta of a few GeV up to momenta of the TeV scale and independently of the ID, providing thus the so-called "stand-alone" momentum measurement. In "stand-alone" mode, the desired resolution is of the order of $\sim 3\%$ for muons with transverse momentum of 50 GeV and approximately 10% for 1 TeV.

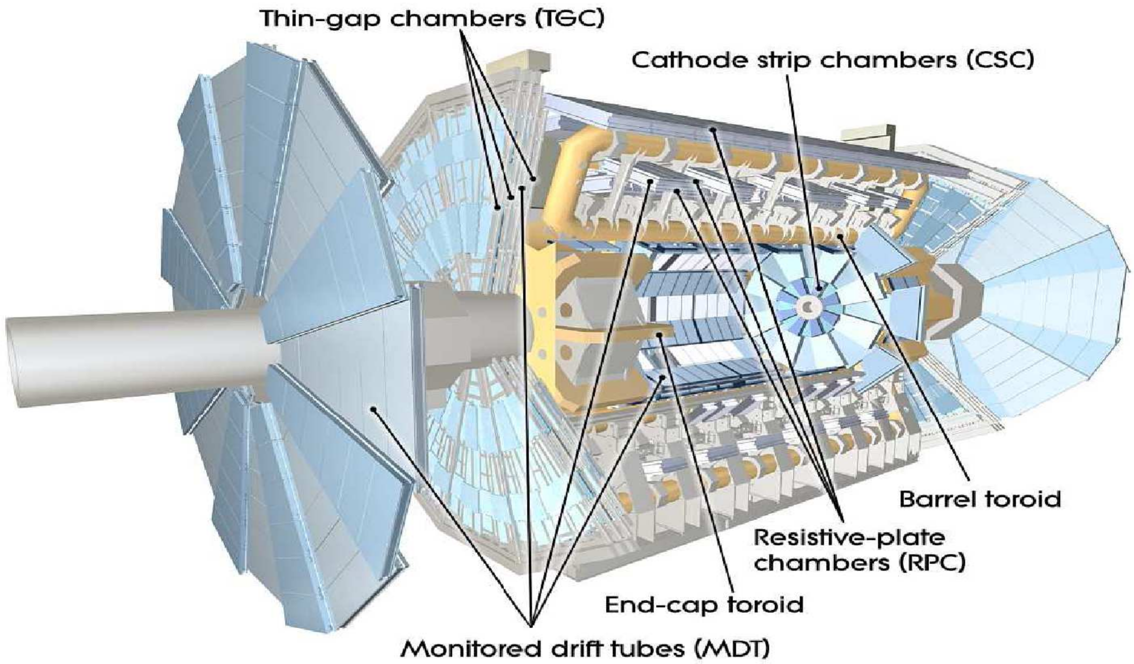

Figure 3.11: **Cut-away view of the ATLAS Muon Spectrometer** - The four different muon chamber technologies are shown. MDT, RPC, CSC and TGC.

Cost considerations, radiation tolerance and performance requirements, introduce the use of four different technologies of muon chambers:

- **Monitored Drift Tube – MDT.** They are the main detection element of the MS used for precise momentum measurement and tracking. They cover the pseudo-rapidity range $|\eta| < 2.7$ apart from the innermost end-cap layer where their coverage stops at $\eta = 2.0$. The whole MS comprises of 1200 MDT chambers.

- **Cathode Strip Chambers – CSC.** They serve the same objectives as the MDT's in the forward region, that is $2.0 < |\eta| < 2.7$, and only in the first tracking layer. In parallel, they provide trigger information in this region.

- **Resistive Plate Chambers – RPC.** They provide triggering and measurement of both coordinates (η and ϕ) in the barrel region ($|\eta| < 1.05$).

- **Thin Gap Chambers – TGC.** They are trigger chambers like the RPC's but installed in the region $1.05 < |\eta| < 2.4$.

An overall 3-dimensional view of the ATLAS MS is shown in Fig.3.11. In the barrel, MDT's are placed in cylindrical order around the beam axis forming three layers of chambers at distances from the interaction point of 5 m, 7.5 m and 10 m which are also called 'Inner', 'Middle' and 'Outer' stations. Their positions are symmetric in the ϕ plane and for this reason the whole barrel system can be divided in eight octants. In each octant there are two sectors called 'Small' and 'Large', the main difference of which is the lateral length that results in overlaps in the ϕ direction. The presence of overlapping chambers in the azimuthal direction diminishes the number of gaps in the coverage. A cross-sectional view of the MS is shown in Fig.3.12(a) and a side view in Fig.3.12(b).

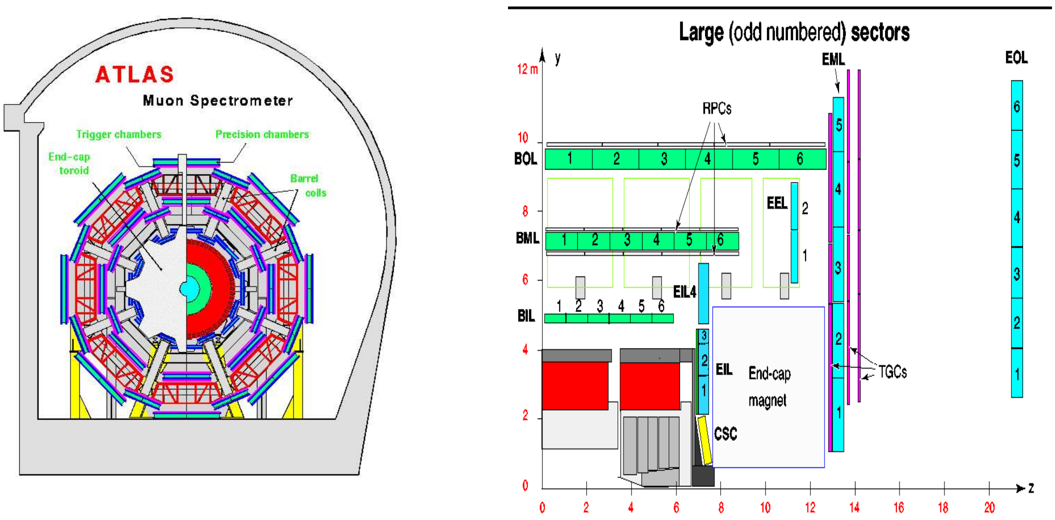

(a) Cross-sectional view of the Muon Spectrometer.

(b) Side view of the Muon Spectrometer.

Figure 3.12: **Cross-sectional and side views of the ATLAS Muon Spectrometer.**

The MDT chambers are named after the previously described pattern of 3 letters based on their location. First is B or E after Barrel or End-cap, second is the station I, M or O after Inner, Middle or Outer respectively and third is the lateral size L or S for Large and Small. For example, BIS, some properties of which are studied in chapter 4, stands for BarrelInnerSmall.

In the end-caps, chambers are installed on specially designed wheel-like support structures perpendicularly around the beam axis at distances 7.4 m, 10.8 m, 14 m and 21.5 m. The use of CSC's in the first concentric ring around the z-axis, is dictated by the harsh radiation environment of the forward region and the ability of CSC's to withstand larger particle fluences with less occupancy. A brief description of each chamber type operation principle is given in the following.

The Monitored Drift Tube technology

An MDT chamber is made up by several aluminum drift tubes arranged in rows called layers. One chamber is comprised of six or eight layers of tubes depending on the distance from the interaction point. Half number of layers forms one multi-layer which is separated from the other multi-layer by a mechanical spacer. A schematic representation of an MDT chamber is shown in Fig.3.13(a). Each drift tube is 29.97 mm in diameter, filled with a gas mixture of Ar/CO_2 (93 : 7) at 3 bar absolute pressure, flowing into the tube through a dedicated gas manifold system to which each tube is individually connected. In the centre of the tube and along its length, a tungsten-rhenium wire acts as the anode while the tube wall as the cathode in order to form a 3080 V potential difference. The diameter of the wire itself is 50 μm and two end-plugs are responsible for holding it at a stable position with respect to the tube.

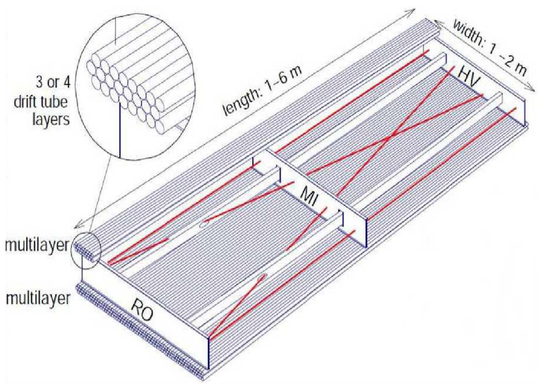

(a) Sketch of a Monitored Drift Tube chamber.

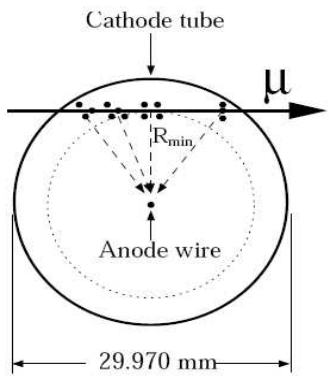

(b) Cross-sectional view of a drift tube.

Figure 3.13: **The precision muon chamber MDT technology.**

When a charged particle traverses the tube, ionizes the gas and liberates electrons from the gas atoms. Under the influence of the electric field, electrons start drifting towards the wire and at the same time ions drift in opposite direction towards the tube's wall. Primary electrons, while moving towards the wire, acquire more energy and cause the ionization of more atoms, creating an avalanche near the wire where the potential is highest. The secondarily produced ions drift toward the tube wall traversing the whole distance from the wire to the wall. The signal induced on the wire propagates to the end of the tube, where an amplifier followed by a discriminator feeds the pulse to the time-to-digital converter (TDC) installed on the chamber. Detailed description on the operation principle of the TDC and the signal formation are given in references [18, 19].

A measurement of the drift-time can be transformed into distance between the wire and the entering point of the initial charged particle using the so-called space-time relation which is characteristic of the gas mixture properties and the applied high voltage. Fig.3.13(b) illustrates the operating principle described above. The distance of closest approach to the wire (R_{min}) is the radius of the drift circle (dotted line) and the tangential line represents the muon's trajectory. It is therefore possible to gather the measured points (drift circles) from all the layers of the chamber and fit a straight line to them. This local straight line is called a track segment. Pattern recognition and track reconstruction are described in more detail in reference [17].

Simulation shows that the intrinsic tube resolution is on average $\sim 58\ \mu m$ much less than the design $80\ \mu m$ [19]. It should be noted though that when a charged particle passes near the wire, resolution drops because of the high drift velocity and due to the geometrical distribution of the ionisation clusters in combination with the fluctuations of the ionisation cluster size and position [19].

The Cathode Strip Chamber technology

The CSC's are multi-wire proportional chambers that substitute the MDT technology in the forward high activity regions. The CSC's are designed to provide high spatial and time resolution, measurement of two coordinates at high-rate environment. They are made of cathode planes segmented into strips in orthogonal directions. The plane with the strips perpendicular to the wires provides the precision coordinate while the one parallel to the wires provides the transverse (ϕ)

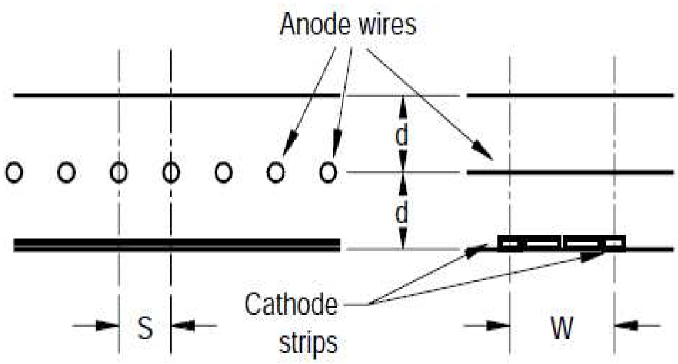

Figure 3.14: **Sketch illustrating the Cathode Strip Chamber technology -** The wire pitch S is equal to the anode-cathode spacing d = 2.54 mm. The spacing of the readout strips W is 5.08 mm.

coordinate. A schematic representation of the above is shown in Fig.3.14.

The chambers are filled with gas mixture of Ar/CO_2 (80 : 20) and ionization of the gas caused by the passage of a charged particle is transformed into an electron avalanche near the wires. The position of the track is obtained by interpolation between the charges induced by the avalanche on neighbouring cathode strips. The expected resolution of the CSC system is about 60 μm in the bending plane and 5 mm in the transverse coordinate. The ability to operate in high-rate environment is mainly due to the small electron drift times, which are of the order of 40 ns, resulting in timing resolution of 7 ns. This also allows the CSC's to be used as trigger chambers in this region.

The Resistive Plate Chamber technology

The RPC's are gaseous detectors which provide triggering for the MDT chambers and also two coordinate measurement. They are made of two parallel resistive electrode-plates of phenolic-melaminic plastic laminate which are separated by each other by insulating spacers forming a gas gap of 2 mm. The gap is filled with a mixture of $C_2H_2F_4$ (94.7/5/0.3) and the electric field, which is created between the plates, is about 4.9 kV/mm and allows the production of electron avalanches along the ionising tracks towards the anode. The signal is read out from metallic strips, which are mounted on the outer faces of the two resistive plates and are perpendicular to each other. These are called η and ϕ strips because η-strips are parallel to the MDT's wire and provide the η coordinate and ϕ-strips are orthogonal to the MDT's wire and give the second coordinate. The spatial resolution is roughly 1 cm while timing resolution is 2 ns. A schematic view of a cross section of an RPC is shown in Fig.3.15(a).

The Thin Gap Chamber technology

The TGC's are used for triggering and measurement of two coordinates similarly to the CSC system and they are installed in the end-cap region. They are multi-wire proportional chambers which consist of two cathode plates forming a 2.8 mm gas gap. The anode wires are located in the middle of the two plates and the distance from each other is 1.8 mm. The gas mixture used is $n-C_5H_{12}$ (n-pentane) and CO_2. The high electric field around the TGC wires and the small wire-to-wire distance lead to very good time resolution for the large majority of the tracks. Only tracks at normal incidence passing midway between two wires have much longer drift times due to the vanishing drift field in this region. This set-up is illustrated in Fig.3.15(b). The bending coordinate is measured by groups of TGC wires while the azimuthal coordinate is measured by the radial strips.

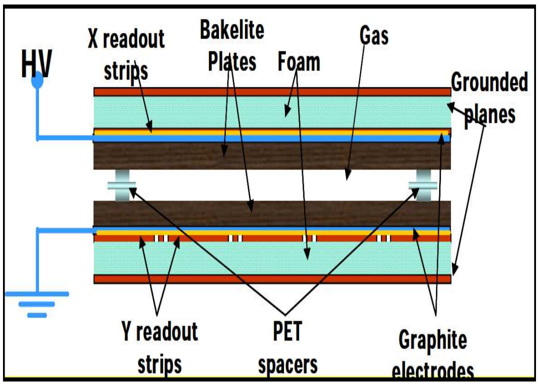

(a) Sketch illustrating the Resistive Plate Chamber technology.

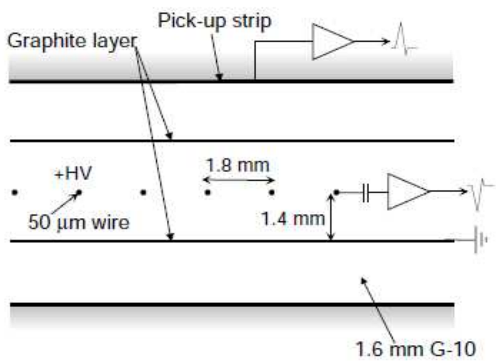

(b) Sketch illustrating the Thin Gap Chamber technology

Figure 3.15: **Schematic view of the RPC and TGC chamber technologies.**

Alignment system

The ATLAS muon spectrometer covers an area of about 5500 m^2 with detection elements. Although the construction quality ensures that the precision of individual elements (drift tubes) within a chamber and the chamber as a whole are high, does not account for the chamber deformations due to thermal gradients or gravity. In addition, the chambers are expected to be installed to their nominal positions with an accuracy of 5 mm and 2 $mrad$, however the resolution goal of the stand-alone muon momentum measurement can be achieved only if the precision on the relative alignment of chambers, within a projective tower and between stations in adjacent towers, is 30 μm. Because of these reasons, a sophisticated alignment system is deployed, which consists of approximately 12000 precision-mounted alignment sensors that continuously monitor both the internal chamber deformations and their relative positions within projective towers and adjacent stations. Fig.3.16 illustrates the concept of the optical alignment system used in the MS.

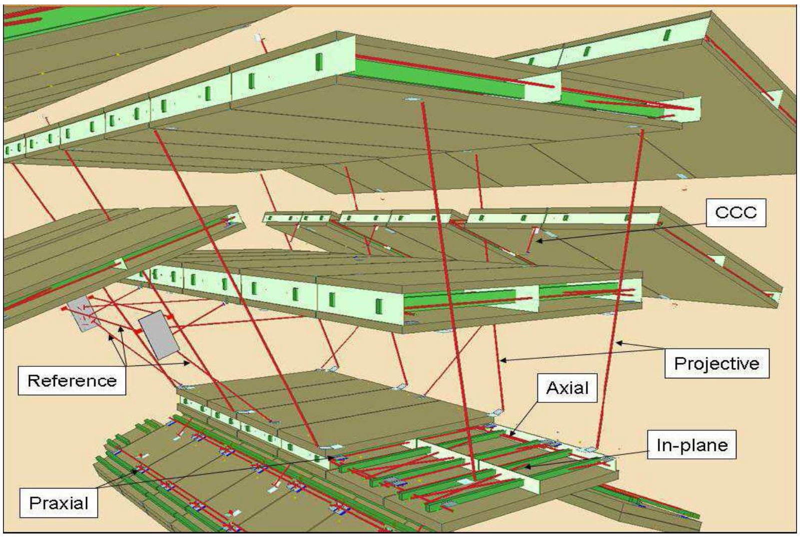

Figure 3.16: **Layout of the optical alignment system for three adjacent barrel sectors** - The alignment system for the muon spectrometer chambers includes axial, praxial, in plane and relative alignment.

Apart from the relative alignment of the MDT chambers themselves, it is also necessary, for reconstruction and momentum measurement of muons, to know the absolute position of the MS with respect to the ID and CS. For this reason, complementary to the optical alignment system, there are track based alignment algorithms which exploit the approximate straight trajectories of high-p_T muons.

The alignment system has been extensively tested in the combined testbeam setup of the H8 experimental area at CERN during 2003 and 2004. More information about the alignment tests held during the H8 physics program can be found in reference [20].

3.2.5 Trigger System

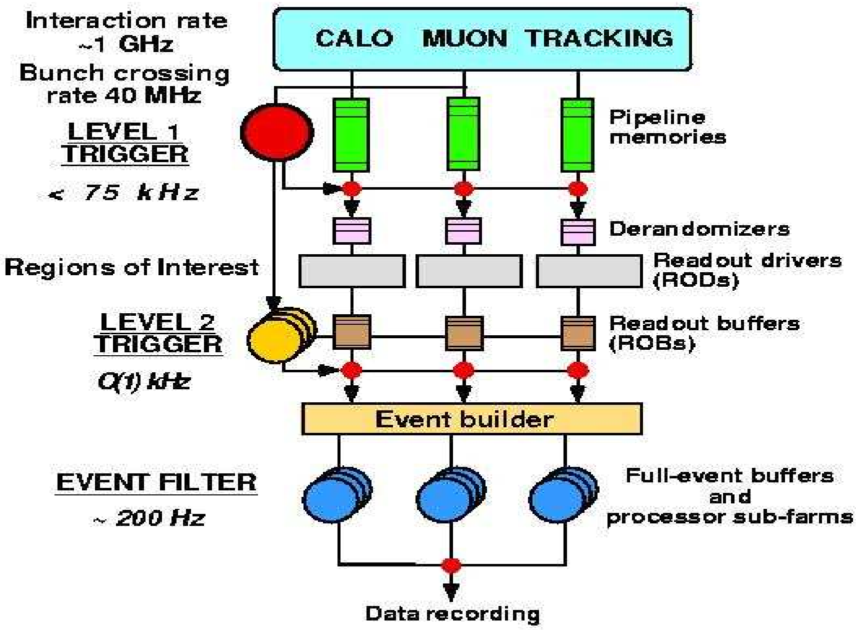

Figure 3.17: **The ATLAS trigger architecture concept** - It consists of three distinct levels, LVL1, LVL2 and EF. The last two constitute the so-called High Level Trigger (HLT).

There are three levels constituting the ATLAS trigger system which are called Level 1 (LVL1), Level 2 (LVL2) and Event Filter (EF). LVL1 receives data from the MS and CS systems only, at the bunch crossing rate of 40 MHz and produces a significantly reduced output rate of 75 kHz. While the LVL1 decision is processed, incoming data are queued in pipeline memories. The main purpose of LVL1 is to select events of interest by searching and combining candidates with specific physics criteria. This is done in the central trigger processor, which implements a "trigger menu" made up of combinations of trigger objects, e.g one muon with $p_T > 20\ GeV$. At the same time, LVL1 passes the Regions-of-Interest (RoIs), which are the detector locations in η and ϕ, where the previously described objects have been identified. It takes less than 2.5 μs for LVL1 to take a decision.

After LVL1 decides if an event contains interesting objects, RoIs are passed to LVL2. The latter uses full granularity from all detectors, refines the data selected by LVL1, using also a dedicated trigger menu, and in approximately 10 ms decides whether an event should proceed to the EF. LVL2 reduces the event rate down to $\sim 3.5\ kHz$.

The Event Builder collects all data from the Read Out Buffers (ROB's) of the detectors every time an event passes LVL2 trigger. At this level the event undergoes full analysis and it is decided in about 4 s on average, if the event should be written out to permanent storage and becomes available for offline analysis by the scientific community. The EF is designed to finally reduce the event rate down to roughly 200 Hz. The key elements of the trigger flow described above are illustrated in Fig.3.17.

3.3 The ATLAS Software Framework

In order for physicists to perform offline analysis on the huge amount of data produced in an experiment, combine the observables that are recorded from the read out systems, such as hits or energy depositions and identify the physics processes in each event, it is necessary to build a robust and common analysis software framework. The analysis software framework of ATLAS is called ATHENA [21].

ATHENA is a control framework based on a component-based architecture called Gaudi, which was initially develop by the LHCb experiment and is now developed by both ATLAS and LHCb. Some of the basic design principles under which ATHENA is developed are:

- The use of abstract software interfaces which makes easy to handle groups of components that share the same interface
- The clear separation between data and algorithms so that a client of the data

is not exposed to the machinery of the creator algorithm itself and as a result, possible changes to the algorithm are transparent to the client

- The classification of data with respect to their lifetime inside the software flow and with respect to the storage type which can be persistent or transient. Persistent means that data are permanently stored on disk and transient that they are stored temporarily on memory

Some of the most important components within the Athena framework are explained in what follows whereas in Fig.3.18 a sketch of the various components and the linking between them is shown:

Algorithms Algorithms are responsible for the necessary analysis of the event and they have both inputs and outputs. Example of an algorithm is a track reconstruction algorithm which takes the detector response as input and provides an object of a reconstructed track that carries basic parameters like impact parameter, momentum or η and ϕ coordinates. The sequence of the algorithms called in each event and also the input and output data are handled by the framework in such a way that one algorithm can access the data of another algorithm.

Tools A tool has the same functionality like an algorithm, it can act on data or produce new data but, in contrast to algorithms, it can be called many times in each event. Tools can be called inside the program flow by an algorithm, using the framework's dedicated service. Usually the role of tools is complementary to that of the algorithms because they perform more specialized tasks.

Services A service provides common functionalities for both algorithms and tools such as messaging service which controls the output of messages sent by the developers. It can be used in different verbosity levels which can be specified by the developer. Other services are used for histogram and N-tuple creation. The histogram service is used for booking, filling and manipulating histograms inside the framework in a coherent way whereas the N-tuple service is responsible for creating the file format which will contain all the information needed to perform physics offline analysis by a physicist. The N-tuple is a file format that is readable from the ROOT analysis framework [22].

Job Options Service The Job Options service handles user defined properties of algorithms, tools or services during run time. The declarations of properties is done via python scripts (JobOptions files) that exist in every software package. For example, a threshold on the acceptable level of noise in a calorimeter cell when measuring the energy deposition of a track in the CS can be set in the JobOptions file. The basic advantage of this approach is that apart from the possibility to adjust properties during run-time, the user does not have to recompile the code in order for the change to take effect.

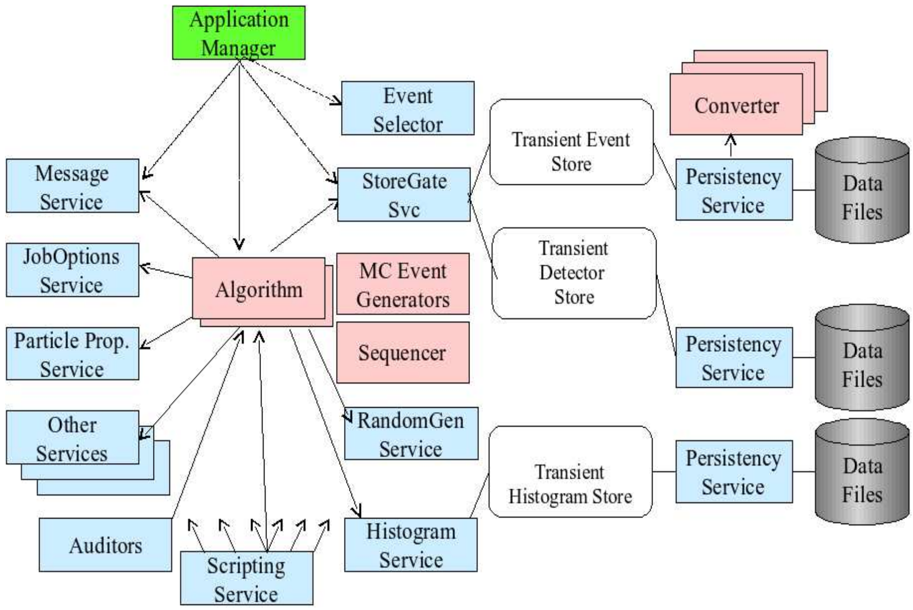

Figure 3.18: **The Athena Framework component model** - Some of the basic components are explained in the text.

As soon as the LHC physics program commences, the objective of the ATLAS software will be the reconstruction of the real proton-proton collisions. In the meanwhile though, physics studies are performed with simulated data. It is the responsibility of the ATLAS software to produce and analyse the simulated data. The steps followed towards this objective are described briefly in the following:

Event generation The event generation is actually the simulation of proton on proton collisions using all the known physics laws. This includes the calculation of the position and momentum 4-vector of all particles participating in a collision event, that is the interacting and spectator partons and all the produced particles. The most commonly used programs, also called Monte Carlo (MC) generators are Pythia [23], Madgraph [24] and Isajet [25]. Usually generators are configured to produce only one particular physics process (e.g $H \rightarrow ZZ \rightarrow \ell\ell\ell\ell$) which eases studies from the corresponding physics groups or just single particles to perform detector and algorithm performance related studies.

Detector simulation At this stage the passage of all previously generated particles through the ATLAS detector is simulated. This task is carried out by an ATLAS specific version of the GEANT [26] software package. The impact of magnetic field and interaction with detector material are taken into account during simulation. The interaction of particles with the active medium of the detector is represented by the so-called 'hit' which contains information on the position and energy loss of the particle.

Digitization After hits in each sub-detector are produced, the detector and electronics response is simulated, taking into account the intrinsic resolution of the particular detection element. The output of the digitization step is identical to the output expected from real collisions. From this step onwards there is no separation between MC and real data.

Reconstruction Data from the digitization process are passed to the reconstruction algorithms. There is a broad spectrum of algorithms, each one performing specific tasks like pattern recognition, track fitting, vertex reconstruction and energy measurements. The end user is exposed however only to the output of the reconstruction process.

There are several types of output containing the event variables and observables that can be used for offline physics analysis. Fundamental types are the Event Summary Data (ESD) and the Analysis Object Data (AOD) [27]. The ESD contains detector level calibrated quantities such as calorimeter cells and ID hits, in addition with the reconstruction objects built from them such as calorimeter clusters and tracks. The AOD is smaller in size than the ESD (100 kB/event and 500 kB/event respectively) because it contains high-level physics objects useful for physics analysis, such as particles with associated tracks.

Apart from the previously mentioned data formats there is also the Derived Physics Data (DPD) format which is technically equivalent with the AOD but differs significantly on the physics information it contains. DPD's are in fact a lighter version of AOD's since they are created from the AOD information by applying stricter event selection (skimming), reducing in size the information per object (slimming) and excluding some of the non important features, regarding the particular analysis, of data objects (thinning).

3.3.1 Track representation in the ATLAS software framework

The need to describe the path of a particle through the detector is fulfilled by the introduction of common C++ track objects. The track objects are filled by reconstruction algorithms with information regarding the particle's trajectory organized in one or multiple sets of parameters. These parameters are always expressed with respect to a surface which in turn represents a specific area of the detector. The parametrization of the track with respect to a surface can be done in various ways but if a particle is moving inside a magnetic field, at least five parameters are needed to provide a complete and unambiguous parametrization with respect to any given detector surface. This is the concept of the so-called `TrackParameters` base class.

In ATLAS objects of the `TrackParameters` base class exist for every type of surface and parametrize the track locally on the surface with five parameters:

$$L_i = (l_1, l_2, \phi, \theta, q/p) \tag{3.8}$$

where l_1 and l_2 represent the local coordinates on the surface, ϕ is the azimuth angle, θ is the polar angle which relates to η through equation 3.3 and q/p is the inverse momentum multiplied by the charge q. Specific classes for local representations of `TrackParameters` exist for every surface type in the tracking Event Data Model (EDM). The most common representation is the one given at the perigee, which is defined as the point of closest approach to the beam axis. In the perigee representation case, l_1 and l_2 above correspond to the transverse and longitudinal impact parameter d_0 and z_0, respectively.

An exhausting description of the tracking EDM in ATLAS is given in reference [28].

4

BIS muon chamber and LArEM calorimeter combined reconstruction in the H8 testbeam

4.1 The H8 combined testbeam experimental area at CERN

During the summer of 2004 a large test stand of all the ATLAS sub-detectors was operated at CERN in the H8 beam line. The data taking program of this period was actually the summit of an effort that had started already in 2000. However, this particular period was unique because it was for the first time that final production barrel parts of each ATLAS sub-detector were operated together, naming the H8 beam line after Combined TestBeam (CTB). It was also the last time this was happening before the sub-detectors were finally installed to the experiment.

The CTB setup in 2004, not only did it resemble the geometry and setup of approximately one octant or one full barrel slice of the ATLAS detector but it was also complemented by an octant of end-cap MS chambers. A schematic representation of the H8 CTB as in 2004 is given in Fig.4.1. In the following sections a brief description of the H8 beamline and the experimental setup of the CTB is given along with the special setup that included a BIS type muon chamber. Very detailed descriptions of the beam properties and experimental setup can be found in references

[20, 29, 30].

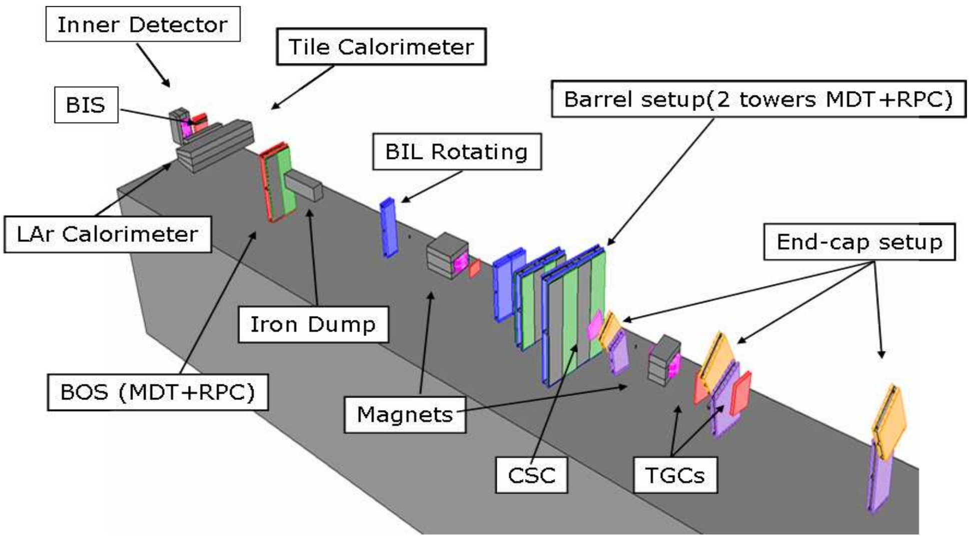

Figure 4.1: **Schematic view of the H8 Combined Testbeam** - Visible on the figure are the two magnets used for particle trajectory bending, the various technologies of the MS chambers and the ID and calorimetric modules.

4.1.1 Beam creation and properties

The particle beam type used for studies at the CTB was $e^{\pm}$, $\pi^{\pm}$ or $\mu^{\pm}$. These beams were created from a 400 GeV proton beam delivered by the SPS to a primary beryllium target of 30 cm thickness. The intensity of the proton beam was roughly 10^{12} protons per spill, hitting the target every 16.8 s while the duration of the spill was approximately 4.8 s. The emerging beam from this target was subsequently directed to the H8 beam line where using dedicated magnets, collimators and other targets it was possible to create different particle type beams with energies in the range of 1 GeV to 350 GeV.

4.1.2 Experimental setup

The experimental setup of the 2004 H8 CTB consisted of three major detector systems of ATLAS, the inner detector, the calorimeter and the muon system. In various locations along the sub-detector line there were also other instrumentation elements not serving detection purposes, providing, nevertheless important services like triggering or bending magnetic fields, required for the smooth functionality of the CTB. The ID was the first system installed in the direction of the beam path, composed of three layers of silicon pixel modules, followed by four layers of the SCT's silicon micro-strip modules and two wedges of the TRT. The Pixel and SCT elements were all placed inside a magnet which produced a magnetic field of 2 T similar to the magnetic field created in ATLAS by the solenoid magnet.

For calorimetry, an electromagnetic LArEM calorimeter module was placed inside a cryostat and three TileCal modules were attached at the back side of the cryostat. The whole calorimetric system was placed on a platform that could perform translations and rotations with respect to the beam axis in order to expose the desired calorimeter cells to the incident beams.

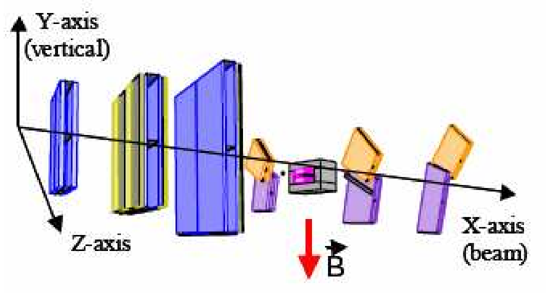

Figure 4.2: **The H8 testbeam coordinate system.**

Before carrying on with the description of the experimental setup it is important to introduce at this point the coordinate system used in the H8 as it will be used many times in the following. Care was taken for the coordinate system used in H8 to resemble the coordinate system used in ATLAS (see chapter 3 and Fig.3.2). As it is shown in Fig.4.2, the positive y-axis was pointing up, the positive x-axis was running along the H8 beam and the z-axis was horizontal, with the positive side running towards the right edge of the detectors as they were seen by the beam. The point $x = y = z = 0$ was lying on the entrance surface of the inner detector magnet. Given this reference system, translations of the calorimeter platform were along the z-axis while rotations were performed around the y-axis.

Right after the calorimetric platform there was a 3.2 m long block of iron dump which was used to prevent all particles except muons, from reaching the muon chambers installed further upstream. Immediately after this slab of iron, there was one BIL type MDT chamber sitting on a rotating support structure, which allowed the rotation of the chamber up to ±15 degrees with respect to the beam, around the y-axis. This was necessary because the rotating BIL chamber was used for the extraction of chamber space-time relations, that were afterwards utilized by all other MDT chambers. The rotation ensured the increase of the angular spread of muon tracks which is needed for the extraction of the $r-t$ relation. A description on how the $r-t$ relations were extracted for the H8 CTB can be found in reference [20].

Further upstream, one barrel and one end-cap part of the MS were installed. A sketch of the MS stand is shown in Fig.4.3. The barrel part of the MS consisted of six MDT chambers arranged in doublets of BIL, BML and BOL types, fully equipped with Front-End electronics and optical alignment systems.

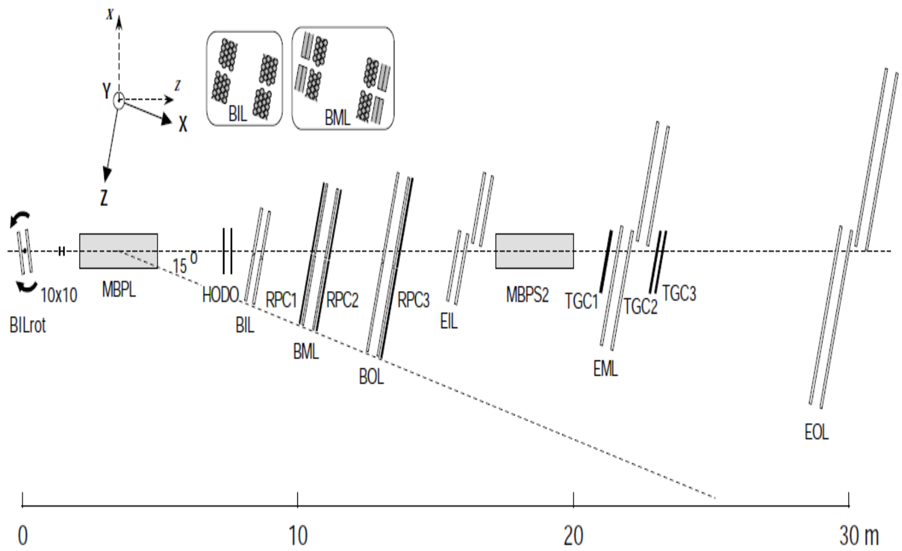

Figure 4.3: **Schematic layout of the muon stand in the H8 testbeam** - Visible are also the two bending magnets (MBPL and MBPS2) and the trigger scintillators.

The orientation of the chambers with respect to the beam was vertical, thus the precision coordinate in the CTB was the z-axis. There were also six RPC chambers. Four of them sandwiching the BML MDT doublet and the other two were installed in the back side of the BOL doublet, as seen by the beam.

The end-cap stand consisted of six MDT chambers of both Small and Large types; two EI, two EM and two EO also fully equipped. The end-cap trigger chambers were also tested by installing one triplet and two doublets of TGC chambers.

Track bending in the MS stand was possible by two magnets, called MBPL and MBPS2, also visible in Fig.4.3. The first one was located before the MS stand and the second one between the EI and EM chambers. Both magnets were able to create a ranging magnetic field with maximum bending power of $\int Bdl = 3.54\ Tm$.

Finally, triggering in the CTB was provided primarily by two scintillator configurations, although in some of the runs trigger chambers themselves were used. The first setup consisted of two small area scintillators, $10 \times 10\ cm^2$, positioned at the very centre of the beam line and in front of the MBPL magnet. The second larger one, also called hodoscope trigger, was made up by two planes of six scintillator slabs of $10 \times 100\ cm^2$ each, placed right before the muon chamber barrel stand.

4.1.3 The Barrel Inner Small MDT muon tracking chamber

The Barrel Inner Small, BIS, muon tracking chamber which was used in the current study at the H8 testbeam, is one of the 130 BIS chambers that were constructed by the collaboration of three greek universities; the University of Athens which performed the tube assembly [31], the National Technical University of Athens which performed the quality assurance and quality control of the tubes [32, 33] and the Aristotle University of Thessaloniki where the chambers were assembled [34, 35].

The BIS are the innermost MDT muon chambers located in the small sectors of the inner station, between the Tile Calorimeter and the barrel toroid coil cryostats and have dimensions of 1 m in z-coordinate and 1.7 m in azimuthal direction. They consist of 2 multi-layers of tubes of 4 layers each and the 2 multi-layers are separated from each other by a 6 mm spacer. The position of the tubes in the chambers during construction was controlled well within the requirements, to better than $10-15\ \mu m$.

4.1.4 The special experimental setup with the BIS chamber

During the summer of 2004 a special experimental setup was used in H8. One BIS type muon chamber was installed in front of the calorimeters, right after the TRT detector. It was actually mounted on a the calorimeter platform in not exactly perpendicular position with respect to the beam but rotated around the z-axis by approximately 11.5 degrees. This setup ensured that the position of BIS with respect to the beam followed the movements of the calorimeters and the rotations and translations of the table exposed BIS at different beam incident angles. In the photograph of Fig.4.4 the BIS chamber installation position is visible with respect to the TRT and the LArEM calorimeter.

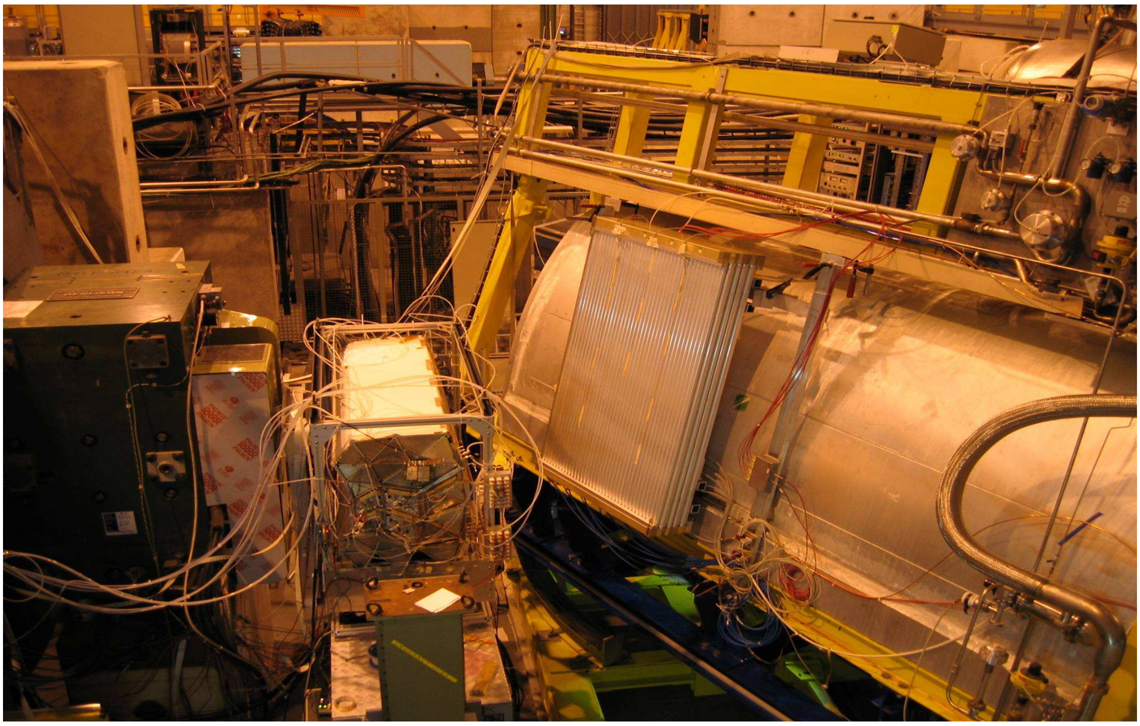

Figure 4.4: **Photograph of the BIS chamber mounted on the calorimeter platform in the H8 testbeam** - Also visible on the photograph is the ID magnet and the TRT right after it.

This setup provided the opportunity for studies on the performance of the chamber in an environment that included muon and positron beams. Note that this setup also provided the means for studies on specific LArEM calorimeter properties. The reconstruction of track segments under these conditions and their correlation with the calorimeter cluster barycentre is discussed in the following sections.

4.2 Track segment reconstruction with BIS

4.2.1 Runs with positron and muon beam

Table 4.1 lists the CTB runs that are used here to study the track segment reconstruction potential of the BIS chamber, in the special experimental setup and the correlation of this track with the calorimeter cluster barycentre. There are seven runs with positron beam of $E = 180\ GeV$ and one run with muons of $E = 350\ GeV$. The positron runs vary in steps of 0.1 in η, covering the range $0.1 \leq \eta \leq 0.7$. The incremental rise of the pseudo-rapidity allows to test the reconstruction of track segments and their correlation with the calorimeter cluster barycentre at steep beam incident angles. The calorimeter platform position in the muon run is $\eta = 0.55$.

Run Number	Beam Type	Beam E [GeV]	Table η
2102459	Positrons	180	0.1
2102470	Positrons	180	0.2
2102478	Positrons	180	0.3
2102488	Positrons	180	0.4
2102511	Positrons	180	0.5
2102537	Positrons	180	0.6
2102523	Positrons	180	0.7
2102731	Muons	350	0.55

Table 4.1: **Runs used for analysis with the BIS chamber in H8 CTB.**

4.2.2 The BIS muon chamber in Athena testbeam reconstruction

As it has already mentioned before, in order to perform track segment reconstruction, pattern recognition algorithms require information on the distance between the tube's wire and the actual particle's trajectory inside the tube, the drift radius (see Fig.3.13(b)). The TDC's located on the mezzanine cards that equip an MDT chamber, record the drift time of each hit and then this time is transformed into distance by the $r - t$ relation. These steps occur inside the Athena framework by dedicated software packages and services. In the CTB the drift time of the individual tube is calculated by the formula:

$$t_{drift} = (A - B + C - t_0) \times D \qquad (4.1)$$

where A is the number of TDC counts from the readout mezzanine card of the muon chamber. The trigger time B, is the time when the muon passed the trigger scintillators and in CTB this information was provided by a dedicated trigger mezzanine card located in the vicinity of the EOL chamber. Parameter C is an offset particular to the H8 muon stand configuration which ensured that the time window in which data from the MDT chambers were searched for, took into consideration all the chambers in H8. The t_0 term corresponds to the time offset of each electronic channel and is calculated from the TDC spectrum at approximately half rise of it. Finally, $D = 0.78$ is the transformation factor from TDC counts to $nsec$. In the CTB, files containing t_0 values were extracted for each chamber and each tube. These files were accessed by ATHENA services during run time and were used as input for the t_{drift} calculation based on equation 4.1.

For the BIS chamber, it was necessary to produce new t_0 files that would be used during reconstruction run time in ATHENA . Values of t_0 are extracted from fitting to the drift time spectrum the following empirical 3-parameter sigmoid function:

$$f(x) = \frac{\alpha}{1 + e^{\frac{t_0 - x}{\beta}}} \tag{4.2}$$

The fit was performed to the drift time spectrum of the tube that was most illuminated by the beam in each layer. Since the beam was impinging BIS at a fixed point, the beam spread was such that it illuminated, providing sufficient statistics, only one or two tubes in each layer. This is also seen in the a typical beam profile of the BIS chamber which is given in Fig.4.5(a) for all layers and in Fig.4.5(c) for one layer. An example of a fit, using equation 4.2, to the drift time spectrum of the most illuminated tube of BIS is shown in Fig.4.5(b). Note that the $r - t$ relation used for the BIS was the $r - t$ relation used by the rest of the muon chambers in CTB.

Track segment reconstruction was performed inside ATHENA using Muonboy reconstruction software package, which was especially configured to account for the geometry of the CTB and in particular the position of the BIS chamber. During reconstruction, Muonboy receives the required information about the drift radius and its error, computed for any hit in the muon chamber, which is provided on request by a devoted ATHENA service (MdtCalibService). With the information on

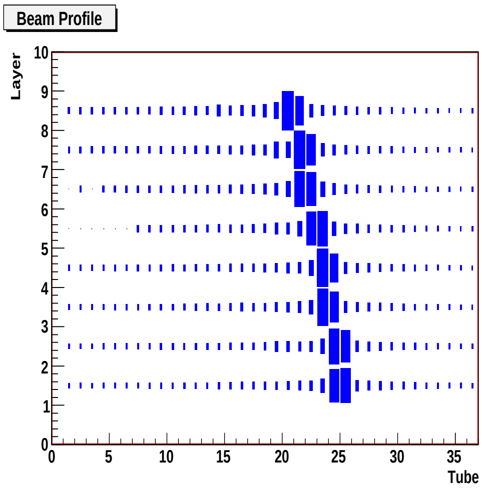

(a) Example of beam profile in the BIS chamber from run with positron beam impinging at $\eta = 0.6$.

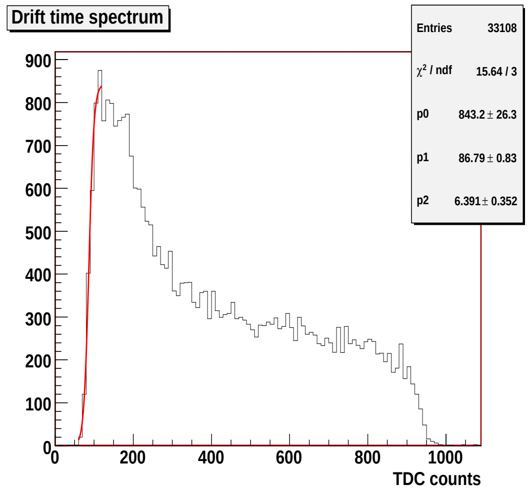

(b) Example of fit to the drift time spectrum on the most illuminated tube in the BIS chamber.

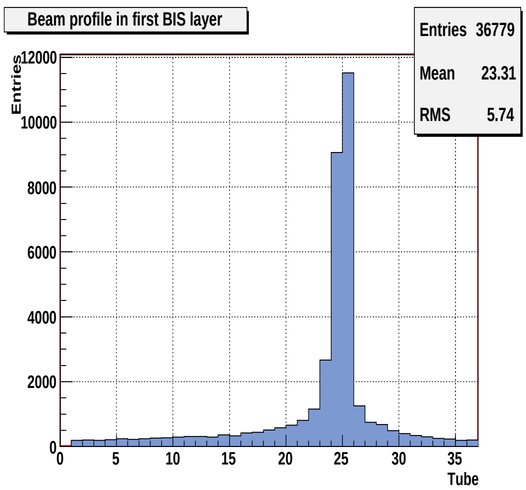

(c) Example of beam profile in one layer of the BIS chamber

Figure 4.5: **Examples of beam profile in BIS chamber and fit to drift time spectrum for extraction of t_0 values.**

the drift radius Muonboy tries to fit the best tangential line, the track segment, to the drift circles. Details on the reconstruction algorithm followed in Muonboy can be found in references [17] and [36].

4.2.3 Selection of reconstructed track segments

The initial attempt to reconstruct track segments was not successful. The problem is illustrated in Fig.4.6 where the drift time distribution of hits that constitute the reconstructed track segments is shown. There is a clear shift of the distribution of roughly 200 *nsec* which means that the drift radius passed to the reconstruction algorithm from the calibration service was incorrect. Given the special position of the BIS chamber, which was about 25 *m* away from the MS stand, in equation 4.1 the offset C had to be modified in order to account for the position of the BIS chamber also. Therefore, a correction for this shift was applied in order to bring the drift time distributions start at zero.

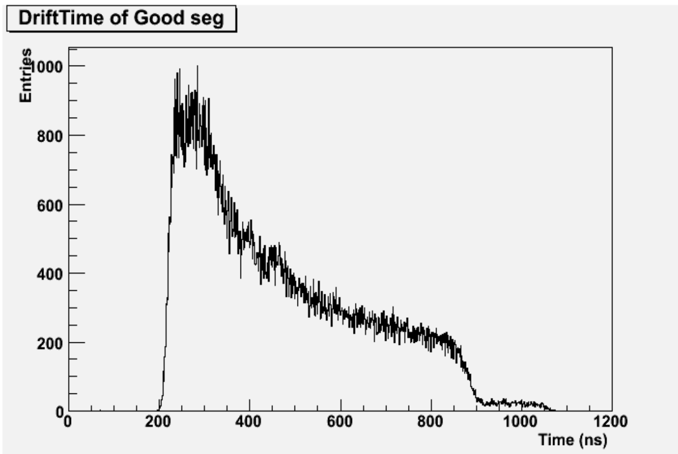

Figure 4.6: **Drift time distribution of hits in selected track segments** - The observed shift of $\sim$ 200 nsec is due to the wrong offset used in the calculation of the drift time. The distribution is obtained from hits of selected track segments (see text)

In Fig.4.7(a) the energy deposited in the Tile calorimeter is plotted with respect to the energy deposited in the LArEM calorimeter, for each event. The figure corresponds to the positron run number 2102511 and similar plots are obtained from the rest of the runs. The first step towards reconstructing track segments is to select the events that exhibit an energy loss in the calorimeters that indeed corresponds to positrons because as it can be seen in the figure there is also contamination from other particles whose energy deposition signature is compatible with muons and pions. Muons are expected to leave very little energy in the calorimeters while pions leave significant amounts of energy in both calorimeters. Positrons on the other hand, are expected to deposit all their energy in the LArEM. Therefore, a first selection of events is done requiring the total energy deposited in the LArEM to be greater than 160 GeV and in the TileCal to be less than 3 GeV. The same type of plot is given in Fig.4.7(b) for the muon run. Here events with muons are selected by requiring the total energy deposited in the LArEM to be less than 3 GeV and in the TileCal to be less than 5 GeV.

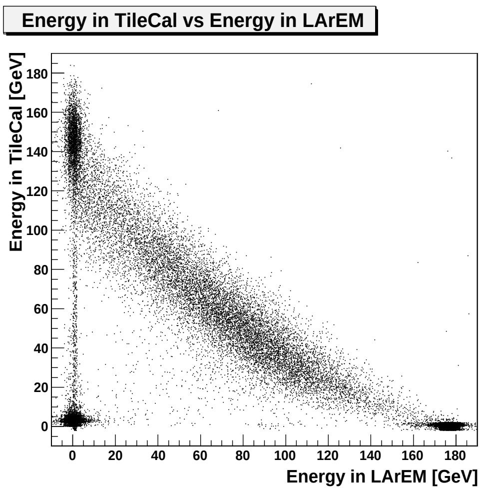

(a) Energy deposited in TileCal versus energy in LArEM calorimeter in positron run 2102511.

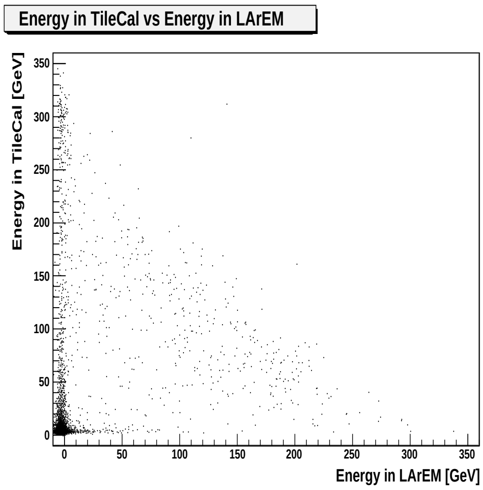

(b) Energy deposited in TileCal versus energy in LArEM calorimeter in muon run.

Figure 4.7: **Energy deposited in TileCal versus energy deposited in LArEM calorimeter from positron and muon runs.**

After selecting events which the energy deposition in the calorimeters is compatible with positrons or muons, the reconstructed track segments in the BIS chamber are analysed. In the plots of Fig.4.8 the number of reconstructed segments per event and the number of hits on the segment is shown for all runs with positron beam. The striking feature of these distributions is the large tail above 1 in the number of segments reconstructed per event while the number of hits is below 5 on most of the segments. An explanation of this feature lies in the fact that positrons are likely to produce secondary photons through bremsstrahlung as they pass through the material of the muon chamber itself but also in the material of the ID before reaching BIS, therefore giving rise to showers of particles. These showers of particles produce a big number of hits on the BIS chamber in each event and the excessive hit multiplicity finally results in an increase of the possible combinations which form a track segment. This is also justified by the plots in Fig.4.9 that follow.

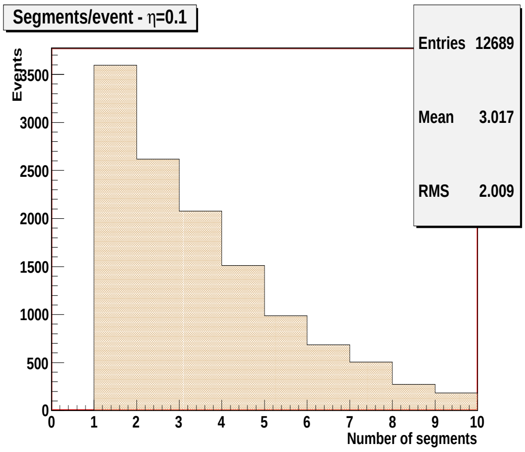

(a) Number of reconstructed track segments per event. Positron run at $\eta = 0.1$

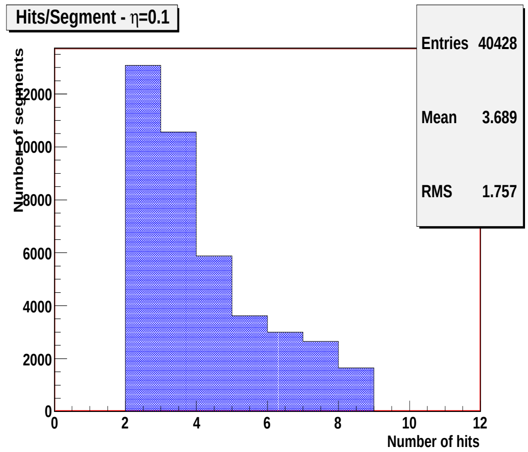

(b) Number of hits on segment. Positron run at $\eta = 0.1$

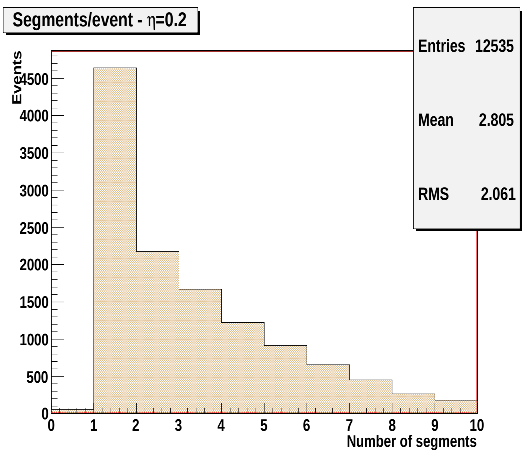

(c) Number of reconstructed track segments per event. Positron run at $\eta = 0.2$

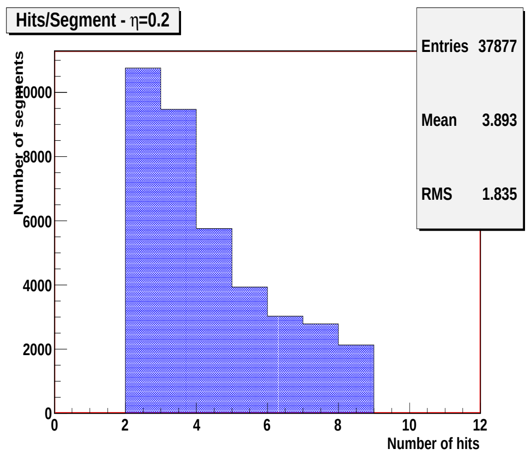

(d) Number of hits on segment. Positron run at $\eta = 0.2$

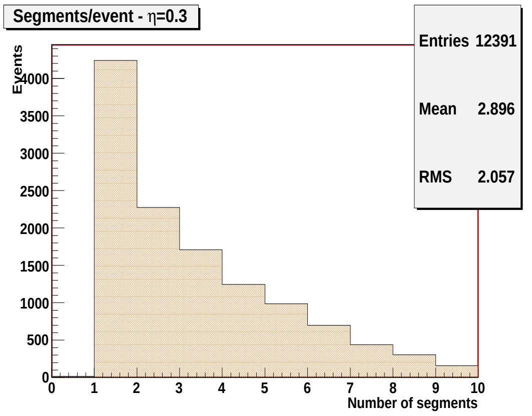

(e) Number of reconstructed track segments per event. Positron run at $\eta = 0.3$

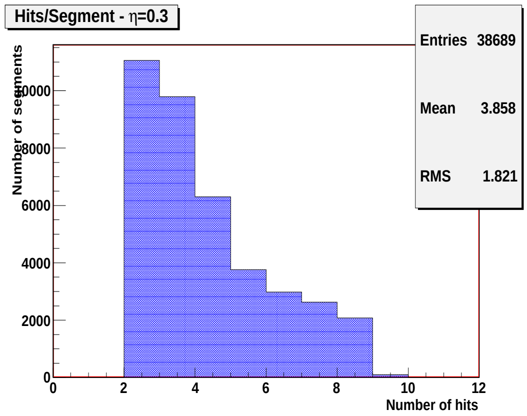

(f) Number of hits on segment. Positron run at $\eta = 0.3$

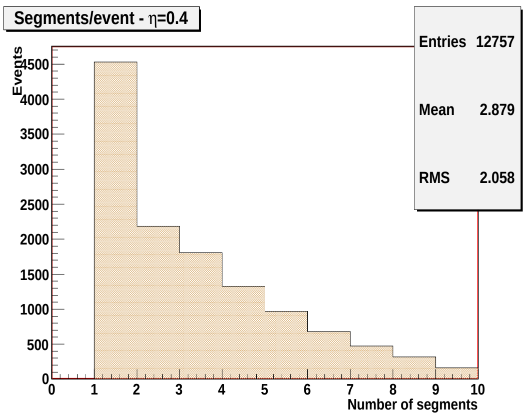

(g) Number of reconstructed track segments per event. Positron run at $\eta = 0.4$

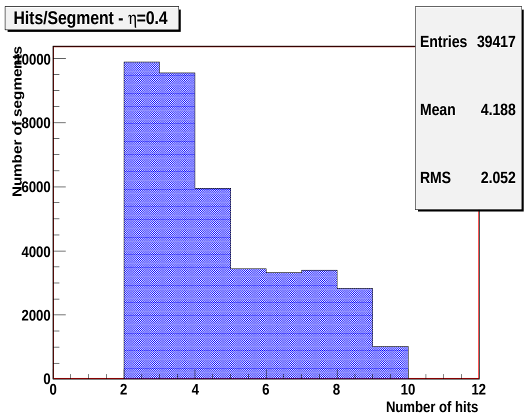

(h) Number of hits on segment. Positron run at $\eta = 0.4$

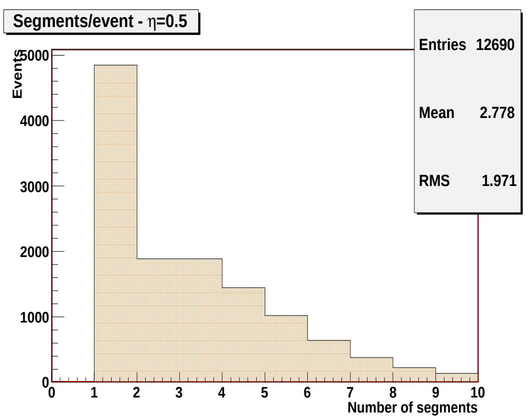

(i) Number of reconstructed track segments per event. Positron run at $\eta = 0.5$

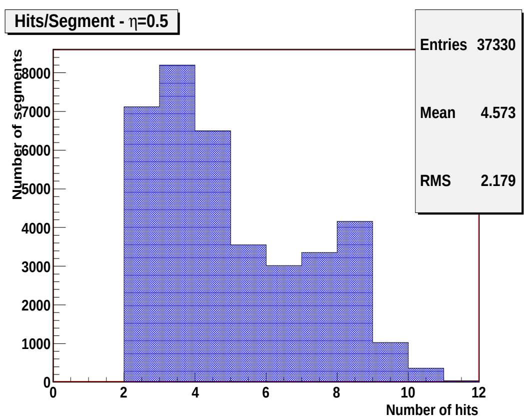

(j) Number of hits on segment. Positron run at $\eta = 0.5$

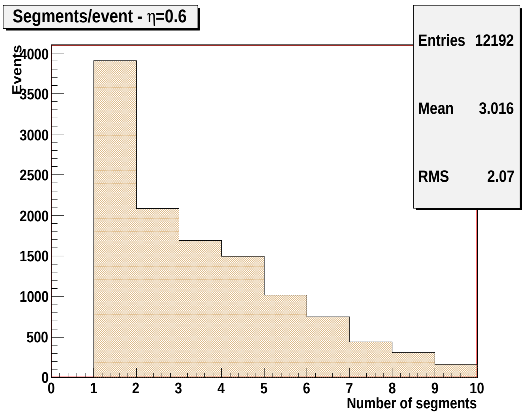

(k) Number of reconstructed track segments per event. Positron run at $\eta = 0.6$

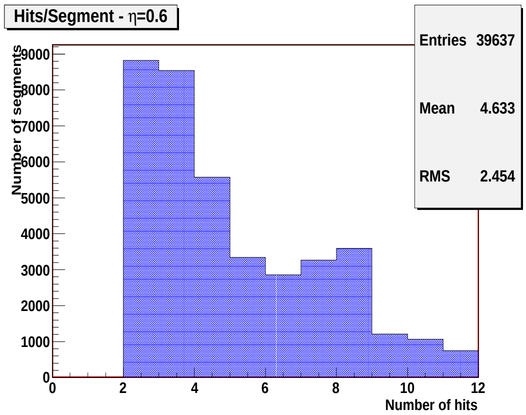

(l) Number of hits on segment. Positron run at $\eta = 0.6$

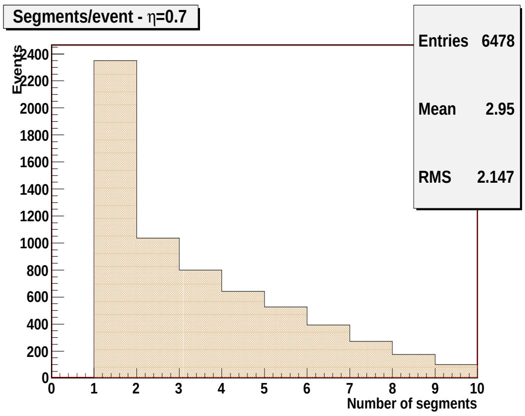

(m) Number of reconstructed track segments per event. Positron run at $\eta = 0.7$

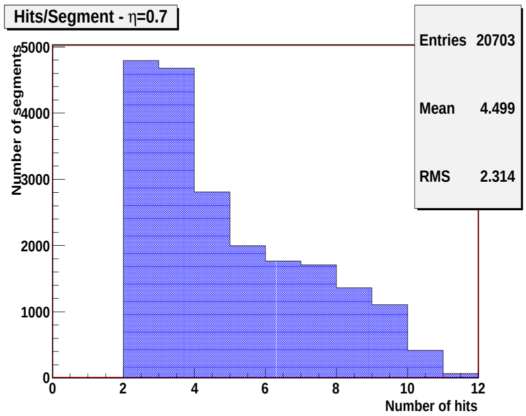

(n) Number of hits on segment. Positron run at $\eta = 0.7$

Figure 4.8: **Number of reconstructed track segments and hits on segment in BIS. Positron runs.**

The number of hits per event in the BIS chamber is given in the histograms of Fig.4.9 and indeed large tails above 10 hits per event can be observed. Note that these histograms are not extracted from all the tubes of the BIS chamber, the number of which is: 8 layers $\times$ 36 tubes $=$ 288 tubes. Different incident angles of the beam on the BIS chamber means that the calorimeter platform performs shifts along the z-axis (apart from the rotation around y-axis), which in turn implies that the beam is not impinging on the BIS chamber at the centre in each run but it is possible that the beam hits the side areas of the chamber. As a result BIS is not uniformly illuminated, therefore, to obtain a reliable calculation of number of hits per event, only hits of the most illuminated tube plus 2 tubes on each side of the latter, in each layer are taken into account. The choice of 5 tubes in each layer is dictated by the beam profile of BIS (an example is given in Fig.4.5(c)) where 5 tubes correspond to the RMS of the profile.

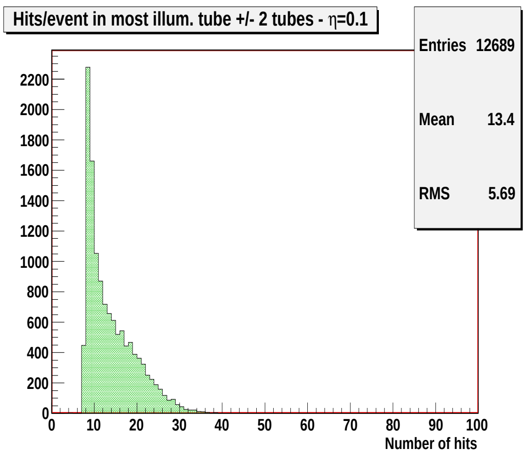

(a) Positron run at $\eta = 0.1$

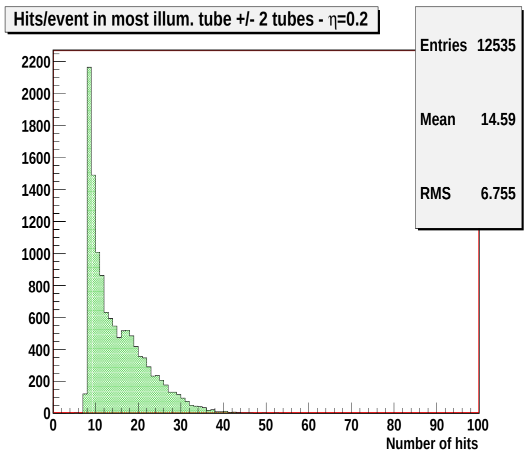

(b) Positron run at $\eta = 0.2$

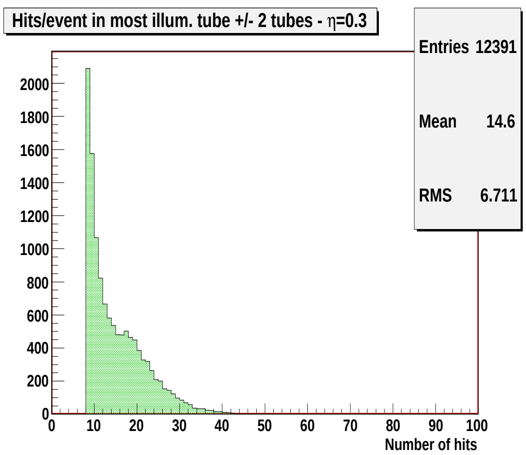

(c) Positron run at $\eta = 0.3$

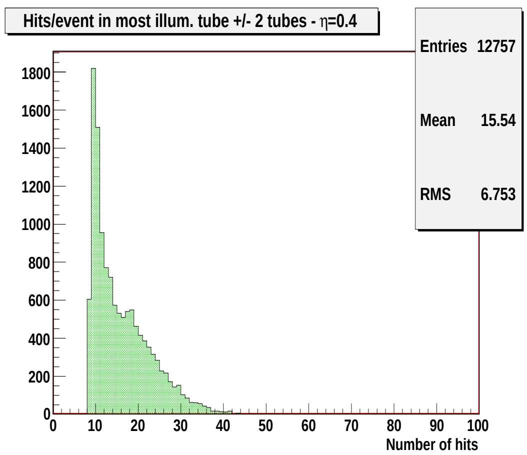

(d) Positron run at $\eta = 0.4$

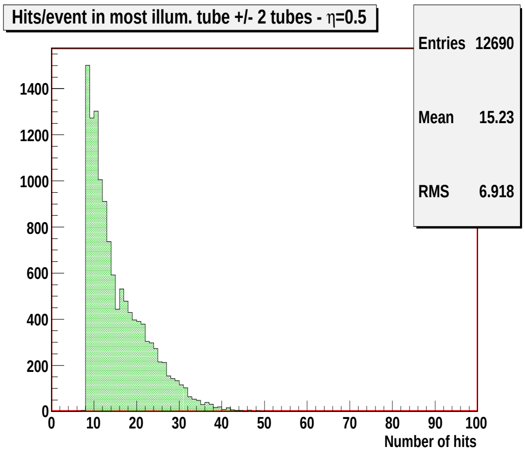

(e) Positron run at $\eta = 0.5$

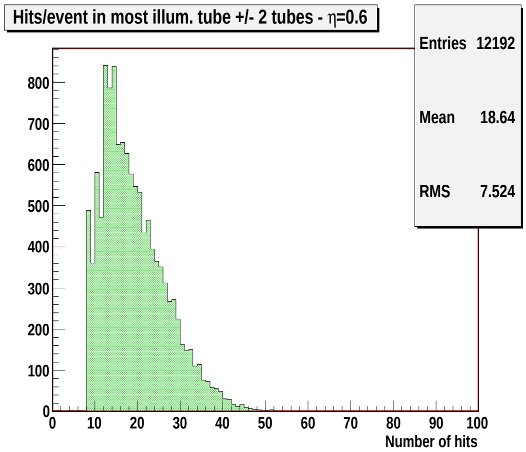

(f) Positron run at $\eta = 0.6$

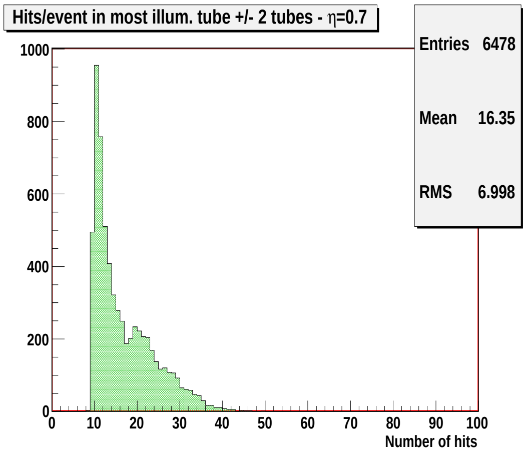

(g) Positron run at $\eta = 0.7$

Figure 4.9: **Number of hits per event in the BIS chamber for positron runs from the hits in the most illuminated tube ± 2 tubes.**

The above considerations are also justified by the corresponding plots in the muon run case, shown in Fig.4.10. Here most of the times only one segment is reconstructed in each event, and the hits on track has a clear peak at 8 which is expected from an 8-layer chamber like BIS. The energy loss due to bremsstrahlung scales as $1/m^2$ therefore muons are significantly less probable to radiate in the material of the ID or the muon chamber itself than the positrons. A comparison between Fig.4.10(c) where the tail in number of hits per event is small and the distributions of Fig.4.9 of the positron runs, manifests the cleaner hit environment in which track segments are reconstructed in the muon run.

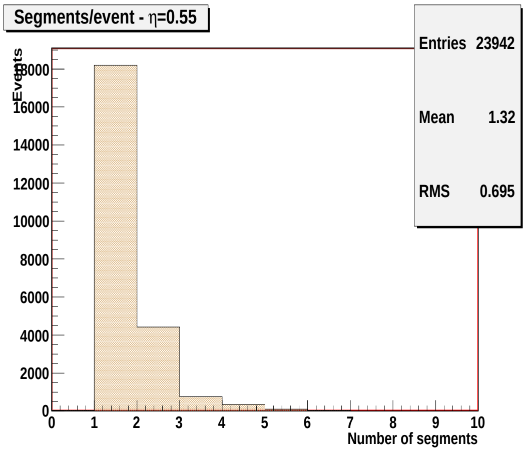

(a) Number of reconstructed track segments per event

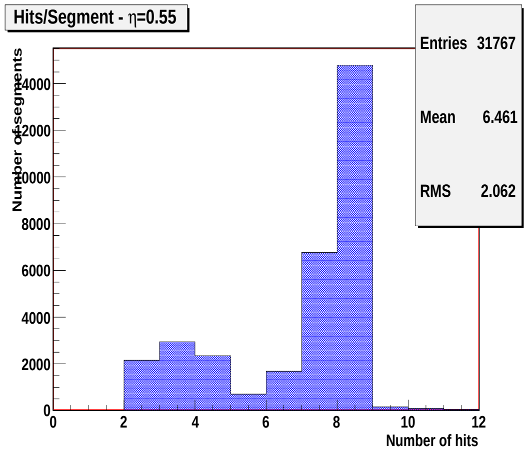

(b) Number of hits on segment.

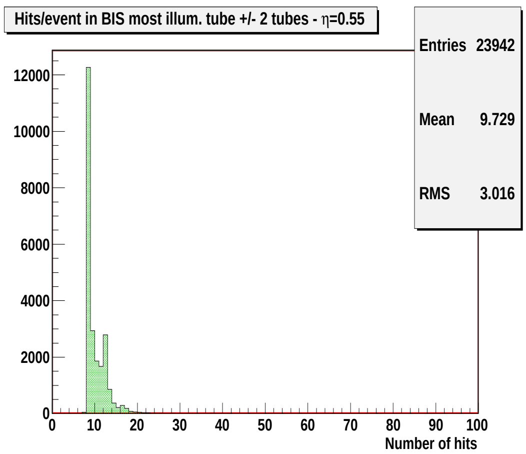

(c) Number of hits per event.

Figure 4.10: **Number of reconstructed track segments 4.10(a), hits on segment 4.10(b) and hits in most illuminated tube ± 2 tubes in BIS 4.10(c). Muon run at $\eta = 0.55$.**

Variables of Fig.4.8 are not representative of the chamber's performance. A quantitative estimate of the latter can be obtained by studying the residuals of the track segment hits, that is the difference between the fitted track and the actual drift radius. For this reason and also since the aim is to correlate the track reconstructed on the BIS chamber with the cluster barycentre of the LArEM calorimeter, it is necessary to select segments that fulfill some qualitative criteria, hereafter called "good segments". On the basis of the number of hits per track segment in BIS, a good segment is selected requiring at least 7 hits. In case there are more than one segments with more than 7 hits, the segment with the maximum number of hits is retained. The distribution of residuals for the positron and muon runs are given in Fig.4.11. Fig.4.11(h) corresponds to the muon run.

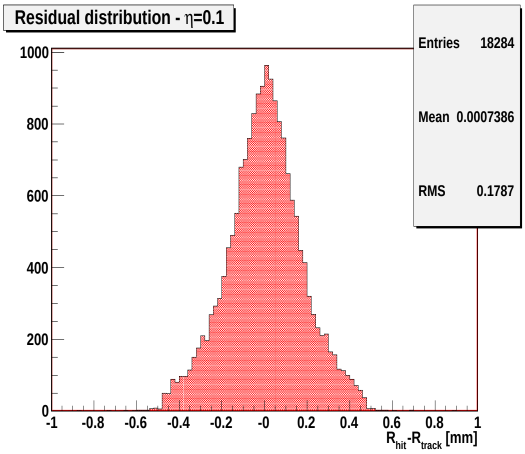

(a) Positron run, $\eta = 0.1$

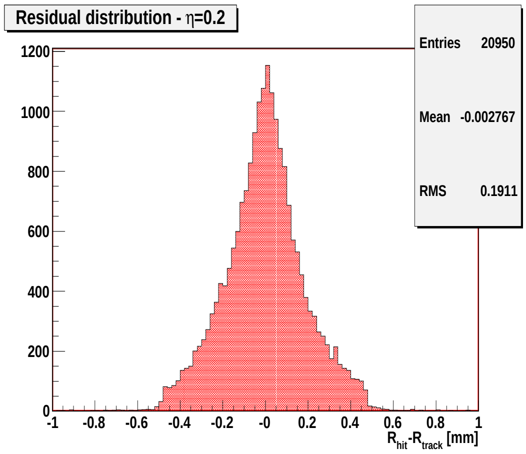

(b) Positron run, $\eta = 0.2$

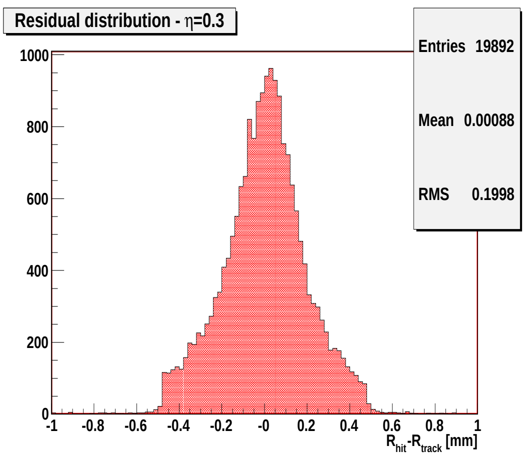

(c) Positron run, $\eta = 0.3$

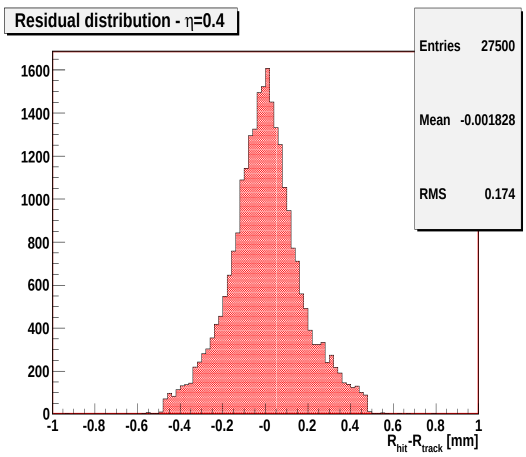

(d) Positron run, $\eta = 0.4$

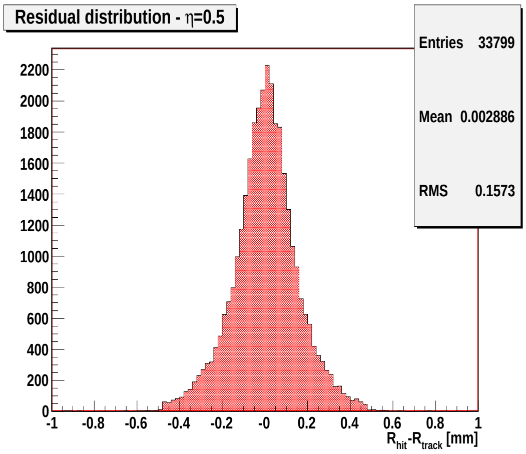

(e) Positron run, $\eta = 0.5$

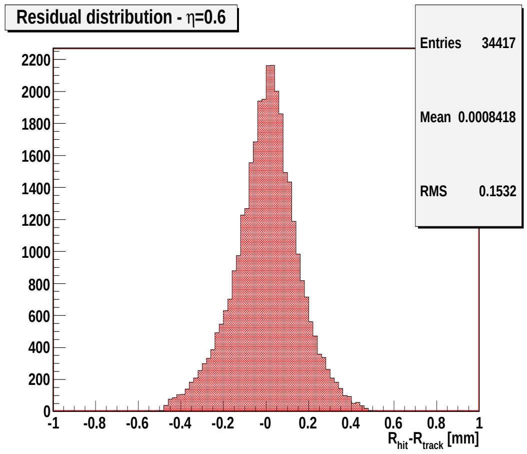

(f) Positron run, $\eta = 0.6$

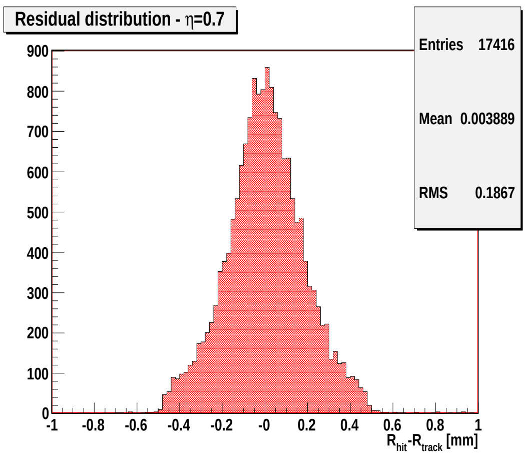

(g) Positron run, $\eta = 0.7$

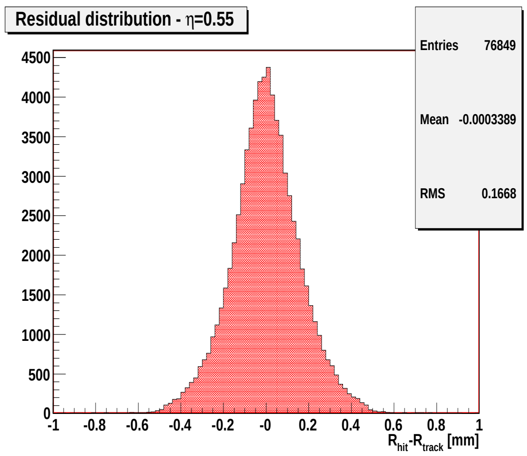

(h) Muon run, $\eta = 0.55$

Figure 4.11: **Residual distributions of reconstructed track segments.**

Fig.4.12 summarizes the values of RMS from each residual distribution of the positron runs. For positrons, the RMS values vary between 200 μm and 150 μm while in the muon case the value is 166.8 μm. These values are compatible with the expectations in the H8 CTB. No η dependence of the residuals is observed while the relative large residuals and their variation with η point to non fully calibrated $r - t$ relations, which is in fact the case since the calibration constants were provided by a different chamber and no temperature corrections were applied.

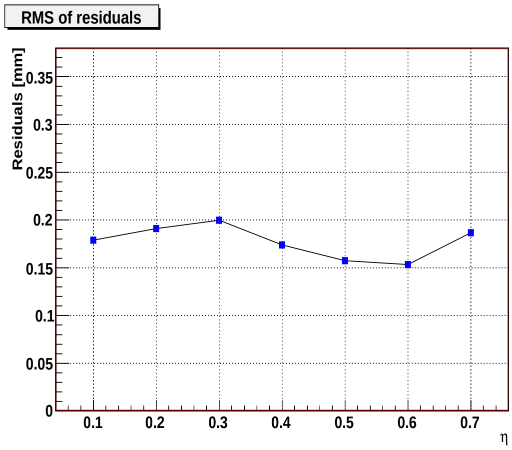

Figure 4.12: **RMS of residual distributions in positron runs**

4.2.4 Correlation between the track segment in BIS and the LArEM calorimeter cluster barycentre

The selected track segments through the procedure described in the previous section, provide the z-coordinate of the track on the BIS chamber. This coordinate is compared to the η of the cluster barycentre which is reconstructed in the front sampling of the LArEM calorimeter. The clustering algorithm used to obtain the cluster barycenter η is called "sliding window" algorithm and is based on summing cells within a fixed-size rectangular window. More information about the sliding window clustering algorithm can be found in reference [37].

The correlation plot obtained from all positron runs is given in Fig.4.13 and indeed correlation is evident between the precision coordinate of the track segment on BIS and the η of the cluster barycentre, although the correspondence is not exactly 1:1. In order to translate a coordinate parallel to the cryostat into an η and ϕ position one needs to know until where to extrapolate the track inside the calorimeter. In order to compare with an η measured by the calorimeter, one has to extrapolate until the depth where the barycenter of the shower lies. This is different for each shower, and only accessible by simulation. However, simulation provides only an average shower depth, which has precision of 1 cm approximately. Therefore the precision of the correlation is limited and this is why 1:1 correspondence is not

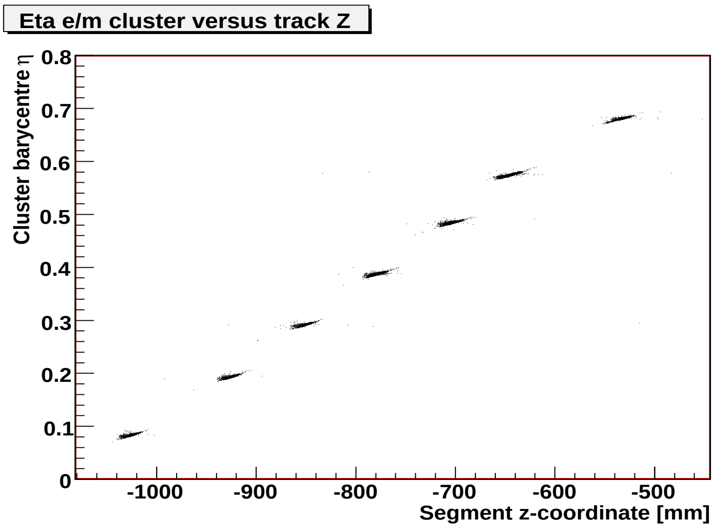

Figure 4.13: **Correlation between the z-coordinate of the track segment in BIS and the cluster calorimeter barycentre at the front sampling of the LArEM** - All positron runs are superimposed on the plot

observed in this case [38]. A zoom-in view at $\eta = 0.4$ is given as an example in Fig.4.14

4.3 Summary

During the summer of 2004 in a special experimental setup at the H8 CTB, a BIS muon chamber was tested. The chamber was installed in front of the calorimeter in order to study the performance of the chamber with both muon and positron beams. In the case of positron beams the reconstruction was even more challenging because of the nature of positrons and the processes that lead to multiple hits per event in the muon chamber.

The analysis included the selection of reconstructed track segments according to calorimetric criteria in order to select events with positrons or muons and reconstruction criteria in order to select "good" track segments. It has been proven that the pattern recognition algorithm performs well and track segment reconstruction is possible even in the presence of multiple hits, at steep beam incident angles and different illumination conditions.

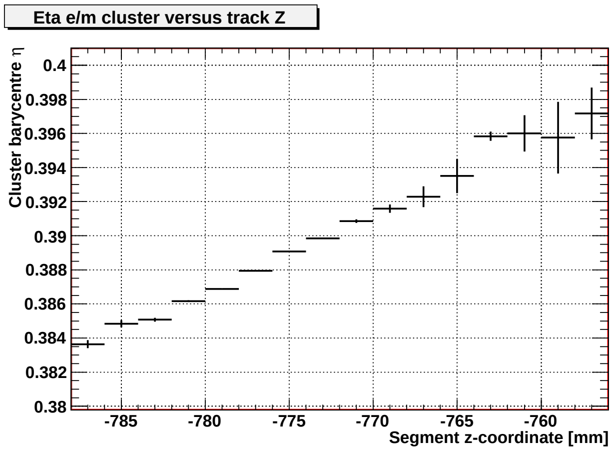

Figure 4.14: **Zoom-in view of the cluster barycentre η versus the z-coordinate of the reconstructed track segment on BIS, from positron run at $\eta = 0.4$**

The RMS of the residual distribution of the reconstructed track segments in BIS was found to vary between 200 μm and 150 μm which is compatible with the expectations at the H8 CTB, given that this result is obtained without using a dedicated $r - t$ relation extracted from the particular muon chamber.

Tracks reconstructed in the BIS chamber were shown to be correlated to the calorimeter cluster barycentre η for various beam incident angles.

5

Catastrophic muon energy loss in testbeam data

5.1 Muon energy loss in ATLAS

In the ATLAS Muon Spectrometer, muons will be measured in a rather clean environment. This is because, as already discussed in chapter 3, the calorimetric system which precedes the MS, applies a material barrier of the order of approximately 100 X_0, resulting in the absorption of any other charged particle except muons before the MS. However, muons will also lose energy in the material before the MS, therefore the resolution of their momentum measurement depends on the processes that take place inside the calorimetric volume. These effects should be taken into account by muon reconstruction algorithms in order for the latter to reach the required momentum resolution. In ATLAS muon reconstruction algorithms, this is achieved by sophisticated techniques which use either direct measurements in the calorimeters or alternatively, parametrizations of the energy loss in order to correct for the amount of energy lost downstream the MS. In references [39, 40, 41] these issues are discussed in great detail.

In this chapter a study of 350 GeV muons which deposit a large fraction of their energy, the so-called catastrophic energy loss, in the ATLAS calorimeters, is presented. Analysis is performed on 2004 data taken at the H8 Combined Testbeam setup described in chapter 4, and includes combination of muon tracks reconstructed in the MS system with their corresponding energy deposition signature in the calorimeters. This is done in order to reject pion contamination of the muon beam in CTB and study the catastrophic muon energy losses by directly measuring the response of the calorimeter.

In the next section a brief theoretical introduction is given on the physics of the muon energy loss in matter and focus is given on the mechanisms that contribute and increase the probability of a muon to lose a large fraction of its energy while interacting with matter. In sections 5.3 and 5.4 the analysis procedure on identifying muons with catastrophic energy loss and results from CTB and MC data are presented respectively.

5.2 Passage of muons through matter

The physical processes that describe how muons lose energy when they interact with matter are represented in a ”condensed” form by the solid curve in Fig.5.1, which corresponds to the mean rate of energy loss of muons on copper versus the muon momentum or $\beta\gamma$ term, where $\beta = \nu/c$ and $\gamma = 1/\sqrt{1-\beta^2}$ is the Lorentz factor. There are four distinct regions visible on this plot, classified according to the momentum of the muon. The first two regions up to $\beta\gamma \sim 0.5$, which correspond to muons with momentum of <10 MeV, are called Lindhard-Schaff and Anderson-Ziegler regions. In the Lindhard-Schaff region the energy loss is proportional to β, as described by the Lindhard theory [42, 43], but this behaviour is not sufficient to explain the Anderson-Ziegler region where only the name-part approximations exist [44] to give a fair description of the energy loss mechanisms.

The other two regions which extent from $\beta\gamma \sim 0.5$ onwards, are of great interest for ATLAS because muon momenta are expected to lie within these boundaries. Up to roughly $\beta\gamma = 800$, which is the region called Bethe-Bloch , muons lose energy proportionally to $1/\beta^2$ mainly due to ionization and atomic excitation. Finally, the region above Bethe-Bloch is called Radiative because radiative mechanisms start contributing to the energy loss and they are responsible for the rise of the curve in Fig.5.1. In the following sections the various energy loss mechanisms are described in more detail.

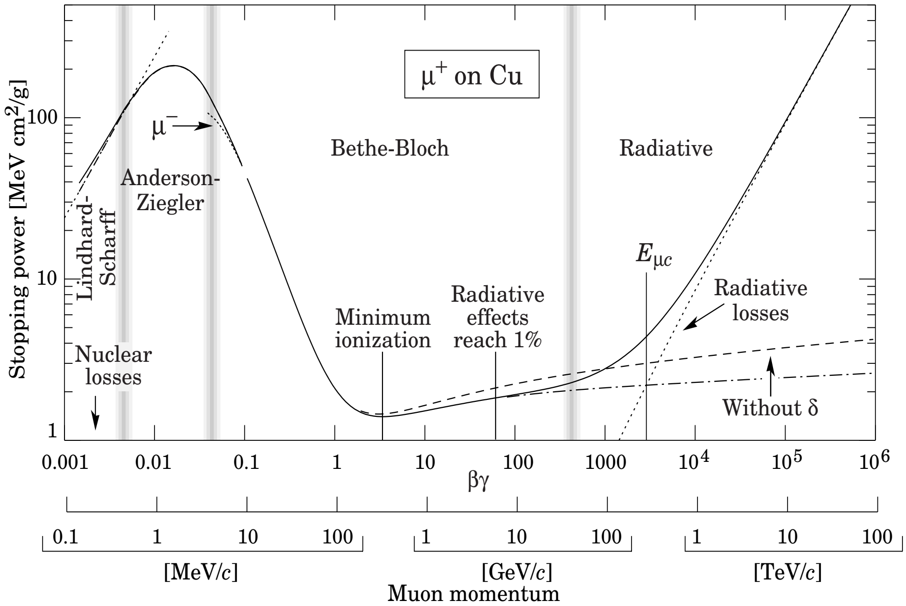

Figure 5.1: **Mean energy loss rate for muons on copper as a function of** $\beta\gamma = p/Mc$ - The momentum extents over nine orders of magnitude. Boundaries of different regions discussed in the text are represented by the vertical bands.

5.2.1 Ionization

Ionization is the dominant energy loss mechanism for muons of moderate momentum of the order of few MeV up to $\sim 80\ GeV$. The energy loss in this region is described by the famous Bethe-Block formula given in equation 5.1. The term K is a constant equal to $4\pi N_A r_e^2 m_e c^2$, where N_A is Avogadro's number, r_e is the classical radius of the electron and m_e is the electron mass. I is the mean excitation energy of the absorber which in turn depends on the Z of the material. The kinetic energy that can be transfered from the muon to the absorber material in a single collision is represented by T_{max} in the Bethe-Bloch equation and its definition is given by equation 5.2 [10].

$$-\frac{dE}{dx} = Kz^2 \frac{Z}{A}\frac{1}{\beta^2}\left[\frac{1}{2}ln\frac{2m_e c^2\beta^2\gamma^2 T_{max}}{I^2} - \beta^2 - \frac{\delta(\beta\gamma)}{2} - \frac{C}{Z}\right] \tag{5.1}$$

$$T_{max} = \frac{2m_e c^2\beta^2\gamma^2}{1 + 2\gamma m_e/M + (m_e/M)^2} \tag{5.2}$$

As it can be seen in equation 5.1, the mean energy loss per unit length depends through the I, Z and A terms on the material that the muon passes from and the velocity of the muon. In the low β region the mean energy loss rate decreases quickly with increasing β, reaching a minimum rate at $\beta\gamma \sim 3$. A muon (and any other charged particle) with energy that corresponds to the point at which dE/dx reaches a minimum is called Minimum Ionising Particle (MIP). For low energies equation 5.1 is necessary to include the term C/Z, the so-called shell correction, to correctly account for the contribution of the atomic binding energies which is of the order of 1% at $\beta\gamma = 0.3$. The correction is only significant in low energies because as energy grows C/Z decreases rapidly.

On the other hand, as β increases further from the MIP point, the energy loss starts increasing slowly, and the dependence becomes logarithmic $ln\beta\gamma$. In this case, the Bethe-Bloch formula has to include also the correction term $\delta(\beta\gamma)/2$ which is called density effect correction. The density effect occurs when the particle's energy increases and its electric field flattens and extends resulting in distant collisions contribution to rise logarithmically as $ln\beta\gamma$ [10].

5.2.2 Energy loss at high energies

As it is indicated in Fig.5.1, when the energy of the muon increases significantly, radiative processes start contributing to the energy loss and eventually dominate over ionization losses. In Fig.5.1 this is represented by the rapid increase of the mean energy loss rate with increasing momentum of the muon in the radiative region.

There are three basic radiative energy loss mechanisms the cross-sections of which can be found in reference [45]:

- Bremsstrahlung
- Pair production
- Photonuclear interactions

The average rate of muon energy loss is written as:

$$-\frac{dE}{dx} = a(E) + b(E)E \tag{5.3}$$

where the $a(E)$ term comes in from the ionization contribution and the sum of the radiative processes is given by $b(E)$. In principle, the cross-sections of these processes are small, they have rather hard spectra and induce large fluctuations in the energy loss. The contribution of each of the above mechanisms to the $b(E)$ term is shown in Fig.5.2 as a function of the energy of muon. The behaviour of $b(E)$ in the high energy regime can be approximated as constant and since $a(E)$ has negligible contribution of the order of 10^{-3}, radiative mechanisms dominate at high energies.

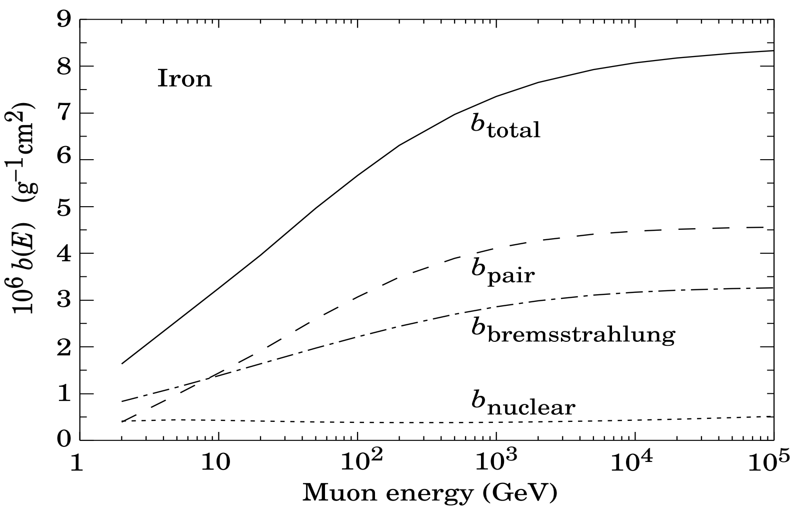

Figure 5.2: **Contribution to the term $b(E)$ from radiative energy loss mechanisms as a function of muon energy** - From reference [45].

If we define the fractional energy loss of a muon with initial energy E as $\nu \equiv E_{loss}/E$ then the cross-section for bremsstrahlung scales as ν^{-1} and the cross-section for pair production as ν^{-3} to ν^{-2} [10]. Photonuclear interactions are related to the process of inelastic scattering of muons from the nucleons or nucleus of the material. Their cross-section rises with muon energy and they contribute to the energy loss mainly when ν is very large. They have almost the same shape as the bremsstrahlung cross section at high ν, but they are about an order of magnitude lower. In Fig.5.3 the cross-sections of the energy loss mechanisms are shown as a function of ν, for muons of various momenta. Although pair production dominates the radiative contributions to the mean energy loss, bremsstrahlung dominates at high ν and since the cross-section of the latter scales as ν^{-1}, hard or "catastrophic" energy losses are therefore more probable in bremsstrahlung. In any case, when radiative processes start to play the leading role in the energy loss, ”catastrophic” loss is more likely to occur. The question which rises then is which is the threshold that one should start taking these effects into account. A convenient answer to this is given by introducing the critical energy.

5.2.3 The muon critical energy

A very useful quantity that can be indicative of the point where radiative mechanisms become important is the ”muon critical energy” E_μ^{crit}, which is defined as the point where ionization and radiative losses become equal. The muon critical energy can be calculated by solving $E_\mu^{crit} = a(E_\mu^{crit})/b(E_\mu^{crit})$. In Fig.5.1 this point is the intersection of the dotted and semi-dotted lines. The critical energy depends on the atomic number Z and this dependence is presented in Fig.5.4. The fact that the critical energy of muons is higher for gases than for solids and liquids is because of the smaller density-effect correction for gases [45].

Some typical values of the muon critical energy which are interesting for ATLAS and in particular for the calorimetric system are the ones for iron, lead and liquid argon. These values can be calculated from the tabulated data of reference [45]. In iron the muon critical energy is 347 GeV, in lead 141 GeV and in liquid argon 485 GeV. These values imply that radiative mechanisms of energy loss for muons become important at lower energies in the LArEM calorimeter than in the TileCal. Therefore, ”catastrophic” energy losses of high momentum muons should also be searched for in the LArEM and in the TileCal systems. In the next sections,these considerations are taken into account when ”catastrophic” energy losses of 350 GeV muons are studied in CTB data.

5.2.4 Fluctuations in muon energy loss

The number of energy loss interactions and the energy transfer of muons in each collision with the traversed material are both statistical processes which are determined by probability distributions. The number of collisions per unit length of material is determined by a Gaussian distribution whereas the energy lost by a muon crossing a path of thickness x has an energy distribution called energy straggling function.

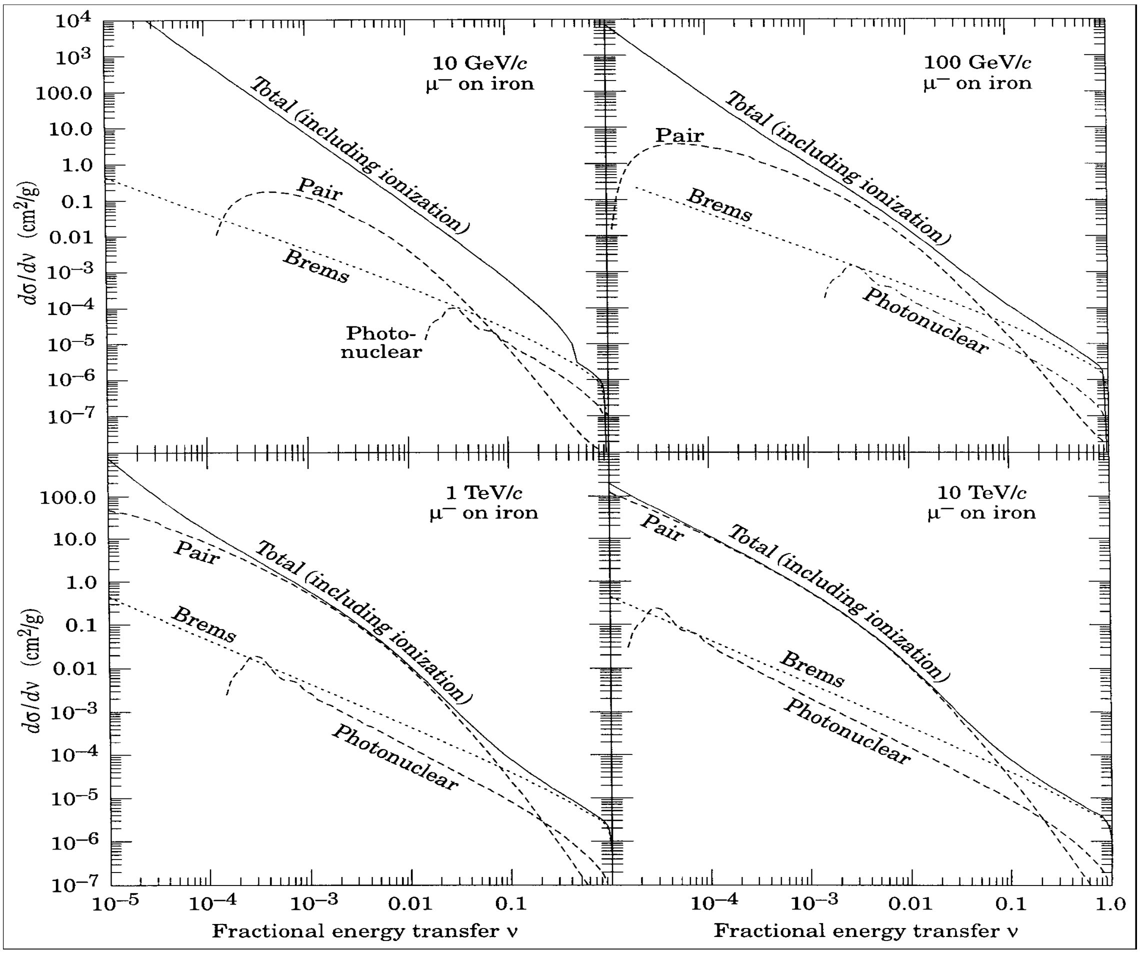

Figure 5.3: **Differential cross section of all energy loss mechanisms as a function of the fractional energy transfer for muons on iron** - From reference [45].

The probability function describing the distribution of energy loss in this case is called Landau distribution and its most probable value is given by equation 5.4.

$$\Delta_p = \xi \left[ln\frac{2mc^2\beta^2\gamma^2}{I} + ln\frac{\xi}{I} + j - \beta^2 - \delta(\beta\gamma) \right] \tag{5.4}$$

In the above equation $\xi = (K/2)(Z/A)(x/\beta^2)$ is the mean energy loss in MeV and $j = 0.2$. This is a distribution with a characteristic asymmetric long tail which extends up to high values of the energy loss and is caused in rather rare collisions where the energy transfer is high. While dE/dx is independent of the thickness x, Δ_p/x scales as $\alpha lnx+b$ [10]. The Landau distribution describes well the energy loss

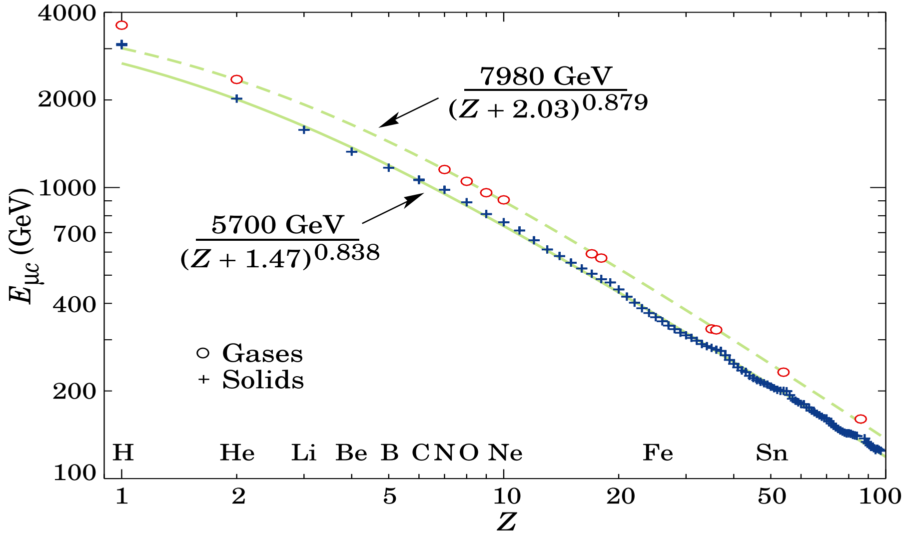

Figure 5.4: **Muon critical energy as a function of the atomic number Z in gases and solids** - From reference [10].

of a muon through materials of moderate thickness and also very thick absorbers [46], but in the latter case the distribution is less asymmetric. However this does not mean that it approaches a Gaussian. The shape of an example Landau distribution which has mean 3.5 and $\sigma = 1.0$ is given in Fig.5.5.

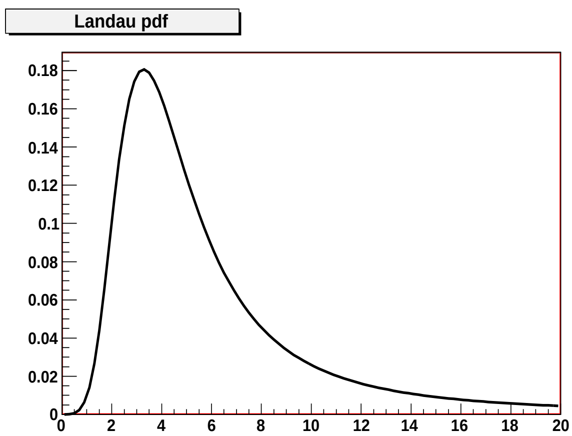

Figure 5.5: **Example of a Landau pdf** - The mean of the pdf is 3.5 and $\sigma = 1.0$.

5.3 Analysis

Identifying muons that have suffered catastrophic energy loss in the calorimeters in testbeam data exhibits one main difficulty. Muon beams at the CTB are not exactly 100% pure but there is also a fraction of pions contaminating them. Muons which pass through the calorimeters and deposit large amounts of energy in the calorimeter layers, hereafter called catastrophic muons, are possible to reproduce the behaviour of pions which also deposit all or most of their energy there. If the pions are stopped inside the calorimeter volume, then a requirement of a track reconstructed in the MS is enough to reject these events. However, there is a fraction of pions that will either leak through the calorimeter, the so-called punch-through pions, giving a track in the MS or they will decay to muons which will in turn produce a track in the MS. The aim of the analysis procedure is the appropriate combination of the reconstructed track in the MS and the energy deposition information in the calorimeters in order to classify events as non catastrophic muons, catastrophic muons and pions. This is explained in section 5.3.4. In sections 5.3.2 and 5.3.3 the selection of the tracks reconstructed in the MS stand and the measurement of the calorimeter response are respectively described.

5.3.1 Data samples

Listed below are the data samples used in the analysis. Both real and MC data include information from the calorimetric system and the muon chambers and will be hereafter referred to as 'combined runs'.

- **Real data** - 20,000 events of a combined run with muon beam of $E = 350$ GeV which is hitting the calorimeters at $\eta = 0.55$.
- **MC data** - 10,000 events of a combined run with muon beam of $E = 350$ GeV which is hitting the calorimeters at $\eta = 0.55$.

5.3.2 Muon track selection

Track pattern recognition in the Muon System is provided by Muonboy reconstruction package, properly configured to perform reconstruction in the particular testbeam geometry. Details on the performance of Muonboy package in the CTB setup can be found in reference [47].

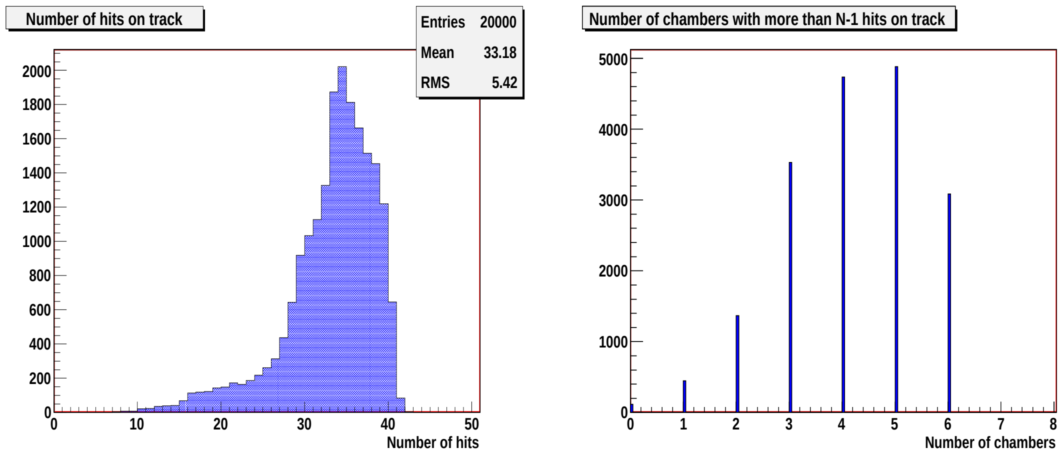

(a) Number of hits on track summing all the barrel and end-cap hits. There are 4 chambers with 6 layers and 2 chambers with 8 layers.

(b) Number of chambers with at least N-1 hits on track. The selected tracks here are required to have at least 12 hits.

Figure 5.6: **Number of hits on reconstructed track and number of chambers with at least N-1 hits** - Note that N is the number of layers.

In order to identify an event as muon it is important to select events with one track reconstructed in the MS which fulfills some quality criteria. A "good track" is defined as a track which has a minimum of 12 hits in the muon chambers and at least one barrel muon chamber is required to be involved. From the six muon stations that potentially have hits on the track, as described in section 4.1.2, BIL and EIL chambers have 8 layers of drift tubes and the rest of the chambers in the barrel, as well as in the end-cap stands, have 6 layers of tubes. This means that the total number of hits in the ideal case should be 40. The distribution of the total number of hits on track in the six MDT chambers is given in Fig.5.6(a). The peak in this plot is at 34 hits while the in majority of events the number of hits on track exceeds 20, which is compatible at least three MDT stations. With 12 hits per track there are at least two chambers involved in the reconstruction.

The request for two chambers with at least 12 hits on the track instead of three is because in the 2004 H8 setup, the beam at the BML stand was crossing the boundary point, along the z-axis, between the two chambers causing inefficiencies in the track reconstruction [47]. Therefore this requirement ensures that a track reconstructed only in the barrel MDTs will not be rejected because the muon is ”missing” the BML stand. For events with one good reconstructed track in the MS,

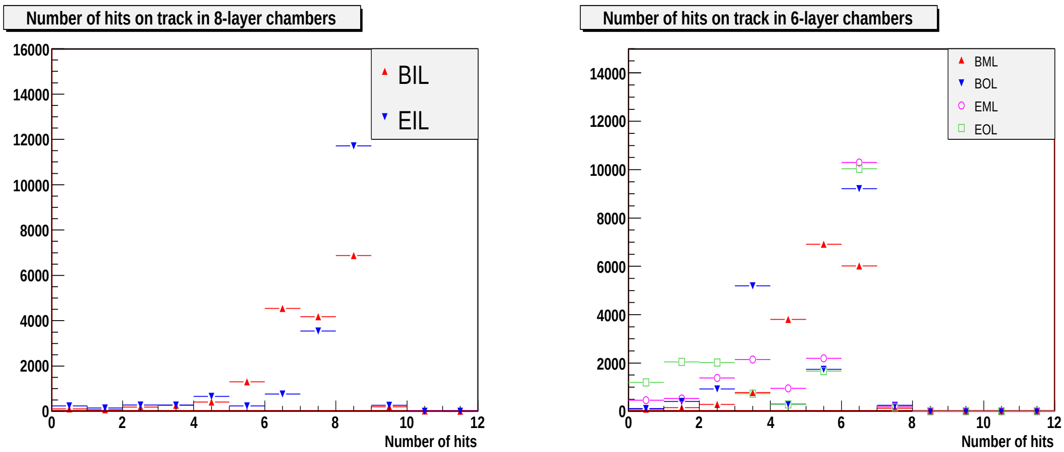

(a) Number of hits per track in 8-layer muon chambers

(b) Number of hits per track in 6-layer muon chambers

Figure 5.7: **Number of hits on track per muon chamber for tracks with at least 12 hits on track.**

the number of track hits in each chamber is given in Fig.5.7. The number of hits per good track for each chamber type is presented separately for the 8-layer 5.7(a) and 6-layer chambers 5.7(b).

In fact, the majority of the selected tracks with the 12 hit requirement have more than two chambers with N or N-1 number of hits, where N is the number of layers of the chamber. This is demonstrated in Fig.5.6(b), where it is evident that in most cases the number of chambers with at least N-1 hits is more than three.

5.3.3 Calorimeter response

LArEM Calorimeter

The LArEM calorimeter is longitudinally segmented in three samplings. A measurement of the muon signal in the LArEM calorimeter is difficult because the signal-to-noise ratio is small in the three compartments, therefore one has to eliminate as much as possible the noise contribution to the total measured energy by taking into account only cells illuminated by the beam. For this reason, a special reconstruction algorithm needs to be deployed in the layers of the LArEM.

The energy deposits of muons in the middle LArEM sampling are usually contained in one cell but some times charge can be shared by two adjacent cells. Since the calorimeter platform position was fixed with respect to the beam at $\eta = 0.55$, the cell with the maximum energy in the middle LArEM layer is found in the track path within the range $\eta = 0.55 \pm 0.05$. From the neighbour cells in η and ϕ only those that have energy above 100 MeV are taken into account. The noise per cell in the middle layer is around 20-30 MeV [9] therefore the 100 MeV cut is used to minimize the noise contribution to the measured energy.

The contribution of the cells in the front compartment to the total noise is large, therefore only one cell behind the most illuminated one in the middle sampling layer is added to the total from this layer. Finally, from the back compartment where the granularity is bigger, only the cell illuminated by the beam is taken into account.

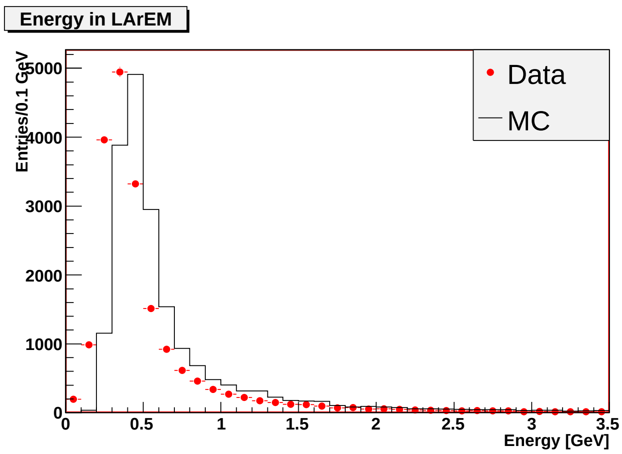

Figure 5.8: **Total energy deposited in the LArEM in CTB and MC data.**

In Fig.5.8 the distribution of the total energy deposited in the LArEM calorimeter is illustrated for both CTB and MC data. As it is clearly seen in the figure, there is a systematic shift of the MC distribution with respect to the one from CTB data. This effect has also been observed and is discussed in reference [48]. It rises from the fact that in the simulation with the Geant version v4.7 which is used here, the energy reconstruction in the LArEM used an incorrect sampling fraction, leading to an overestimation of the measured energy by 10% in all LArEM cells. Therefore for the current study values of the MC are scaled down by 10%.

Tile Calorimeter

The Tile calorimeter is longitudinally segmented in three compartments, A, BC and D. Given the narrow beam profile, the fixed position of the calorimeter platform with respect to the beam and the large granularity of the tile compartments, $\Delta\eta \times \Delta\phi = 0.1 \times 0.1$ in A and BC and 0.2×0.1 in D , there was only one cell illuminated by the beam in each compartment, hence the energy is obtained from the cell illuminated by the beam from each TileCal compartment. Again, in order to suppress noise contributions to the measured energy, only if the cell energy exceeds 50 MeV is taken into account. The expected noise per cell in the TileCal is roughly 15 MeV.

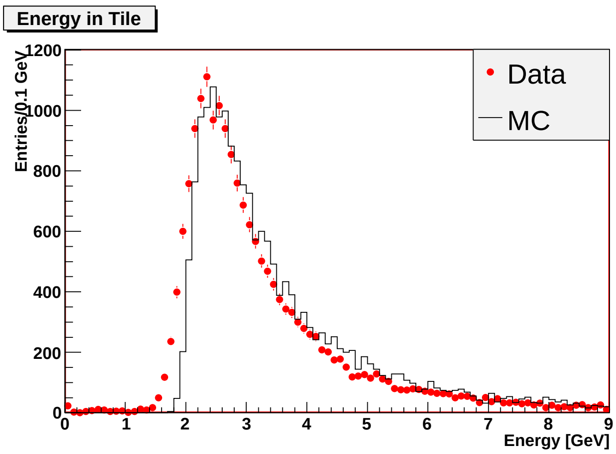

Figure 5.9: **Total energy deposited in the TileCal in CTB and MC data.**

In Fig.5.9 the distribution of the total energy deposited in the TileCal is illustrated for both CTB and MC data. As it is clearly seen in the figure the shapes of the distributions between data and simulation are different and there is also a small shift of the MC distribution with respect to the one from CTB data. As in the case of LArEM, this discrepancy in the measured muon signal between data and MC simulation has been observed also in reference [48] where it has been shown to be of the order of $\sim 5\%$ for 350 GeV muons. The difference is attributed to the fact that the simulation did not include light attenuation effects in the tiles. Therefore, in what follows the MC energy distributions in the TileCal are artificially scaled down by $\sim 5\%$ in order to match the CTB data.

5.3.4 Event classification

The energy measured in the LArEM and TileCal calorimeters, as described in the previous section, is shown in the correlation plot of Fig.5.10(a) for CTB data and in Fig.5.10(b) for MC data. There is an event population that exhibits significant energy deposit in both calorimetric systems in the CTB data plot. This behaviour is compatible with pions of similar momentum to muons, which indeed contaminate the beam in the CTB. The pion contamination is also justified by Fig.5.10(b) where the pure muon MC simulation sample is shown. The population of events with big energy deposition in both calorimetric systems is absent here as expected. It can be also noted that significant fraction of the energy of the muon can be deposited in the LArEM calorimeter as expected by the fact that the muon critical energy in the LArEM is less than in the TileCal, implying that radiative losses start contributing to the energy loss earlier in the LArEM.

Muons produce a track in the MS, therefore requesting a good track in the MS should have been enough to separate between pions and muons. However the possibility to have a pion penetrating through the $\sim 10\lambda$ of material of the ATLAS calorimeters and reach the MS, should be also taken into account especially since in the CTB runs analysed here, the dump between the calorimeters and the MS had been removed, which means that it is also possible that pion tracks can be reconstructed in the MS. In addition, some pions can decay to muons which will again produce a track in the MS.

Because of the above reasons, certain criteria have to be fulfilled in order to identify muons with catastrophic energy loss and classify events in two mutually exclusive categories; muons and pions. This is achieved exploiting the way muons and pions lose energy in the LArEM and in each one of the three TileCal compartments, complemented with the reconstruction or not of a track in the MS. The selection criteria are described in the following:

Muons

Two basic requirements need to be fulfilled so that an event is classified as a muon. First, one good track reconstructed in the MS should exist and secondly, the corresponding energy deposition in the calorimeter volume should be compatible with a MIP particle. The latter means that MIP energy depositions should exist in the

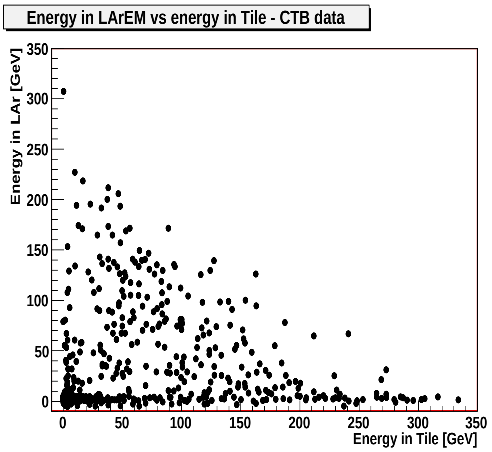

(a) Energy in LArEM versus energy in Tile calorimeters from CTB data

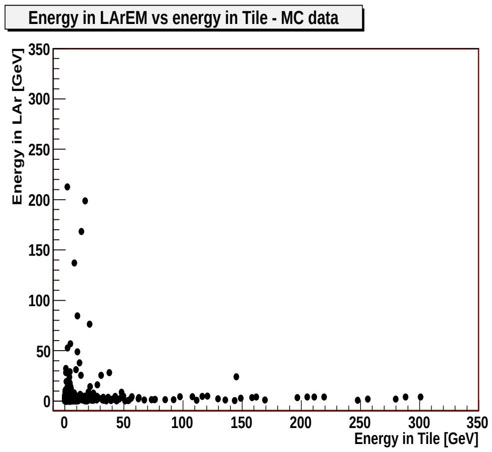

(b) Energy in LArEM versus energy in Tile calorimeters from MC muon data

Figure 5.10: **Energy in LArEM versus energy in Tile calorimeters from CTB and MC data** - Red points correspond to CTB data while the solid curve to the Landau fit.

LArEM and each of the three TileCal compartments. Since the material contribution of the LArEM ($\sim 25X_0$) is of the same order with one TileCal compartment, in the following the LArEM will be treated as one compartment. The MIP energy threshold values for all compartments are extracted from CTB data and the energy distributions in each of them are illustrated in Fig.5.11. The distributions are fitted with a Landau and the MIP energy threshold is calculated as $E_{MIP} \simeq MPV + 5\sigma_{landau}$ where MPV is the Most Probable Value of the Landau fit. The values obtained through this method are 0.6 GeV, 0.8 GeV, 2.2 GeV and 1 GeV for the LArEM, A, BC and D compartments respectively.

In addition, events can be also classified as muons if they are required to have a good reconstructed track in the MS and energy deposition greater than one MIP in only one calorimeter compartment. This category includes the catastrophic muon candidates.

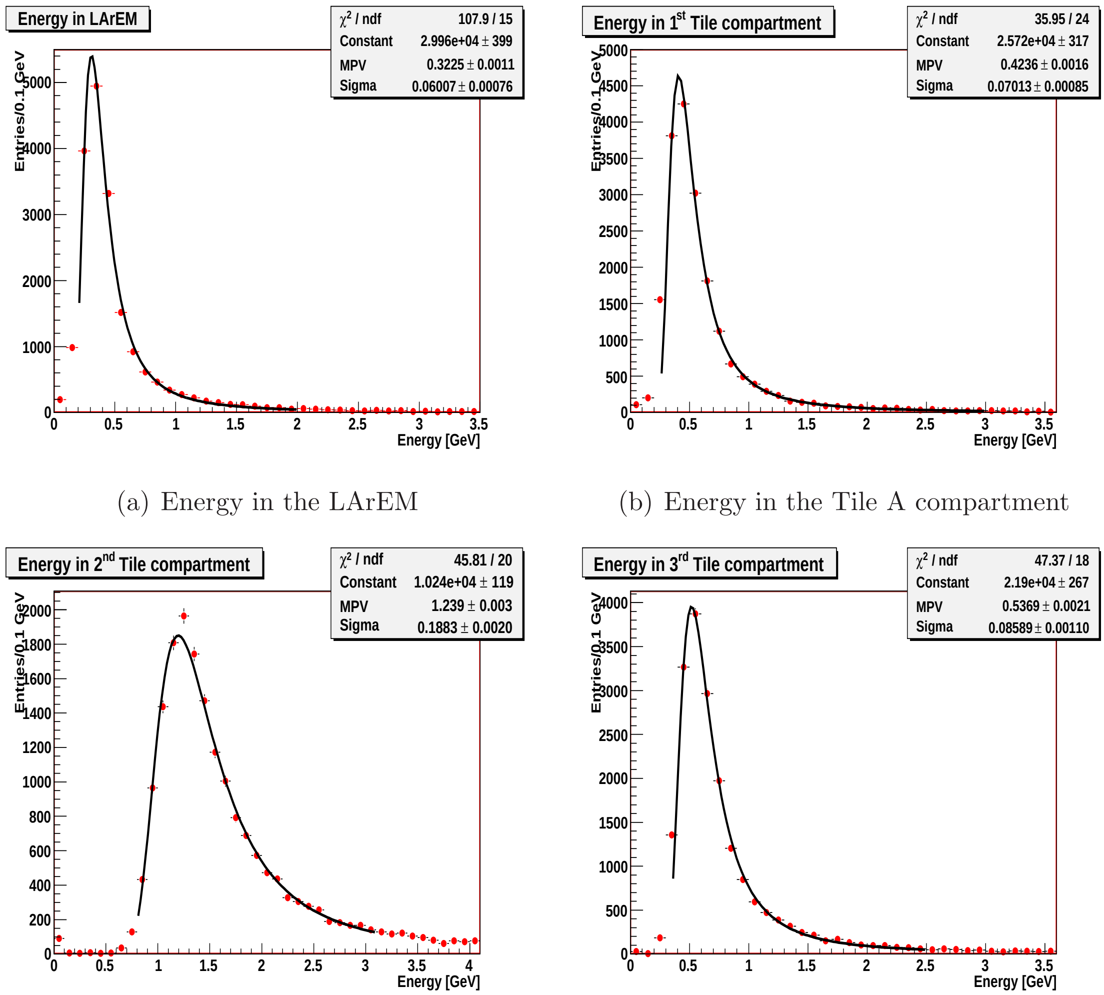

(a) Energy in the LArEM

(b) Energy in the Tile A compartment

(c) Energy in the Tile BC compartment

(d) Energy in the Tile D compartment

Figure 5.11: **Energy deposited in the calorimeter compartments before selection criteria.**

The requirement for more than one MIP deposition in only one compartment or MIP in all compartments, has good discriminating power between muons and pions because the latter are expected to shower throughout their path in the calorimeters, depositing energy well above the MIP zone in more than one compartments. This is justified by the plots of Fig.5.12(a), 5.12(b) and 5.12(c), 5.12(d) where the correlation between the energy deposited in the LArEM and TileCal A compartment and between the TileCal A and BC compartments are shown for pions and muons from MC data. Note that the pion sample used here is of the same energy as muons and impinge on the calorimeter at the same η point. As it can be seen, pions deposit a large amount of their energy in more that one compartment and their shower starts already in the LArEM calorimeter.

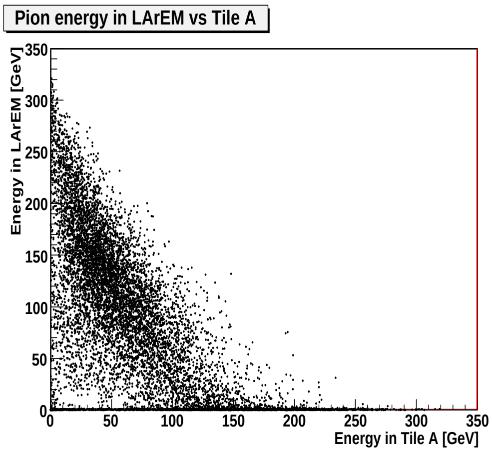

(a) Energy deposited by pions in the LArEM versus the energy deposited in Tile A compartment

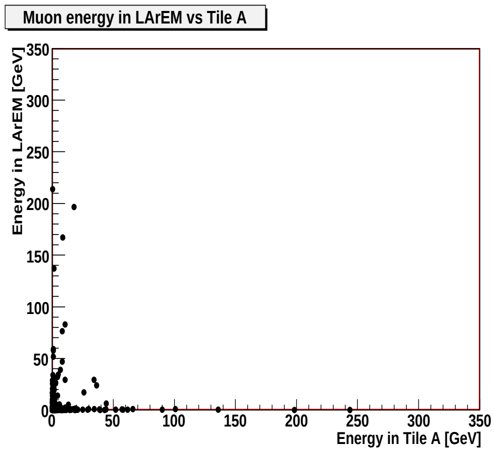

(b) Energy deposited by muons in the LArEM versus the energy deposited in Tile A compartment

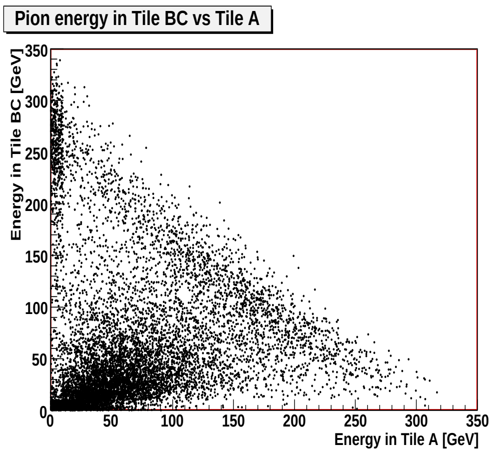

(c) Energy deposited by pions in the Tile BC versus the energy deposited in Tile A compartment

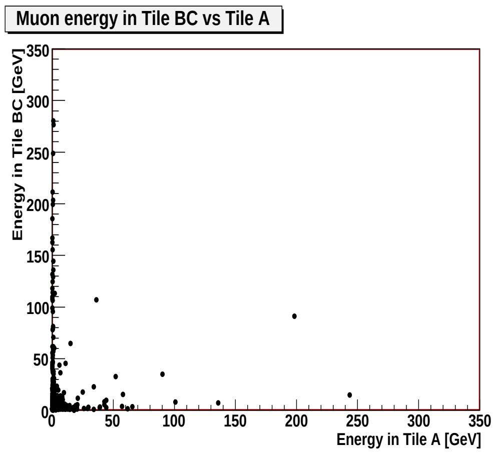

(d) Energy deposited by muons in the Tile BC versus the energy deposited in Tile A compartment

Figure 5.12: **Correlation plots of the energy deposited in the calorimeter compartments for pions and muons in MC simulation event samples.**

On the other hand muon showers are very localized around the muon track and are contained in only one calorimeter compartment. This is also seen in the figures

Event	MS track	E_{lar} - E^{A}_{tile} - E^{BC}_{tile} - E^{D}_{tile}	CTB %	MC %
Muons	Yes	<MIP in all or >MIP in one	77.0 ± 0.9	77.2 ± 1.2
Pions	Yes	>MIP in at least first 3	2.5 ± 0.2	1.6 ± 0.2
Not passing cuts			20.5	21.2

Table 5.1: **Summary of the selection criteria for tagging events as muons or pions.**

where no correlation between the deposited energy in two consecutive compartments is observed. Therefore, events with energy deposition above one MIP in only one compartment are classified as muons and are therefore candidates for catastrophic energy loss.

Pions

Events that have a good reconstructed track in the MS and energy deposited more than one MIP in at least the first three calorimeter compartments, are classified as pions. This category consists of both pions reaching the MS and muons coming from the decay of pions.

The selection criteria described above and the fraction of events in each event category after the selection is applied, are all summarized in Table 5.1. The bottom row of the table corresponds to events that do not fulfill the selection criteria and therefore cannot be identified either as muons or as pions. They are classified as events not passing the cuts and indicate the selection criteria inefficiency. This fraction of events is of the order of $\sim 20\%$ for CTB and MC data.

Finally, the fraction of events classified as pions, which in the MC case is 1.6%, indicates the misidentification probability because of the MIP definition. In the case of CTB data, there is a contribution to this fraction (2.5%) which indeed corresponds to pion contamination in the beam, in addition to the misidentification probability (1.6%).

5.4 Results

The corresponding plot to Fig.5.10(a), after the classification of the events based on the selection criteria, is given in Fig.5.13. The blue points, which represent pions, lie indeed in the area where significant energy deposition is seen in both calorimeters compatible with pion behaviour. The red points represent muons and lie in the sides of the plot. It should be noted that apart from the muons that are obviously catastrophic in the TileCal, there is also a number of muons that lose large amounts of energy in the LArEM calorimeter.

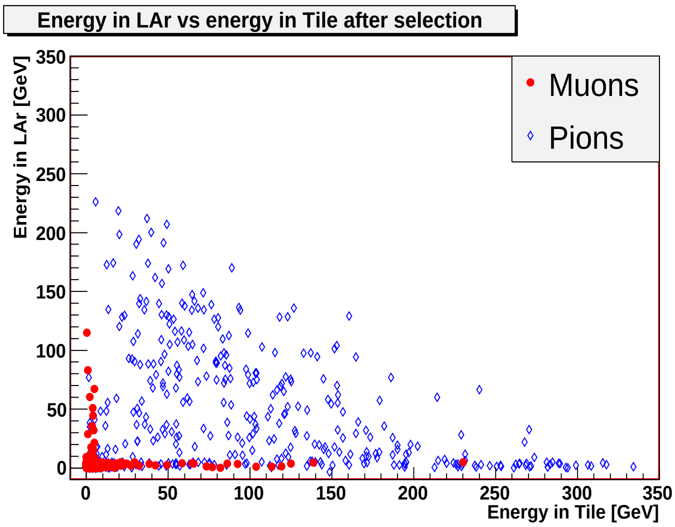

Figure 5.13: **Energy in the LArEM versus energy in the TileCal for events passing the selection criteria** - Events are classified as muons or pions based on the selection criteria described in the text.

The total energy distribution for the events classified as muons, either MIP muons or muons with catastrophic energy loss, is shown in Fig.5.14. CTB data are compared to data from simulation and the distributions are normalized to the same number of events. There is no indication of pion contamination in the sample which would have been visible at higher energies. The agreement is good in the low energies and within errors in the higher energies where statistical fluctuations are bigger.

The fraction of events or probability for 350 GeV muons to lose a large amount of their energy in the calorimeters is shown in Fig.5.15. The vertical axis gives the fraction of events with a total energy loss greater than a threshold value of the horizontal axis. The calculation is done for both CTB and MC data over a wide range of threshold values and good agreement with MC simulation expectations is

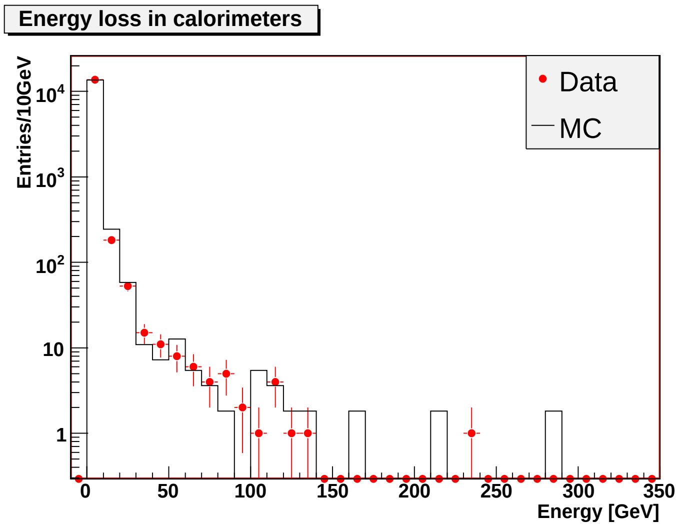

Figure 5.14: **Total energy deposited in the calorimeters of selected muons, in CTB and MC data.** - Distributions are normalized to the same number of events.

observed. Results are summarized in Table 5.2. Note that the event fraction in both CTB and MC data are referred to the total number of reconstructed muons and they do not contain the events which do not pass the cuts (see Table 5.1).

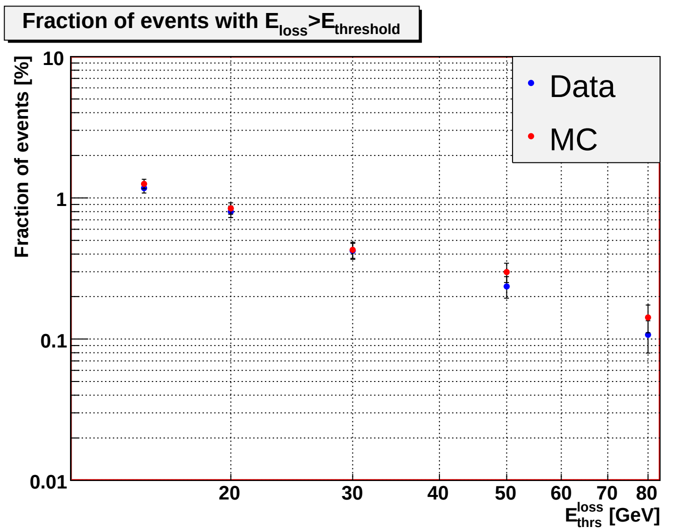

Figure 5.15: **Probability for catastrophic muon energy loss in the calorimeters versus the energy threshold, for CTB and MC data** - Errors shown here are statistical only.

$E_{threshold}$ [GeV]	Event fraction [%] - CTB	Event fraction [%] - MC
15	1.17 ± 0.09	1.26 ± 0.13
20	0.80 ± 0.08	0.84 ± 0.10
30	0.42 ± 0.06	0.43 ± 0.07
50	0.24 ± 0.04	0.30 ± 0.06
80	0.11 ± 0.03	0.14 ± 0.04

Table 5.2: **Fraction of events with $E_{loss} > E_{threshold}$ for CTB and MC data.**

5.5 Summary

In a 350 GeV muon beam at H8, using the information of the Muon System (barrel and end-cap) to reconstruct the track and the energy deposited in LArEM and TileCal, muons were identified and the ones with catastrophic energy losses were selected. The requirements on the reconstructed track quality and the criteria for the energy deposited in the LArEM and the TileCal compartments, assured a "pion-free" muon sample. The muon energy loss distribution in LArEM and TileCal of 350 GeV muons was compared to Monte Carlo simulation and found to be in good agreement.

Events of 350 GeV muons with catastrophic energy loss were identified exploiting the way muons lose energy in the calorimeter compartments. The fraction of muons exhibiting a total energy loss above 15, 20, 30, 50 and 80 GeV in the calorimeters was computed and results were found to be consistent with expectations from MC simulation.

6

Muon energy deposition and isolation measurement in the calorimeters

The direct measurement of the calorimeter response when a muon traverses the calorimetric volume is an integral part of muon reconstruction, the ultimate goal of which is the refit of the muon track with calorimeter information as well. In addition, the measurement of the energy deposited in the calorimeters by the muon itself and by other particles which might exist around its trajectory, enriches the information of the final muon object, providing the possibility to exploit the additional piece of information in offline physics analysis. To this end, an accurate method of energy deposition measurement in the calorimeters is developed under the software package name `TrackInCaloTools` [49], which is part of the official ATLAS software. Under the ATHENA framework scope, `TrackInCaloTools` is a tool that can be used by reconstruction algorithms many times in each event, as already mentioned in section 3.3.

Measuring the response of the calorimeters, when a muon penetrates the CS, is imperative for reasons discussed in the next section 6.1. The principle of the method is described in detail in section 6.2, while results from the application of the method on single muon events of various momenta and muons from $t\bar{t} \to 4\ell + X$ events are presented in section 6.3.

6.1 The importance of the muon energy loss measurement

The passage of muons from the calorimeters and the measurement of the calorimeter response addresses important issues that rise during reconstruction. The muon momentum, measured by the MS, is necessary to be complemented by the energy loss in the calorimeters, in order for the correct momentum information to be assigned to the final reconstructed muon object. On the one hand, the energy lost by muons in the calorimeters can be estimated by parametrizations but, on the other hand, this is not always sufficient to account accurately for the energy loss, especially in the case of muons with catastrophic energy loss because as seen in the previous chapter, there is not one formula to account for all energy loss mechanisms. This is the reason why reconstruction algorithms include techniques that try to determine for each muon candidate, which is the suitable information regarding the energy loss, the energy loss given by the parametrization or the one given by the measurement.

A measurement of the response of the calorimeters, when a muon traverses their material, also provides valuable information on the isolation of the muon candidate. Muons do not always reach the calorimeters alone, but are often accompanied by more particles that deposit energy in the area around the muon trajectory and interfere with the energy loss measurement of the muon itself. For example, a muon can emerge within a jet of hadrons created from quark decays but it can as well be isolated in cases like the leptonic decays of Z or W bosons. It is therefore essential to define isolation criteria for the candidate muons and correctly define their energy loss. Isolation is a corner-stone property of particles that can be exploited in physics analysis as a discriminant feature between different physics processes. An example will be given in chapter 7, where isolation is one of the variables used in the analysis of $ZZ \rightarrow 4\ell$ to reject background processes that exhibit non-isolated leptons in the final state.

Finally, the energy deposition measurement in the calorimeters is the base of muon tagging algorithms that use only calorimetric criteria to determine the "flavour" of the candidate. An example was already presented in chapter 5 where the energy measurement in the LArEM and the TileCal was used to separate muons from pions in the H8 testbeam setup. In ATLAS, muon tagging is attained using the LArEM calorimeter, the TileCal or both. Related algorithms already exist and their principle and performance is presented in reference [41].

6.2 Measurement principle

The most commonly used method for measuring the isolation and energy loss of muons in the calorimeters is based on the formation of the so-called calorimeter tower assuming that the trajectory of the muon is straight. The calorimeter tower is a collection of cells that lie within the boundaries of a cone with radius $\Delta R = \sqrt{\Delta\eta^2 + \Delta\phi^2}$ opened around the muon trajectory. However, the muon trajectory is not exactly straight but is subject to deviations from the straight line approximation because of multiple scattering from the detector material and also effects due to the magnetic field.

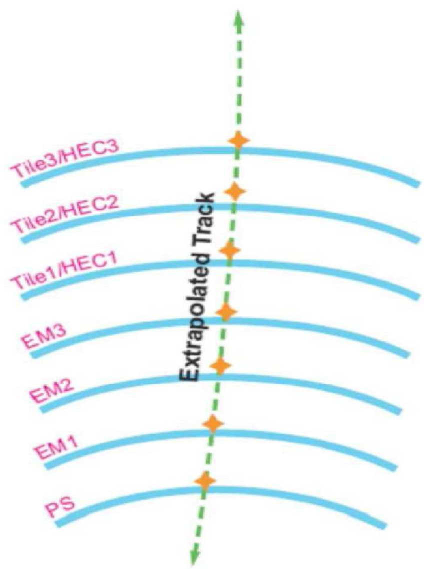

Figure 6.1: **Illustration of the track update method** - Information on the track is obtained at each layer of the calorimeter. The orange points represent the centres of the cones which open in order to form the local cell tower.

Within this context, the principle of `TrackInCaloTools` resides in the update of the track position information at each calorimeter layer taking into account these effects. The new position information in η and ϕ is then used as the centre of the cone which now opens at each calorimeter layer forming a kind of local cell tower. Fig.6.1 illustrates schematically this concept.

There are two basic pieces of information that `TrackInCaloTools` package provides. The first one is the energy or transverse energy deposited in a cone around the muon track in each or all the calorimeter layers. The second one is the calorimeter cell collection that exists inside a cone, again around the muon track. Both these outputs are passed to another tool (`MuonIsolationTool`) which uses them as input to provide the calorimeter muon isolation transverse energy and the cell cluster that is written to AOD and accompanies the muon object at this level.

Apart from the above functionality though, one can use `TrackInCaloTools` inside any algorithm or tool that needs information on the energy deposited in the calorimeters around a reconstructed track. The inputs, algorithmic flow and outputs of the method are described in the following.

6.2.1 Inputs, outputs and algorithmic flow

There are two basic and several optional inputs that `TrackInCaloTools` needs in order to perform an energy measurement. These comprise of:

- a track reconstructed either in the ID or the MS represented in software terms by an object of the `Trk::TrackParameters` or `Trk::Track` class.

- the cone radius ΔR that will be opened around the track to collect the energy from the cells that lie within the formed tower. There is also the possibility that not only one cone size is passed as input but instead, a list of cone sizes can be given. In that case the output corresponds to each cone size.

The outputs one can retrieve from `TrackInCaloTools` are:

- The energy or transverse energy deposited in the cone on each calorimeter layer, or in each calorimeter technology (LArEM, TileCal, HEC) or in the calorimeter in total.

- The cells that are contained in the cone-tower at the same layer(s).

- The collection of cells on track. This cell collection consists only from the ones that the track went through which means that one cell per calorimeter layer is collected.

The general concept of the program flow can be summarized in the following steps:

1. A track and the ΔR of the cone are given as input. The η coordinate of the track is retrieved from the corresponding `TrackParameters` set. Based on this and the pseudo-rapidity coverage of the first calorimeter layer, it is decided the region on the calorimeter, barrel or end-cap, to be used as the destination surface of the track extrapolation.

2. Extrapolation of the track is provided by the standard ATLAS `Extrapolator` tool. Effects due to multiple scattering and bending from the magnetic field are handled internally by the `Extrapolator` package. Details about the implementation of the track extrapolation facility in the ATLAS software can be found in reference [50]. The result of the extrapolation process is another set of `TrackParameters` which is now given on the target calorimeter layer.

3. From the new calorimeter layer the extrapolation is repeated towards the next calorimeter layer using the latest `TrackParameters` set. In this way, a collection of track impact points is formed.

4. The impact points on the calorimeter are passed to the method that performs the measurement and using the coordinates η and ϕ of the track on each calorimeter layer, a cone is opened around the track with radius ΔR. Note that in case an extrapolation has failed on one layer because, for example, the track is pointing in the crack regions of the calorimeter, the η and ϕ set of the last successful extrapolation is used as the cone opening point.

5. After cells are selected with the geometrical criteria described in the previous step, a second selection step is taken to suppress the noise contribution to the measured energy. The RMS of the noise of each cell, provided by `CaloNoiseTool` [51], is retrieved and the cell is retained if:

$$E_{cell} > N \times RMS_{noise} \tag{6.1}$$

The total energy deposition is then given by the sum of the energy of the selected cells. Note that N is a value which can be defined through job options and by default is set to 3.4.

6. The cell collection that participates in the energy deposition measurement and which is finally written as a calorimeter cluster at the AOD stage, is also formed at this step. The only difference from the previous step is that since the motivation of having cells in the AOD is the possibility to redo isolation in offline physics analysis, the cells are selected here applying a less strict noise cut according to:

$$|E_{cell}| > N \times RMS_{noise} \tag{6.2}$$

where N here is by default set to 2.0 and can be defined through job options. The size of the cone from which the cell cluster is created, is subject to constrains on the AOD object size which should be kept below the MB order. Therefore, by default a medium size cone of $\Delta R = 0.45$ is chosen to collect the calorimeter cells in the official ATHENA release versions.

6.3 Energy measurement in physics events

6.3.1 Measurement with single muon events

In Fig.6.2 and 6.3, a comparison between the measured transverse energy from `TrackInCaloTools` and the true transverse energy loss is shown. The radius of the cone used for the measurement is 0.2 around the muon trajectory and single muon events of momentum 10, 50, 100, 300, 500 and 1000 GeV were used. The average transverse energy loss is shown as a function of η . In the same η bins the average true transverse energy lost between the interaction point and the entrance of the Muon Spectrometer is shown as this is obtained from the GEANT4 ATLAS full simulation. The noise correction used in the measurement of the energy loss is on the cell level, according to equation 6.1.

The discrepancy between the measured and true transverse energy loss can be attributed to the energy loss in the inert material between the beam pipe and the entrance of the muon spectrometer. Indeed adding the parametrized energy loss

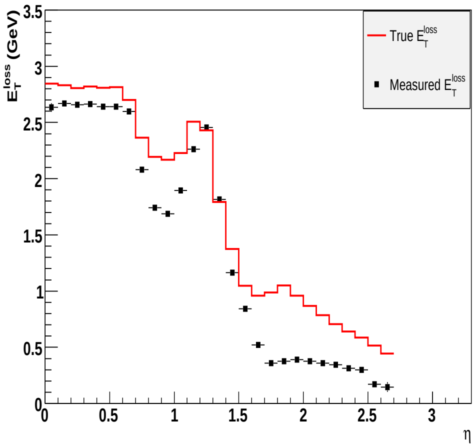

(a) Measured and true E_T loss as a function of η for muons of $P = 10$ GeV

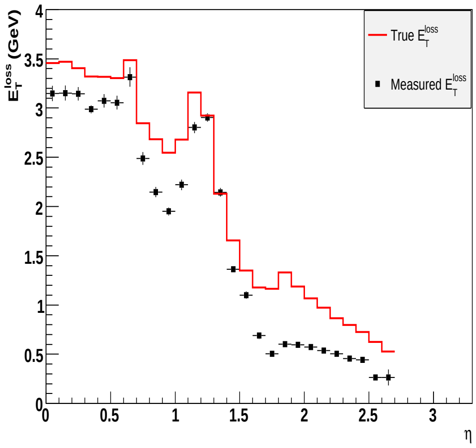

(b) Measured and true E_T loss as a function of η for muons of $P = 50$ GeV

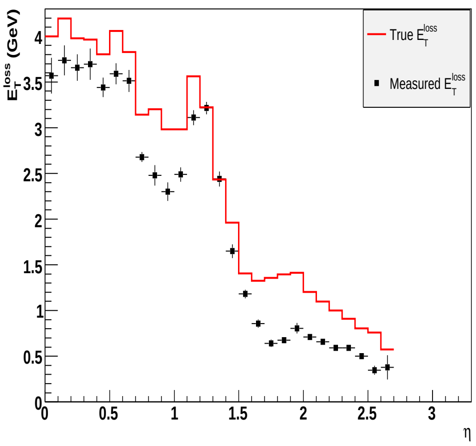

(c) Measured and true E_T loss as a function of η for muons of $P = 100$ GeV

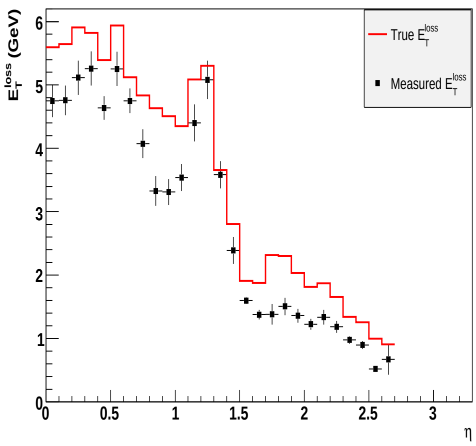

(d) Measured and true E_T loss as a function of η for muons of $P = 300$ GeV

Figure 6.2: **Measured transverse energy distributions compared to the true transverse energy loss, as a function of η for muons of momentum 10, 50, 100 and 300** GeV - The cone size used for the measurement of the energy loss is $\Delta R = 0.2$.

correction for the dead material has shown that it accounts for the discrepancy to very good agreement. The reason why this amount of energy loss is not included in the total transverse energy loss here or in `TrackInCaloTools`, is the fact that adding

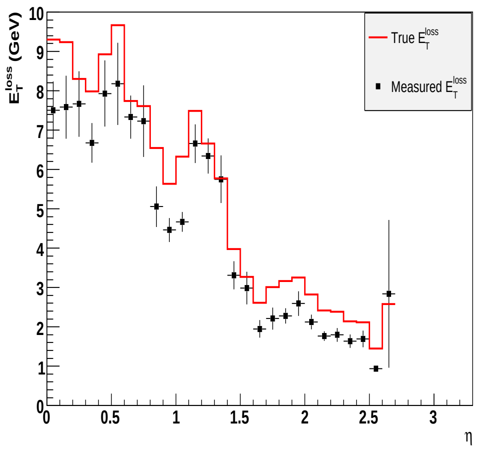

(a) Measured and true E_T loss as a function of η for muons of $P = 500\ GeV$

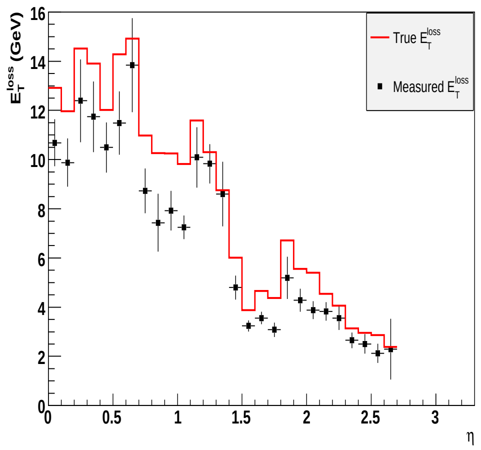

(b) Measured and true E_T loss as a function of η for muons of $P = 1000\ GeV$

Figure 6.3: **Measured E_T distributions compared to the true E_T loss, as a function of η for muons of momentum 500 and 1000** GeV - The cone size used is $\Delta R = 0.2$.

a muon energy loss parametrization term in the result, goes beyond the scope of a direct measurement in the calorimeters and the isolation concept.

The region around $|\eta| = 1$ corresponds to the crack in the TileCal and that is why the measurement is even lower than the energy loss in that region. The larger discrepancy that is seen in $|\eta| > 1.5$ is attributed to the high noise level of the HEC calorimeter. A typical value of the RMS of the noise distribution in the HEC on the cell level, is roughly 200 - 400 MeV [9].

6.3.2 Measurement with $t\bar{t} \rightarrow 4\ell + X$ events

A quantitative example of the facilities that `TrackInCaloTools` provides at the AOD, is illustrated well with $t\bar{t} \rightarrow 4\ell + X$ event sample. In this process both t-quarks decay to a W boson and a b-quark. The leptonic decays of the W which are forced here, give two high-p_T isolated leptons in the final state. The other two leptons that emerge from the decays of the b-quarks are softer and non-isolated.

Using the measurement method on muon tracks reconstructed by the STACO algorithm [2], the transverse energy in five cone sizes, opened around the muon track, are obtained. Muons are separated to the isolated ones from the W decays and to the non-isolated ones and the corresponding plots for the two categories of muons are shown in figures 6.4(a) and 6.4(b).

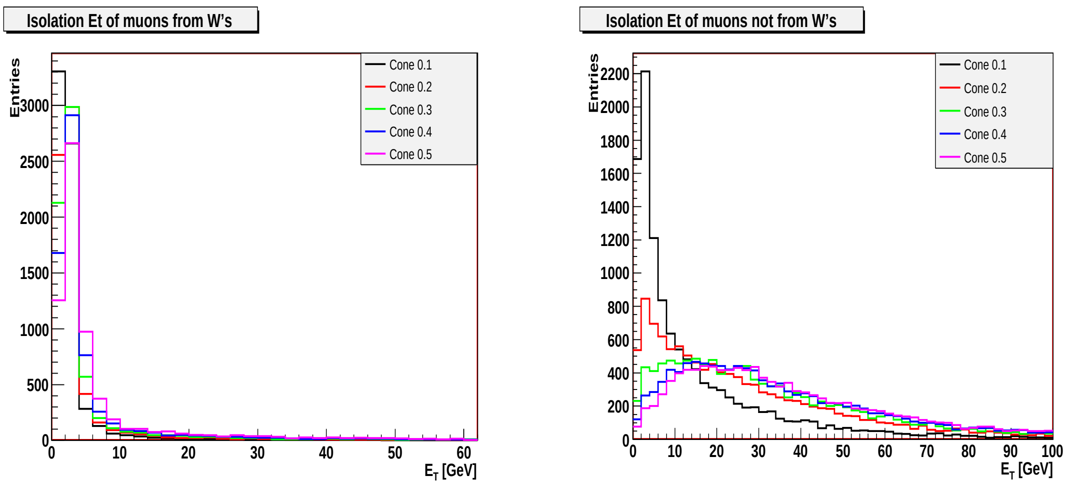

(a) Isolation E_T of muons coming from W boson decays, measured in 5 cone sizes

(b) Isolation E_T of muons not coming from W boson decays, measured in 5 cone sizes

Figure 6.4: **Isolation E_T of muons in $t\bar{t}$ events measured in 5 cone sizes** - Collected cells are required to have $E > 3.4\sigma_{noise}$.

In the case of muons from W decay the mean of the transverse energy collected rises almost linearly with the cone size and does not exceed 12 GeV even for the biggest cone. This is expected since the environment around the muon trajectory is rather clean and increasing the size of the cone, in principle adds only noise to the total measured E_T. However it should be stressed that it is possible that as the cone size increases, a jet near the muon track could interfere in the measurement.

In the non-isolated muons case, where it is anticipated that large amounts of energy will be deposited in the calorimeters because of the jet activity, the increase in the mean value of the transverse energy is indeed evident. The energy collected in the biggest cone has a mean value which is bigger by a factor of 4-5 with respect to the isolated muons case.

The mean values for the different cone sizes in each case are summarized in the plots of Fig.6.5. Note that the cells collected here are subject to equation 6.1.

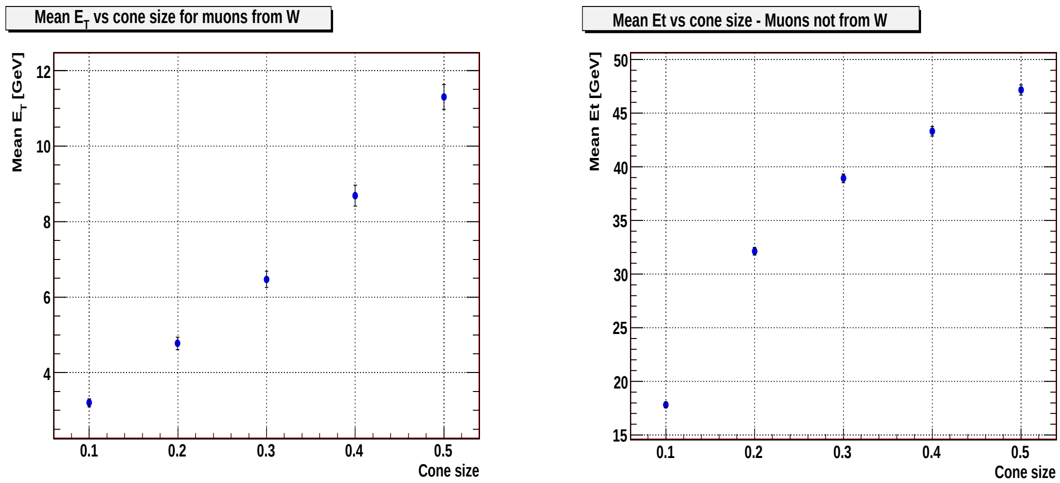

(a) Average isolation E_T of muons coming from W boson decays, measured in 5 cone sizes

(b) Average isolation E_T of muons coming from W boson decays, measured in 5 cone sizes

Figure 6.5: **Average isolation E_T of muons in $t\bar{t}$ events measured in 5 cone sizes for muons coming from the decays of $W's$ and any other muon.** - Noise suppression is performed on the cell level according to equation 6.1.

6.3.3 Number of cells involved in the E_T measurement

It is interesting to look at the number of cells that are involved in the measurement of the isolation E_T in both cases of muons. As it has been mentioned before, the information of the cells that are related to the isolation E_T measurement of the muons, as calculated in `TrackInCaloTools`, is present in the latest versions of ATHENA , at the AOD level. Therefore, this offers the possibility to exploit this additional piece of information for offline physics analysis.

In order to get a reliable estimate on the number of cells that become involved in a measurement, it is important to confine the measurement in such a pseudo-rapidity range that the cell granularity stays the same for each calorimeter layer. Because of this reason, here the following results are confined for muons reconstructed in the range $|\eta| \leq 0.8$.

In Fig. 6.6(a) the number of cells that participate in the E_T measurement around the muon trajectory is shown for different cone sizes. Both muon cases are superimposed here. Muons from W's and muons coming from any other process. Note that for each cone size, the core cone of $\Delta R = 0.1$ has been subtracted since this includes mainly the contribution of the cells that muons deposit their energy. The mean values from each distribution are gathered in Fig.6.6(b).

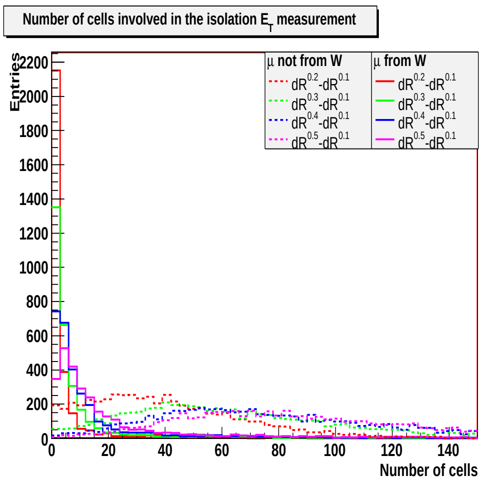

(a) Number of cells involved in the isolation E_T measurement of muons in $t\bar{t}$ events, measured in 4 cone sizes

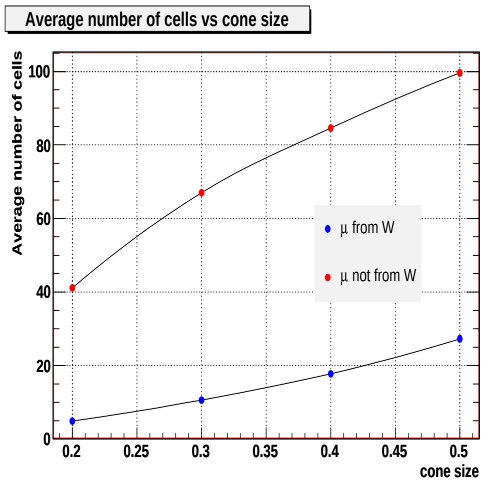

(b) Average number of cells involved in the isolation E_T measurement of muons in $t\bar{t}$ events, measured in 4 cone sizes

Figure 6.6: **Number of cells and average number of cells involved in the isolation E_T measurement of muons in $t\bar{t}$ events, measured in 4 cone sizes** - The η of all muon tracks is within $|\eta| \leq 0.8$. Noise suppression is performed on the cell level according to equation 6.1.

The number of cells involved in the measurement of the transverse energy loss, shows a remarkable behaviour in the case of isolated muons compared to the behaviour of the non isolated ones. The mean value of the largest cone size of the isolated muons is already below the mean value of the smalled cone size in the non-isolated case and well below the corresponding cone size. It is therefore possible to exploit this information in offline physics analysis as another discriminating variable between signal and background processes and a complementary criterion for the isolation of muons.

6.4 Summary

`TrackInCaloTools` is a software package developed in the context of this thesis which is integrated in the ATLAS software framework. It is used by `MuonIsolationTool` to provide the muon energy deposition measurements needed by the latter to create the isolation related variables. It also provides the calorimeter cells, that are associated with the measurement of the transverse energy in a cone around the muon track, which are thereafter used to produce a muon calorimeter cluster at the AOD data analysis level.

The energy lost by muons in the calorimeters has been proven that it is well estimated by the measurement method, performed in `TrackInCaloTools`, in the limit that corrections for the energy loss in the inert material are not taken into account. It also provides reliable estimation on the isolation E_T measurement and the calorimeter cells associated with this measurement for the muon candidate.

The isolation E_T in the calorimeters in various cones around the muon track has been measured in $t\bar{t}$ events for muons coming from the decay of W and for muons emerging from other processes. The mean measured E_T rises with the cone size for both isolated and non isolated muons but differ significantly in their values as expected.

The average number of cells, above noise threshold, associated with the isolation E_T measurement also varies with the cone size and striking difference has been observed between the average number of cells involved in the measurement of the isolation E_T of isolated and non isolated muons. The mean number of cells even in the biggest cone for the isolated muons, is smaller than the mean number of cells of the non-isolated in the smallest size cone. This indicates that the number of cells associated with the isolation E_T measurement could be used as a discriminating variable in physics analysis.

7

Studies of Z boson pair production with the ATLAS detector

7.1 Diboson production at the LHC

The production of vector boson pairs predicted by the electroweak interactions sector of the Standard Model is, in many respects, an issue of great importance for the physics searches at the LHC. Diboson production, exploiting the 14 TeV centre-of-mass energy available at the LHC, provides a unique probe to the accuracy of the Standard Model and the non-Abelian gauge symmetry at high energy. The self interactions of vector bosons are expected to the $O(10^{-4})$ within the SM theoretical framework and consequently, any deviation from the SM values would signal the existence of new physics which could manifest as anomalous couplings or new heavy particles that decay to vector boson pairs.

The importance of vector boson pair production is also realized as source of background to many interesting physics signals the prominent of which is the Higgs boson production. If the Higgs is heavy enough it will mainly decay through ZZ or WW pairs as it is illustrated in Fig.2.6. The ZZ channel in particular, which is studied in detail in the following sections, is very interesting because the process of $H \to ZZ$ with the subsequent decay of the two Z bosons to lepton pairs – the so-called "gold-plated channel" for Higgs discovery at the LHC – although it has a very clean signature with four isolated leptons in the final state, will suffer from the irreducible background which $q\bar{q} \to ZZ \to \ell\ell\ell\ell$ production constitutes. The latter is also a background to SUSY physics processes that include four leptons in the final state. It is therefore crucial to measure and control the ZZ channel already with the first data of LHC and as it will be shown in the next sections, this is indeed feasible with as little as 1 fb^{-1} of data.

7.2 Theoretical framework

The ZZ production mechanism is allowed in the SM and proceeds through the t and u-channel $q\bar{q}$ scattering shown in the Feynman diagrams of Fig.7.1(a) and Fig.7.1(b) respectively. The s-channel diagram in Fig.7.1(c) includes the neutral triple gauge coupling vertex which is not allowed at tree level in the SM. However, computation of the one-loop corrections introduces a contribution of this diagram at the $O(10^{-4})$ [52].

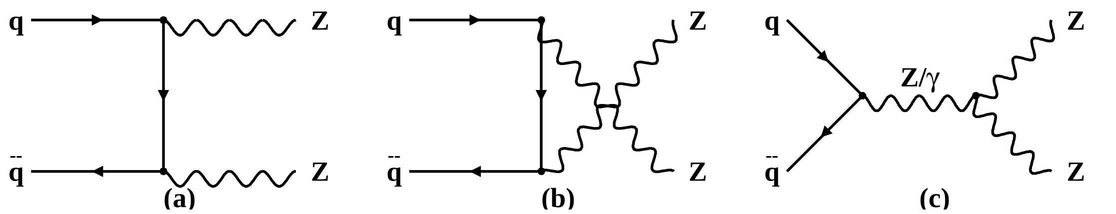

Figure 7.1: **Tree level Feynman diagrams of $q\bar{q} \rightarrow ZZ$ production** - Diagrams (a) and (b) show the t-channel and u-channel contribution, allowed in the Standard Model. Self interactions of Z bosons are included in (c) through the s-channel $q\bar{q}$ annihilation.

The cross-section at tree-level was calculated almost thirty years ago in reference [53] and includes all polarization states of the ZZ pair. The cross section in this reference is given as:

$$\frac{d\sigma}{dt} = \frac{2\pi\alpha^2}{s^2}\frac{g_V{}^{i4} + g_A{}^{i4} + 6g_V{}^{i2}g_A{}^{i2}}{e^4} \times \left[\frac{t}{u} + \frac{u}{t} + \frac{4M_Z^2 s}{ut} - M_Z^4\left(\frac{1}{t^2} + \frac{1}{u^2}\right)\right] \quad (7.1)$$

where s, t, u are the Mandelstam variables and i corresponds to quark flavour. Higher order QCD corrections were computed in references [54, 55, 56]. Later calculations of the $pp \rightarrow ZZ$ production cross section at $\sqrt{s} = 14\ TeV$ are performed in references

	σ_{LO} [pb]	σ_{NLO} [pb]	K_F
CTEQ5	12.9 (11.8)	17.2 (15.8)	1.33 (1.34)
MRST	12.2 (11.4)	16.3 (15.2)	1.34 (1.33)
CTEQ6	9.6	14.7	1.35

Table 7.1: **Summary of $pp \to ZZ$ production cross-section values for different PDFs** - Values not in parentheses are taken from Ref.[57], whereas values in parentheses from Ref.[58]. The NLO cross-section in the CTEQ6 PDF case is calculated by MC@NLO generator and the LO from PYTHIA requiring $70 < m(Z/\gamma^*) < 110\ GeV$ in both cases. Note that $K_F = 1.35$ is an average value since there is a dependence on the 4 lepton's invariant mass.

[57, 58]. The PDFs that are used in the references are the CTEQ5 and MRST and their results are summarized in Table 7.1.

In the bottom row of this table, the corresponding predictions for the CTEQ6 PDF [59] are of interest because this PDF is used by PYTHIA (v6.3) to generate the $pp \to ZZ \to \ell\ell\ell\ell$ signal Monte Carlo samples at LO, which are used here. The cross-section at LO in the CTEQ6 case is 9.6 pb, requiring that $Z/\gamma^\star$ are on-mass-shell. Relaxing this requirement to include also off-mass-shell Z boson with $m(Z/\gamma^\star) > 12\ GeV$ gives a cross-section of 11.2 pb.

The NLO calculations give higher production cross-sections with a k-factor (K_f), defined as $K_f = \sigma(NLO)/\sigma(LO)$, of 1.35 when both Z bosons are on-mass-shell. Nevertheless, it is important to stress that the K_f is not constant but is highly correlated to the four lepton invariant mass with an average value of 1.35, while it varies in the mass range $115-405\ GeV$ from 1.15 to 1.52. This dependence is evaluated using MCFM MC calculations [60].

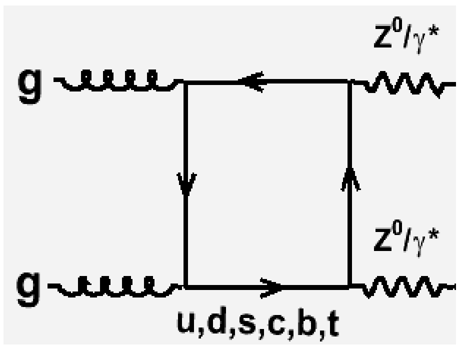

Figure 7.2: **Feynman diagram of ZZ production via gluon-gluon fusion** - The contribution to the cross-section by this diagram is around 20%.

There is also a significant NNLO contribution in the production cross-section of the order of $\sim 20\%$ from gluon-gluon fusion process [61], which is illustrated in the Feynman diagram of Fig.7.2, but this is not included in the MC simulation here.

7.3 Event generation

7.3.1 Signal

The $q\bar{q} \rightarrow ZZ \rightarrow \ell\ell\ell\ell$ signal has a very clean signature with four isolated and high-p_T leptons in the final state. The event topologies that are studied here are the $\mu^+\mu^-\mu^+\mu^-$, $e^+e^-e^+e^-$ and $\mu^+\mu^-e^+e^-$. Two "filter" cuts are used at generation level in order to keep only events with leptons which have $p_T > 5$ and lie in the rapidity region $|\eta| < 2.7$. The reasons for imposing these filters are related to detector design constrains and the need to increase the available statistics of the simulated samples used for analysis, since the acceptance of the MS is $|\eta| < 2.7$ and the ID's $|\eta| < 2.5$. The overall "filter" efficiency on the $q\bar{q} \rightarrow ZZ \rightarrow \ell\ell\ell\ell$ production in Pythia is $\epsilon_{filter} = 21.9\%$.

The $Z/\gamma^\star$ interference terms are included in Pythia . With the mass cut on the dileptons decay from $Z/\gamma^\star$ at 12 GeV, the production cross section times the branching ratio of $Z \rightarrow \ell^+\ell^-$ decay for three flavours $\ell = \mu, e, \tau$ is 159 fb. Note that the branching ratio of $\tau \rightarrow \ell$ is accounted for in the "filter" efficiency since events with hadronic decays of τ's are not kept at generation level. The fraction of each event topology in the total number of generated events is given in Table 7.2. In this table the contribution of the leptonic decays of τ's is also given, however the event topologies $3e1\mu$ and $3\mu1e$ which arise from at least one Z boson decaying to a τ pair are not studied here. These events constitute the 3.32% of the total number of $ZZ \rightarrow 4\ell$ events. It is important to note that for completeness it would have been more precise to include the contribution of the τ leptonic decay to the other three event configurations when calculating efficiencies, however as it will be explained in section 7.4.3, applying a mass constrain to the Z bosons, reduces the number of events with a Z decaying to τ's, to negligible levels. It is therefore not included in efficiency calculations in the following sections. The basic properties of

Channel	Fraction in $ZZ \to 4\ell$ [%]	Channel	$\tau \to e, \mu$ contribution [%]
$ZZ \to 4\mu$	23.41	$ZZ \to 4\mu$	1.17
$ZZ \to 4e$	22.70	$ZZ \to 4e$	0.97
$ZZ \to 2\mu 2e$	46.56	$ZZ \to 2\mu 2e$	1.87
$ZZ \to 2\tau 2\ell$	7.33	$ZZ \to 3\mu 1e$	1.76
		$ZZ \to 1\mu 3e$	1.56
Total	100.0	Total	7.33

Table 7.2: **The composition of the $ZZ \to 4\ell$ sample according to the final state configuration and the contribution to the five possible event topologies from the τ leptonic decays of the Z's.**

the PYTHIA signal sample used in the analysis are illustrated in the first column of Table 7.3. In total 43000 events are analysed corresponding to luminosity of:

$$L = \frac{N}{\sigma \times BR \times \epsilon_{filter}} = \frac{43000}{159 \times 0.219} = 1234.9\ fb^{-1} \tag{7.2}$$

Before going to details on the analysis, it is meaningful to look at the four lepton invariant mass distributions of the $ZZ \to 4\ell$ topology in the PYTHIA generated data, to validate the shape of the distributions and identify the different mass regions. In Fig.7.3(a) the MC invariant mass distributions of the four leptons for the cases $\mu^+\mu^-\mu^+\mu^-$, $e^+e^-e^+e^-$, $\mu^+\mu^-e^+e^-$ are shown. Two striking regions can be observed. The first one with the clear peak around 200 GeV corresponds to the region where both Z bosons are on-mass-shell. The second one lies below 200 GeV and exhibits two structures which correspond to the cases that one or both Z's are off-mass-shell. This classification is nicely illustrated in Fig.7.3(b) where the correlation between the masses of the two Z's is shown. Note that the distributions of Fig.7.3(a) are drawn before any cut is applied.

From the distributions of Fig.7.3(a) it is easy to classify each event to three categories, ZZ, $ZZ^\star$ and $Z^\star Z^\star$, according to either the on-mass-shell definition of the Z or the invariant mass of the ZZ pair. The fraction of events is shown in Table 7.4 where in the first column the on-mass-shell window lies between $70 - 110$ GeV, while in the second column the window is $M_Z \pm 5\Gamma_Z$, given that values for the

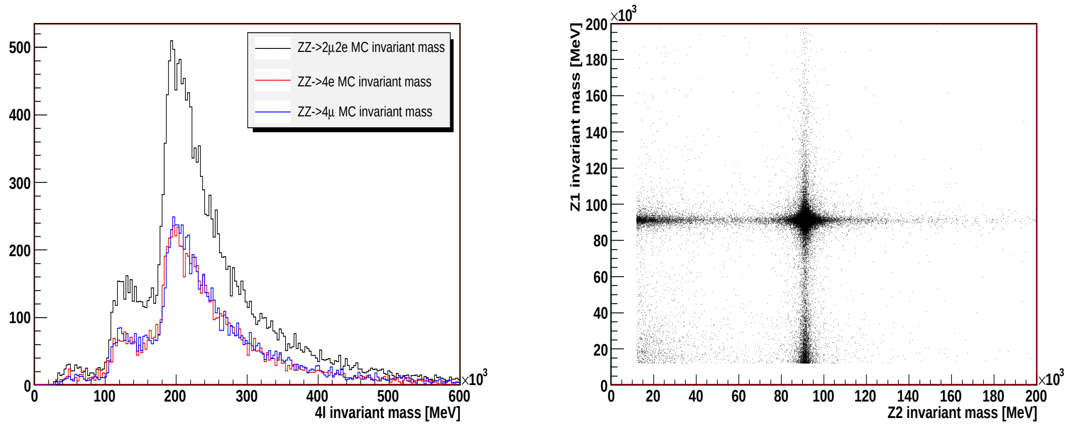

(a) MC Invariant mass of the four leptons for the cases $\mu^+\mu^-\mu^+\mu^-$, $e^+e^-e^+e^-$ and $\mu^+\mu^-\mathrm{e}^+\mathrm{e}^-$.

(b) Correlation between the MC masses of the two Z bosons.

Figure 7.3: **Monte Carlo four lepton invariant mass distributions and mass correlations of the two Z bosons.**

mass and the width of the Z are taken from reference [10] as $M_Z = 91.19\ GeV$ and $\Gamma_Z \simeq 2.5\ GeV$. In the third column the ZZ window opens above $2M_Z$ while the ZZ^* and Z^*Z^* lie in the regions $100 - 2M_Z$ and $< 100\ GeV$ respectively.

Process	$pp \to ZZ \to 4\ell$	$pp \to Zb\bar{b} \to 4\ell$	$pp \to t\bar{t} \to 4\ell$
$\sigma[pb]$	11.2	52	833
Filter	$\mid \eta \mid < 2.7$, $p_T > 5\mathrm{GeV}$	$Zb\bar{b} \to \ell\ell\ell\ell$	$t\bar{t} \to \ell\ell\ell\ell$
ϵ_{filter}	0.219	0.00942	0.00728
K-factor	1.35	1.42	-
Events	43000	313689	152701
$L[fb^{-1}]$	1234.9	640	25.2

Table 7.3: **Basic properties of signal and background samples.**

In the analysis sections that follow, two different mass regions are adopted as constrain on one or both Z mass. The region, characterized hereafter as "tight", requires both Z's to have reconstructed invariant mass between 70 and 110 GeV. This

	$70 < m_Z < 110[\%]$	$m_Z \pm 5{\times}\Gamma_Z[\%]$	$m_{ZZ} > 2M_Z[\%]$
ZZ	72.9	69.1	80.0
ZZ^*	23.4	26.4	17.6
Z^*Z^*	3.7	4.5	2.4

Table 7.4: **Fraction of events $Z^{(\star)}Z^{(\star)}$ in the PYTHIA sample classified according different mass regions.**

corresponds to Z's with generated mass $\pm 5\sigma$ around the mass value and therefore represents $\sim$ 70% of the PYTHIA sample. The second mass region, characterized hereafter as "loose", requires one Z between 70 GeV and 110 GeV and the second Z invariant mass to be greater than 20 GeV. This corresponds to 89% of the PYTHIA sample. It is important to define the mass region using the constrain on the Z mass (one or both) instead of the reconstructed four lepton invariant mass in order to eliminate combinatorials and background events as it will be shown in section 7.4.

Since the transverse momentum of the leptons is a variable that is used later in the analysis as a signal to background discriminating observable, the leptons p_T distributions in the MC PYTHIA sample, of each $ZZ^{(*)}$ decay topology studied here, are shown in Fig.7.4. Note that each plot corresponds to different lepton flavour.

7.3.2 Background

Any process containing four leptons in the final state is a possible source of background to the $ZZ \rightarrow 4\ell$ channel. The main backgrounds are:

- $pp \rightarrow t\bar{t} \rightarrow WW\ b\bar{b}$

  The production of $t\bar{t}$ pairs will be dominant at the LHC because of the huge production cross section of 833 pb at NLO [62] resulting in 8×10^6 events per year at low luminosity. For $ZZ \rightarrow 4\ell$, the decay of the $t\bar{t}$ pair is a source of background when both W bosons decay leptonically and the other two leptons come from the semileptonic decay of the two b-quarks. The large production cross section necessitates the use of four lepton final state "filter"

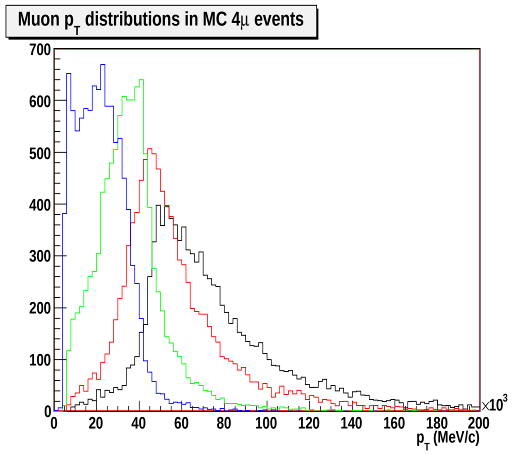

(a) Ordered p_T distributions of the 4 muons in $\mu^+\mu^-\mu^+\mu^-$ events.

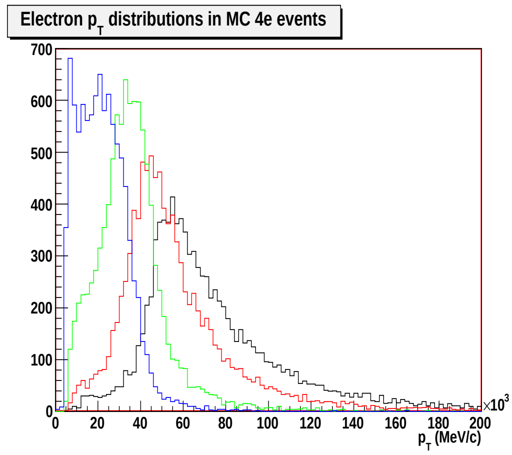

(b) Ordered p_T distributions of the 4 electrons in $e^+e^-e^+e^-$ events.

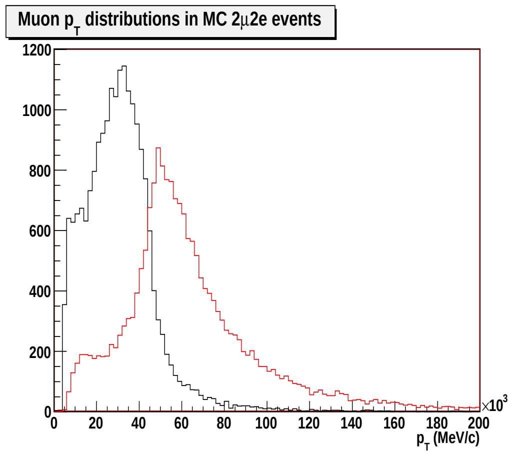

(c) Ordered p_T distributions of the 2 muons in $\mu^+\mu^-\mathrm{e}^+\mathrm{e}^-$ events.

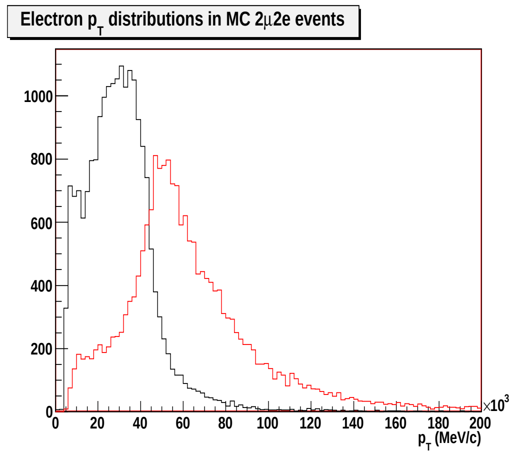

(d) Ordered p_T distributions of the 2 electrons in $\mu^+\mu^-\mathrm{e}^+\mathrm{e}^-$ events.

Figure 7.4: **Lepton MC p_T distributions for the $\mu^+\mu^-\mu^+\mu^-$, $e^+e^-e^+e^-$ and $\mu^+\mu^-\mathrm{e}^+\mathrm{e}^-$ event topologies.**

cuts at generation level in order to increase the statistics. In total, 152701 $t\bar{t}$ events, generated with Mc@nlo generator [63], with full ATLAS simulation, are analysed, corresponding to integrated luminosity of $L = 25.2\ fb^{-1}$, given that the filter efficiency is 0.00728.

- $pp \rightarrow Z + jets$

The elimination of this background is more difficult since the topology includes a genuine Z. The production of four leptons from this process proceeds when the Z boson decays leptonically accompanied by leptons in heavy quark jets, typically jets from b or c quarks, or leptons in light quark jets or jets misidentified as leptons. In the $Zb\bar{b}$ case which is studied here, the production LO cross-section is 52 pb. In total 313689 $Zb\bar{b}$ events generated withPYTHIA and interfaced with ACERMC [64] for the hadronization and underlying event processes, are analysed and similarly to the $t\bar{t}$ case a four lepton "filter" cut is imposed at generation level with efficiency 0.00942. The corresponding integrated luminosity is 640 fb^{-1}.

- $pp \rightarrow WZ$

  This process is also a possible source of background when both W and Z bosons decay leptonically and a fake reconstructed lepton is included as the fourth component of the topology. Although the cross-section of this channel is comparable to the $Zb\bar{b}$ case – the SM predicts the total W^+Z^0 production cross section to be 29.4 pb and the W^-Z^0 production cross section to be 18.4 pb at NLO [58, 65] and when multiplied by the branching ratio for the $WZ \rightarrow \ell\nu\ell\ell$ gives 441.7 fb and 276.4 fb respectively – the subsidiary requirement of a fake lepton present, brings the overall contribution of this background process down to insignificant values. This is because the expected fake rate for example in muons is less than 2% per triggered event at low luminosity and can be further suppressed requiring a combined muon track with $p_T > 5\ GeV$ [9]. Fake electrons can be also suppressed, by similar E_T requirements, to very low levels. Therefore this background channel is not studied here.

The basic properties of the background samples are shown in the last two columns of Table 7.3.

7.4 Event selection

Event selection and background rejection is mainly based on the requirement that the experimental signature of ZZ production is high-p_T isolated muons and electrons. At the same time the $Zb\bar{b}$ background is expected to have two high energetic leptons produced by the decay of the Z boson and another two softer leptons coming from the two b-quarks. These last two leptons though are expected to be produced within a jet of hadrons therefore they will not be isolated. This is also the picture one can expect in the $t\bar{t}$ background where the lepton from the W decay is anticipated to be isolated and more energetic than the non isolated leptons produced from the hadronization of b-quarks into jets.

On the one hand, identification and observable quantities of muons are provided by Staco reconstruction algorithm and on the other hand the reconstruction algorithm which fills all electron related physical quantities is Egamma [66]. One essential step before the main analysis procedure to select the $ZZ^{(*)}$ candidates, is to "clean up" for each event the objects identified as muons and/or electrons. For muons these pre-selection criteria are:

1. $p_T > 6\ GeV$ - This cut helps rejecting muons from the background processes, fakes or muons coming from the spectator quarks of the collision. In principle, these muons are much softer than the muons of the signal process.

2. $|\eta| < 2.7$ - This cut is imposed by the MS coverage which extents up to 2.7 in η and acts only as a precaution in case a reconstructed muon has been wrongly assigned an η value outside the actual detector's acceptance.

3. Muon tracks should be "combined", which means that Staco has successfully associated a track reconstructed in the MS with a track reconstructed in the ID. The combined track requirement is applied in the pseudo-rapidity range -2.5 to 2.5. Note that this requirement applies up to the acceptance of the ID system at $\eta = 2.5$. From that point, up to the limit of the MS acceptance at $\eta = 2.7$ tracks are required to have been reconstructed by the MS stand-alone.

4. All track fits should have $\chi^2/ndf < 15$ (where ndf is number of degrees of freedom) and the matching of the associated MS and ID tracks should also have $\chi^2/ndf < 15$.

For electrons the set of pre-selection cuts is:

1. $p_T > 6\ GeV$

2. $|\eta| < 2.5$

3. $0.5 < E/P < 3.0$, where E is the energy of the electron measured in the calorimeter and P is the momentum of the associated electron track in the ID.

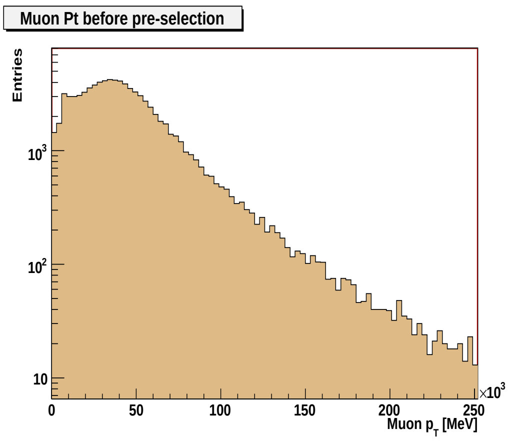

(a) Muon p_T distribution in $ZZ \to 4\ell$ events.

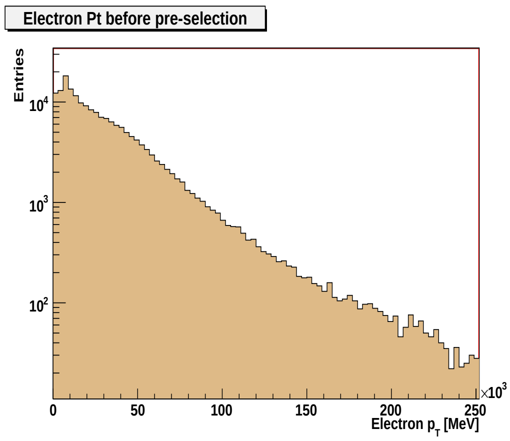

(b) Electron p_T distribution in $ZZ \to 4\ell$ events.

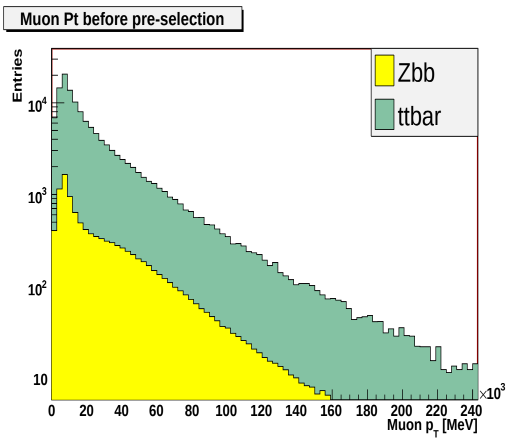

(c) Muon p_T distribution in background events.

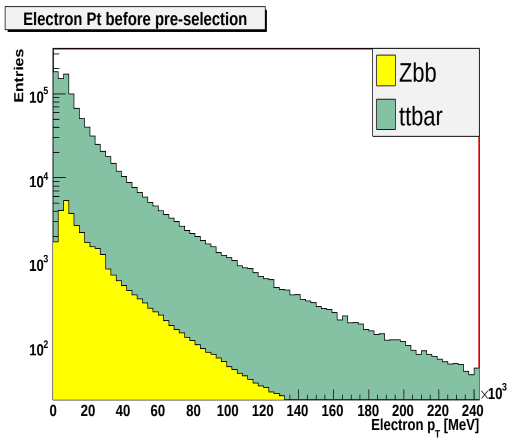

(d) Electron p_T distribution in background events.

Figure 7.5: **Reconstructed lepton initial p_T distributions in signal and background events** - Distributions in background are normalized to the same luminosity.

In addition to the above cuts, the number of leptons in each event is required to be at least four and their flavour should correspond to the three event topologies $\mu^+\mu^-\mu^+\mu^-$, $e^+e^-e^+e^-$ and $\mu^+\mu^-\mathrm{e}^+\mathrm{e}^-$. Therefore events with four or more muons, four or more electrons and events with at least two or more leptons of each flavour are retained. Note that after these pre-selection criteria the number of events that appear in more than one topology is negligible. Nevertheless, in case such an event exists, it is classified to the $\mu^+\mu^-e^+e^-$ topology but does not survive the rest of the cut flow which is described later. The initial p_T distributions of the reconstructed leptons for both signal and background are given in Fig.7.5.

Another two basic selection criteria are applied at this step. Leptons form pairs of the same flavour and opposite charge in each topology. Pairs with both leptons lying within a cone of radius $\Delta R < 0.2$ are rejected because muons or electrons from the Z decays have large opening angle. Each of the formed pairs is in fact one Z candidate which combined in doublets forms one four lepton event candidate. The total efficiency of the pre-selection cuts described above, is given later together with the efficiency of the rest of the selection cuts that are used in the analysis, for both signal and background.

7.4.1 Isolation cuts

Isolation criteria are applied to each of the four leptons in all topology cases. For muon isolation the variable I is defined as,

$$I = \frac{E_T^{0.4}}{E_T^{\mu}} \tag{7.3}$$

where $E_T^{0.4}$ is the transverse energy in a cone around the muon track of radius $\Delta R = 0.4$ and E_T^{μ} is the transverse energy of the muon. A muon is considered isolated if $I < 0.2$. Fig.7.6 shows the distribution of the muon isolation variable I for each of the four muons in the $\mu^+\mu^-\mu^+\mu^-$ topology, for both signal and background. Note that distributions in each plot are normalized with respect to the same number of events. It is evident that both backgrounds have distributions with a much bigger tail towards higher values of I which is expected since leptons in the $t\bar{t}$ case are not isolated and the leptons in the $Zb\bar{b}$ emerging from the b-quarks are also non-isolated.

In the electron case it was not possible to use the same variable I that was used for muons because in the particular ATHENA release the isolation transverse energy calculation was not reliable. Therefore for electron isolation, a series of cuts based

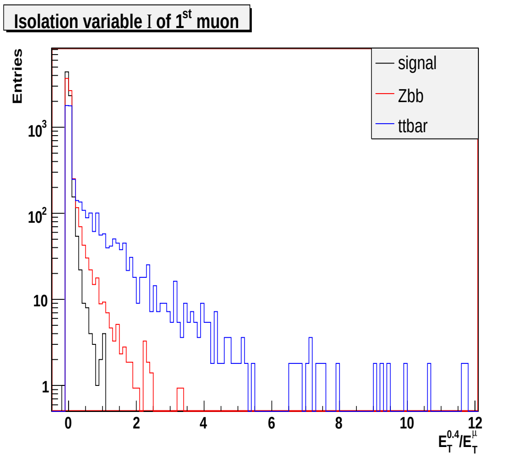

(a) Isolation variable I of the 1^{st} muon in 4μ events

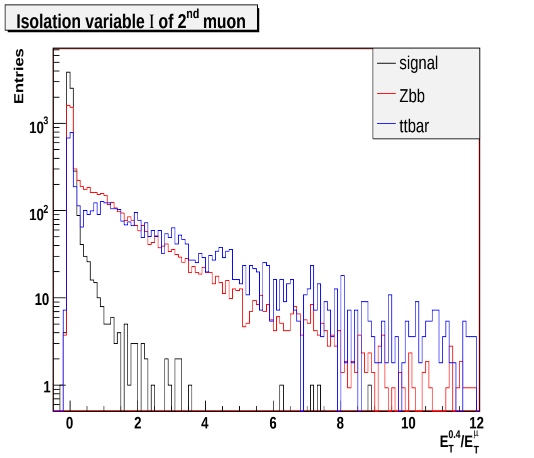

(b) Isolation variable I of the 2^{nd} muon in 4μ events

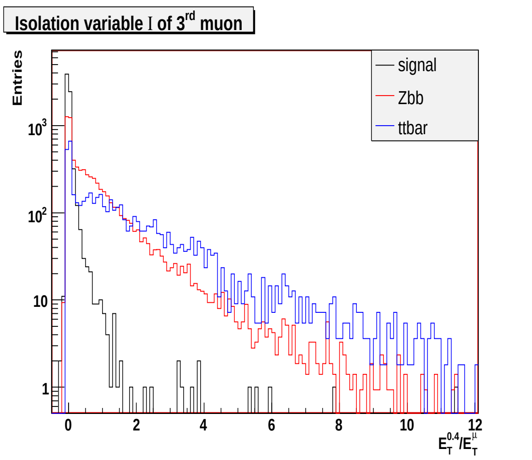

(c) Isolation variable I of the 3^{rd} muon in 4μ events

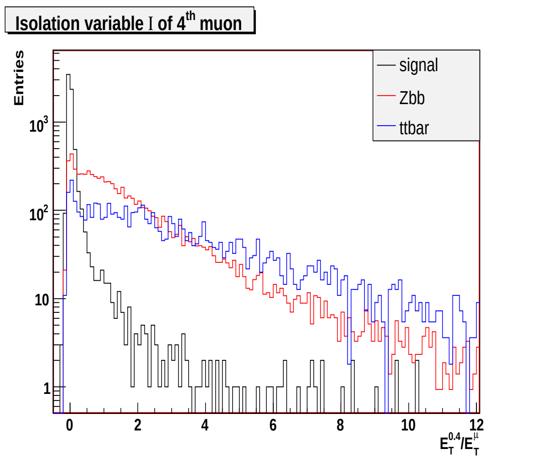

(d) Isolation variable I of the 4^{th} muon in 4μ events

Figure 7.6: **Muon isolation variable I for signal and background in the 4 muon final state case** - Distributions are normalized to the same number of events.

on the properties of the shower shape in different compartments of the calorimeter is used. This information is contained in a condensed form in a 32-bit integer, the so-called `isEM` flag [67]. If a cut is not passed, then a bit is set in the `isEM` flag. An electron is considered isolated if the first four bits of the `isEM` flag are set, i.e (isEM & 0xF) == 0. The first four bits represent cuts which are only calorimeter based and in particular consist of:

1. a rapidity range cut in the middle layer of the LArEM calorimeter
2. an η dependent cut on the hadronic leakage
3. η and E_T bin-dependent cut on the energy in the middle sampling layer.
4. η and E_T bin-dependent cut on the energy in the first sampling layer.

7.4.2 Maximum p_T cut

The striking difference in the p_T distributions of the leptons in the ZZ signal and the background processes, which can be exploited in background rejection, is the much softer p_T distributions of leptons in the background processes. In the $Zb\bar{b}$ case this is because two of the final state electrons or muons emerge from b-quark jets. In the $t\bar{t}$ case, the final leptons are produced also from the decay of b-quarks in addition with the leptons coming from the decay of the two W's which are also softer that the ones coming from the Z boson decay. Taking into account the above considerations, at least one lepton in each pair candidate is required to have $p_T > 20\,GeV$.

The p_T distribution of the lepton with the highest p_T in each pair of electrons and muons is shown in Fig.7.7. Fig.7.7(a) and 7.7(b) correspond to the $\mu^+\mu^-\mu^+\mu^-$ and $e^+e^-e^+e^-$ case respectively, while Fig.7.7(c) and 7.7(d) to the highest muon and electron of the $\mu^+\mu^-\mathrm{e}^+\mathrm{e}^-$ case.

The choice of the particular values of the cuts rests in the investigation of the effect of a range of values on the maximization of the signal efficiency and the coinstantaneous minimization of the background efficiency. Plots in Fig.7.8 show the efficiency of the p_T^{max} and isolation cuts for the $\mu^+\mu^-\mu^+\mu^-$ event topology, while plots in Fig.7.9 show the p_T^{max} cut efficiency also for the $e^+e^-e^+e^-$ and $\mu^+\mu^-\mathrm{e}^+\mathrm{e}^-$ final state cases. For a p_T cut at 20 GeV, in all cases approximately 95% of the signal is preserved while the background rejection is $\sim$ 20% on the $Zb\bar{b}$ and $\sim$ 35% on the $t\bar{t}$.

For isolation, in the case of the 4μ topology the value $I = 0.2$ is a good compromise between maintaining the selection of backgrounds at very low levels $< 0.5\%$ and losing no more than $\sim$ 18% of signal.

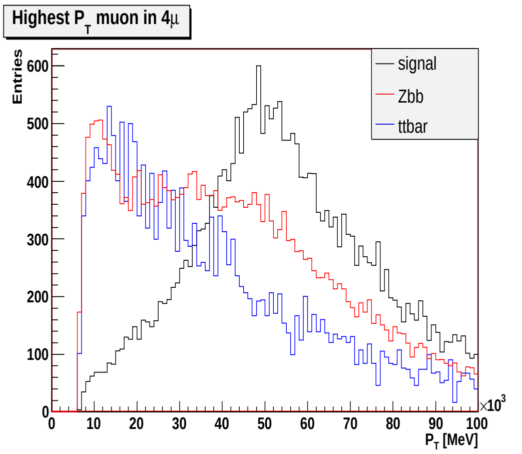

(a) p_T of the hardest muon in the $\mu^+\mu^-\mu^+\mu^-$ case

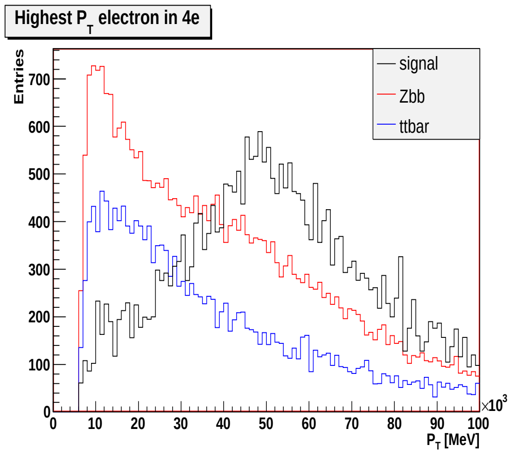

(b) p_T of the hardest electron in the $e^+e^-e^+e^-$ case

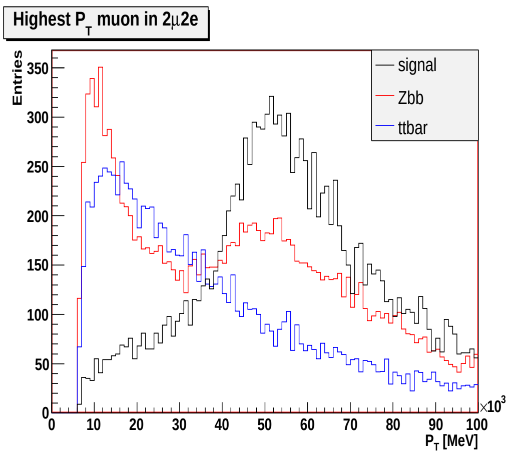

(c) p_T of the hardest muon in the $\mu^+\mu^-\mathrm{e}^+\mathrm{e}^-$ case

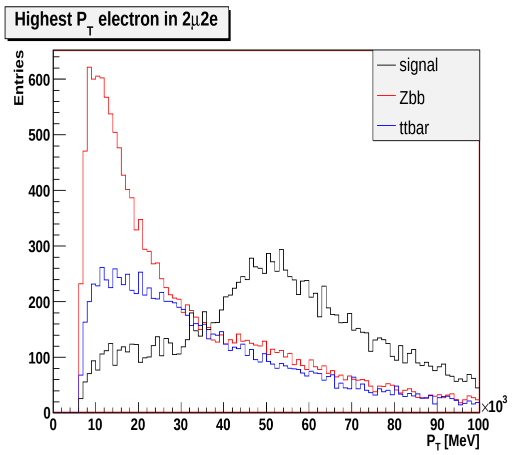

(d) p_T of the hardest electron in the $\mu^+\mu^-\mathrm{e}^+\mathrm{e}^-$ case

Figure 7.7: p_T **distributions of the highest** p_T **lepton for signal and background** - Distributions are normalized to the same number of events.

7.4.3 Z mass cut

Although very powerful, the isolation and p_T^{max} cuts do not eliminate all of the $t\bar{t}$ and $Zb\bar{b}$ backgrounds. In addition, one important issue at this stage is the combinatorial background which is induced by the lepton quadruplet formation. Both combinatorial and physics backgrounds can be further reduced by constraining the reconstructed mass of the Z candidates in the "tight" or "loose" mass regions de-

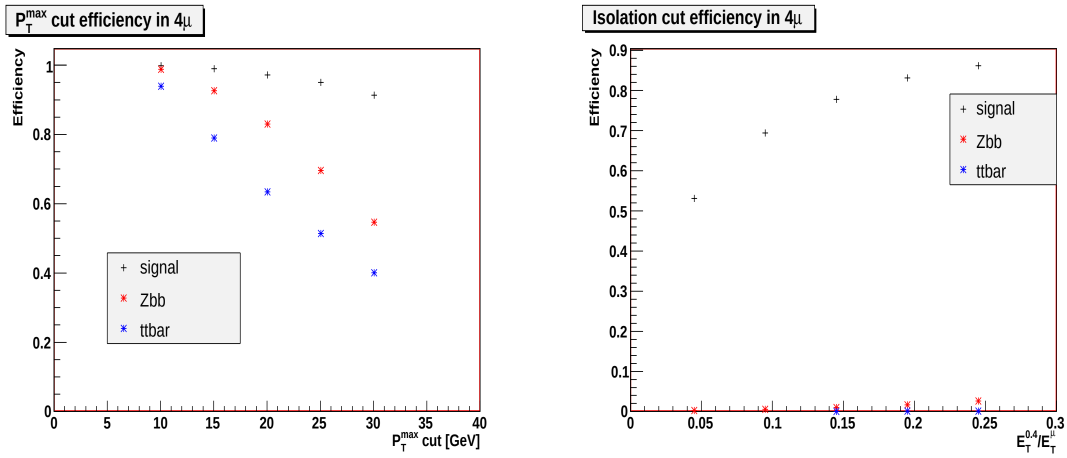

(a) Efficiency of the p_T^{max} cut (b) Efficiency of the isolation cut

Figure 7.8: **Efficiency of p_T^{max} and the isolation cuts, for the $\mu^+\mu^-\mu^+\mu^-$ case.**

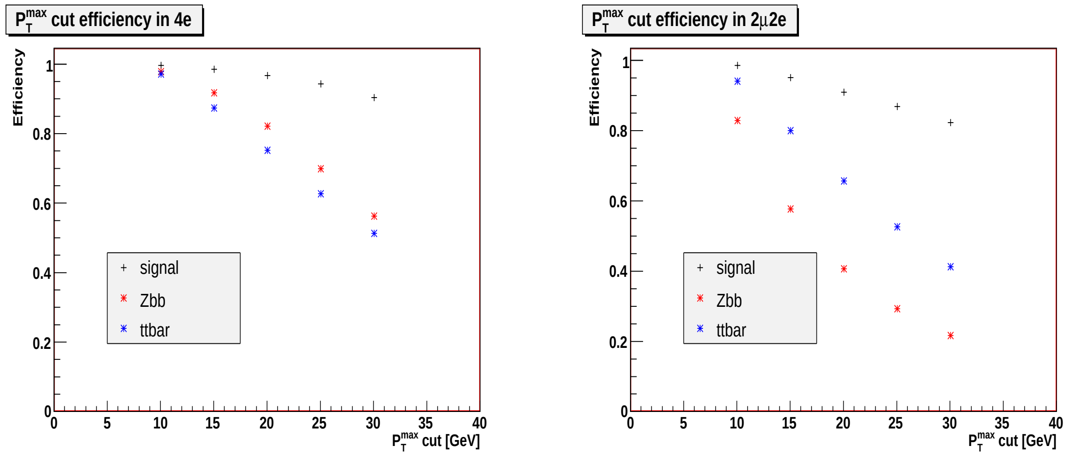

(a) Efficiency of p_T^{max} cut for the $e^+e^-e^+e^-$ case (b) Efficiency of p_T^{max} cut for the $\mu^+\mu^-\mathrm{e}^+\mathrm{e}^-$ case

Figure 7.9: **Efficiency of p_T^{max} cut for the $e^+e^-e^+e^-$ and $\mu^+\mu^-\mathrm{e}^+\mathrm{e}^-$ cases.**

scribed in section 7.3.1. However, even with this constrain it is still possible to have more than one possible quadruplet combination in the end. In such cases the quadruplet which contains the Z candidate with mass closer to the SM value of 91.19 GeV is retained.

The tight mass region requires both Z bosons in the range 70 GeV to 110 GeV while the loose region requires one Z within 70–110 GeV and the second Z with a mass greater than 20 GeV. The events of this category constitute the irreducible background to the $H \rightarrow ZZ^* \rightarrow 4\ell$ and it is therefore important to measure its shape and give an estimate on the expected number of signal events. Results presented in the next section are given for both mass cases, tight and loose.

7.5 Cut efficiency

The cut flow described in the previous section and the efficiency of each of these cuts for the three signal event topologies, is given in Table 7.5. The lepton pre-selection efficiency is calculated with respect to the initial number of events in each topology, while the efficiencies for each set of cuts are computed with respect to the previous one. The product of the relative efficiencies agrees with the ratio of the reconstructed events after all cuts to the generated ones. The errors in the last row of this table are statistical only assuming to be gaussian.

Table 7.5: **Signal selection cut efficiencies.**

	4μ [%]		$4e$ [%]		$2\mu 2e$ [%]	
Lepton Preselection	70.67		62.27		65.40	
Pair formation,ΔR	99.34		87.97		93.37	
p_T^{max}	97.18		96.68		90.97	
Isolation	83.47		60.64		64.94	
Z Mass	Tight	Loose	Tight	Loose	Tight	Loose
	72.68	91.99	76.09	93.47	77.81	95.19
Total	41.39 ± 0.64	52.38 ± 0.72	24.43 ± 0.50	30.01 ± 0.56	28.07 ± 0.37	34.34 ± 0.41

Table 7.6: $Zb\bar{b}$ **background cut efficiencies.**

	4μ [%]		$4e$ [%]		$2\mu 2e$ [%]	
Lepton Preselection	6.33		10.70		18.36	
Pair formation,ΔR	77.29		59.08		48.49	
p_T^{max}	83.01		82.18		40.69	
Isolation	1.55		5.20		1.60	
Z Mass	Tight	Loose	Tight	Loose	Tight	Loose
	2.03	24.87	2.24	25.59	8.79	69.76
Total($\times 10^{-3}$)	1.28 ± 0.64	15.62 ± 2.23	6.06 ± 1.39	69.16 ± 4.70	5.10 ± 1.28	40.48 ± 3.59

Table 7.7: $t\bar{t}$ **background cut efficiencies**.

	4μ [%]		$4e$ [%]		$2\mu 2e$ [%]	
Lepton Preselection	3.20		24.84		36.12	
Pair formation,ΔR	62.69		53.59		43.59	
p_T^{max}	63.40		75.17		65.70	
Isolation	0.21		0.41		0.18	
Z Mass	Tight	Loose	Tight	Loose	Tight	Loose
	25.00	50.00	1.61	20.97	3.45	37.93
Total($\times 10^{-3}$)	0.66 ± 0.66	1.31 ± 0.93	0.66 ± 0.66	8.51 ± 2.36	$< 1.60 \pm 1.02$	7.20 ± 2.17

For the $t\bar{t}$ and $Zb\bar{b}$ backgrounds Tables 7.6 and 7.7 provide the corresponding efficiencies of the same cuts. The efficiency value of a cut refers to previous cut in the row apart from the first one which refers to the total number of generated background events. Errors here are also assumed gaussian. As already observer in the individual efficiency plots of p_T and isolation cuts, the vast majority of the background in both processes is rejected by these two selection criteria where for the $t\bar{t}$ the efficiency is of the order of $< 0.5\%$ and for the $Zb\bar{b}$ of the order of $\sim 1\%$. There is however a discrepancy in the efficiency of the isolation cut between the 4μ and $4e$ topologies. This can be explained by the fact that for electron isolation the criteria based only on the `isEM` flag are not as strict as the isolation variable I defined for muons.

7.6 Expected signal and background

In Fig.7.10, 7.11 and 7.12 the invariant mass distributions of the four leptons in the 4μ,$4e$ and $2\mu 2e$ final state cases respectively, are given after all selection cuts are applied. The figures include two kind of plots depending on the mass regions defined for the Z bosons. Distributions for the tight mass region are shown on the left plots while the ones for the loose mass region are shown on the right. Both backgrounds, $t\bar{t}$ and $Zb\bar{b}$ are drawn on the same plots which are all normalized to 10 fb^{-1}. The $ZZ \rightarrow 4\ell$ signal and the $Zb\bar{b}$ background distributions also include the k-factor contribution, with $K_f = 1.35$ for ZZ and $K_f = 1.42$ for the $Zb\bar{b}$. Finally, in Fig.7.13 the invariant mass of all 4-lepton cases is drawn, again for the two mass regions.

It is evident, especially in the plots corresponding to the loose mass region, that the $Zb\bar{b}$ and $t\bar{t}$ background have an impact on the low invariant mass regions, which is very small though. In the topology $2\mu 2e$ using the tight Z mass constrain, there are no events left after all the cuts from the $t\bar{t}$ process and this is why this contribution is missing from the corresponding plot.

The expected number of signal and background events for each of the three final state configurations at 1 fb^{-1} is given in Table 7.8 for the tight Z mass constrain and in Table 7.9 for the loose Z mass constrain. Errors shown are statistical only.

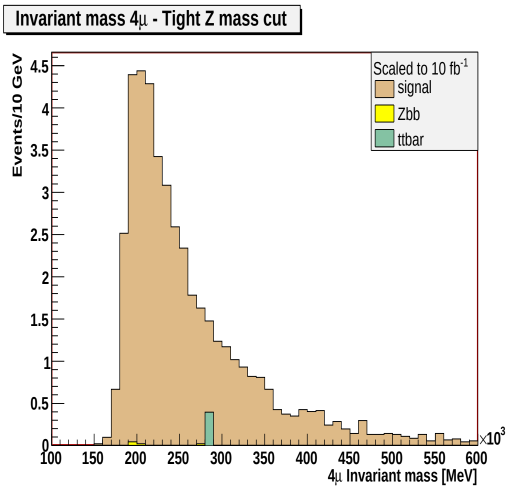

(a) Invariant mass of 4μ after all cuts, for signal and background using the tight Z mass cut region.

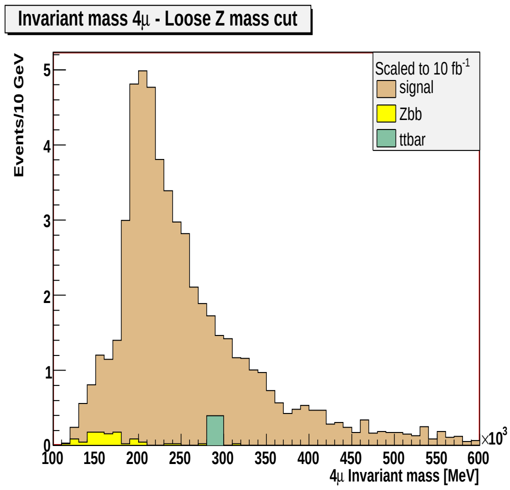

(b) Invariant mass of 4μ after all cuts, for signal and background using the loose Z mass cut region.

Figure 7.10: **Invariant mass of 4μ after all cuts, for signal and background.**

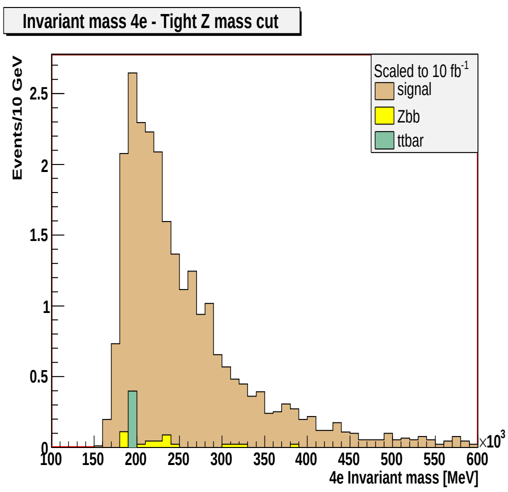

(a) Invariant mass of $4e$ after all cuts, for signal and background using the tight Z mass cut region.

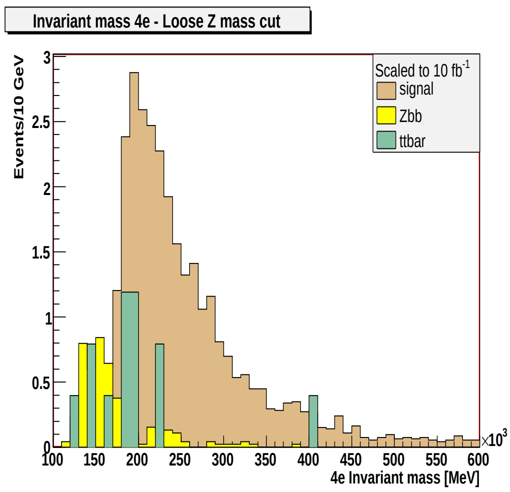

(b) Invariant mass of $4e$ after all cuts, for signal and background using the loose Z mass cut region.

Figure 7.11: **Invariant mass of $4e$ after all cuts, for signal and background.**

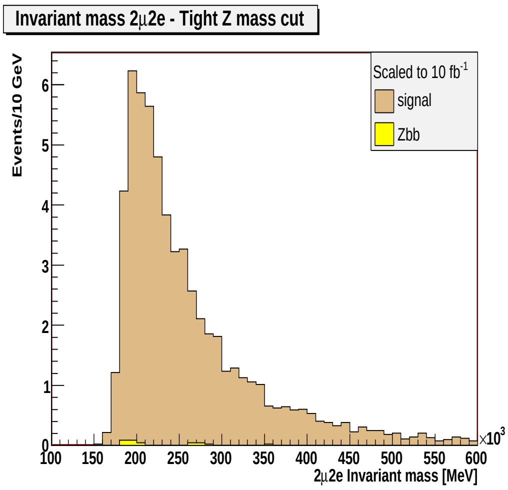

(a) Invariant mass of $2\mu 2e$ after all cuts, for signal and background using the tight Z mass cut region.

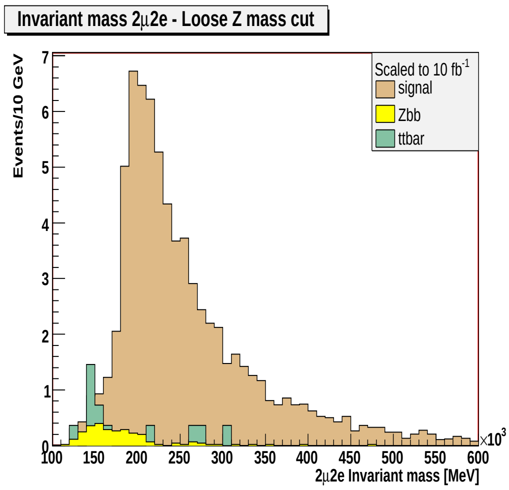

(b) Invariant mass of $2\mu 2e$ after all cuts, for signal and background using the loose Z mass cut region.

Figure 7.12: **Invariant mass of $2\mu 2e$ after all cuts, for signal and background.**

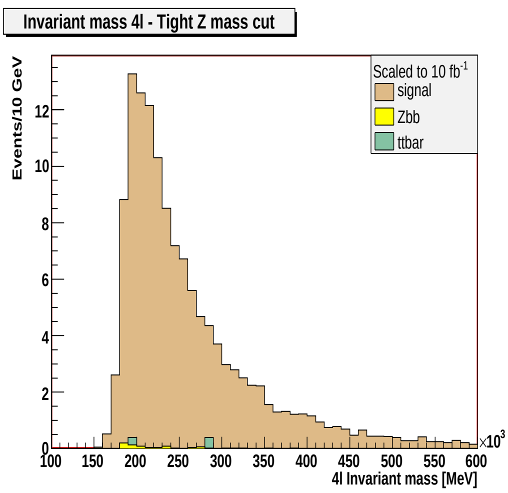

(a) Invariant mass of 4ℓ after all cuts, for signal and background using the tight Z mass cut region.

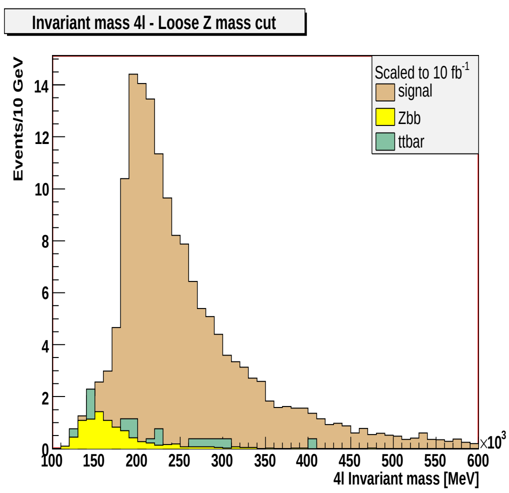

(b) Invariant mass of 4ℓ after all cuts, for signal and background using the loose Z mass cut region.

Figure 7.13: **Invariant mass of 4ℓ after all cuts, for signal and background.**

	4μ events	$4e$ events	$2\mu 2e$ events	Total
Signal	4.53±0.06	2.58±0.05	6.18±0.07	13.29 ±0.10
$Zb\bar{b}$	0.009±0.004	0.042±0.008	0.034±0.007	0.085±0.012
$t\bar{t}$	0.04±0.04	0.04±0.04	<0.097±0.062	<0.177±0.08
Backgr. total	0.049±0.040	0.082±0.041	<0.131±0.040	<0.26±0.08

Table 7.8: **Expected signal and background events at $L = 1fb^{-1}$ using the tight Z mass cut.**

	4μ events	$4e$ events	$2\mu 2e$ events	Total
Signal	5.73±0.07	3.18±0.05	7.56±0.08	16.47 ±0.12
$Zb\bar{b}$	0.11±0.01	0.48±0.03	0.28±0.02	0.87±0.04
$t\bar{t}$	0.08±0.06	0.52±0.14	0.44±0.13	1.03±0.20
Backgr. total	0.19±0.06	1.00±0.15	0.72 ±0.13	1.90±0.21

Table 7.9: **Expected signal and background events at $L = 1fb^{-1}$ using the loose Z mass cut.**

With 1 fb^{-1} of data we expect a total of 13.3 and 16.5 signal events respectively in the two mass regions, and < 0.26 and 1.90 background events. Note that in the $t\bar{t}$ case and in particular the $2\mu 2e$ topology, the number of events surviving the cuts is zero. Here, the Poisson interval upper limit for zero mean is used at 90% confidence level [68], therefore the expected number of events in this case normalized to 1 fb^{-1} is less than 0.097.

One can conclude that the backgrounds, both $t\bar{t}$ and $Zb\bar{b}$ are brought down to negligible levels and although the limited available statistics does not allow extracting a well defined shape for them, it is nevertheless possible to measure the $ZZ^{(*)}$ production cross-section with as little as 1 fb^{-1}.

7.7 Systematic uncertainties

The systematic uncertainties to the signal comprise of:

- The uncertainty in the luminosity which is estimated to 6.5% after the first

$0.3fb^{-1}$

- The uncertainty from the PDF's used to $\sim 3\%$
- The scaling uncertainty for the NLO calculations or equivalently to the K_f to $\sim 5\%$
- The uncertainty $\sim$ 3% due to lepton identification, assumed the same for electrons and muons.
- The background estimate systematic uncertainty which amounts to $\sim 2\%$ and is driven by the cross-section uncertainties

Assuming gaussian distributions for all the above uncertainties, the total systematic uncertainty to the signal amounts to 9.2%. As seen from this analysis the measurement of the ZZ and ZZ^* cross-section is essentially background free but at $L = 1fb^{-1}$ is dominated by statistical error. At $L = 10fb^{-1}$ the statistical error will drop to about 10% and systematic error will have a similar impact [69].

7.8 Summary

A complete study on the Z boson pair production through the decay process $ZZ^{(*)} \rightarrow 4\ell$ where $\ell = e, \mu$ has been performed using the ATLAS detector at the LHC. Analysis was done using full ATLAS simulation events for the signal and for the background processes $pp \rightarrow t\bar{t} \rightarrow 4\ell$ and $pp \rightarrow Zb\bar{b} \rightarrow 4\ell$. Kinematic and physics oriented cuts were applied to both signal and background events and the cut efficiencies were studied.

With only 1 fb^{-1} of data, 13.3 signal events are expected requiring that both Z bosons are on-mass-shell while 16.5 are expected in the $ZZ^{(*)}$ case. Backgrounds coming from the $t\bar{t}$ and $Zb\bar{b}$ cases were found to be negligible, contributing in total less than 0.26 events in the ZZ and 1.9 events in the $ZZ^{(*)}$ case where their effect is concentrated mainly to the low mass regions.

8
Conclusions

This thesis has presented two different aspects of important issues carried out towards the preparation of the ATLAS experiment. The first aspect covered reconstruction, identification and isolation studies of muons using the Muon Spectrometer and the Calorimetric System of the ATLAS detector. The second aspect consisted of simulations of physics processes in order to investigate the ability of ATLAS to detect the Z boson pair production through the decay to four leptons.

For studies of physics processes that include muons in the final state it is important to understand the performance and reconstruction capability of the Muon Spectrometer and in particular of the muon tracking chambers. To this end, the performance of a BIS type muon chamber was studied using data from the H8 testbeam at CERN. It has been shown that even with different illuminating conditions, that comprised of positron and muon beams, and at different particle incident angles, the performance of the chamber and track reconstruction algorithm, remains reliable. The use of dedicated calibration constants would improve the resolution of the chamber even further.

Another crucial issue for studies of physics processes with muons in the final state is the precise measurement of the muon momentum. For this, the Muon Spectrometer is designed to achieve a resolution of the order of $\sim 2\%$ for muons of 100 GeV energy and 10% for 1 TeV muons. The resolution depends on the energy loss which occurs in the calorimeters and should be corrected for, but in the case of catastrophic muon losses is difficult to estimate it analytically. The expectations that muons of 350 GeV energy will suffer catastrophic energy loss in the calorimeters has been investigated in this thesis, using testbeam data from the H8 and comparison with Monte Carlo simulation. The fraction of muons that deposit more than 20 GeV in the calorimeters has been measured to be of the order of $\sim 1\%$, which is in good agreement with the simulation.

Identification of muons with catastrophic energy losses was based on the measurement of the deposited energy in each calorimeter compartment at H8. This manifests the importance of the precise energy deposition measurement in each calorimetric compartment, in ATLAS as well. However, in ATLAS the energy deposition measurement addresses also imperative issues for track reconstruction and isolation. Within the context of this thesis, a software package that performs energy deposition measurements in the ATLAS calorimeters has been developed and is used in the Athena framework for filling isolation related variables at the AOD. Physics analysis can also profit from the developed method since it provides at the AOD, the selected calorimeter cells in a cone around the muon track allowing the recalculation of isolation variables offline. In the current thesis, it has been also shown using simulated $t\bar{t}$ events, that the information on the cells and the number of those that participate in the transverse energy deposition measurement, can be used as a discriminating variable between isolated and non isolated muons in the barrel region of ATLAS, since the average number of cells between the two cases is more than 4 times different in all cone sizes used. The suggested isolation variable is independent of the actual response of the calorimeter and cell calibration constants. Future work would involve studies on more physics processes and detector regions and in the presense of pile up as well.

Finally, the study performed in this thesis on the observation potential with the ATLAS detector of Z boson pair production through the decay of the pair to electrons and/or muons has provided with quantitave expectations of observation which amounts to 13.29±0.10 events for ZZ or 16.5±0.1 events for $ZZ^{(*)}$ with 1 fb^{-1}. Contributions from the background processes of $Zb\bar{b}$ and $t\bar{t}$, although using limited statistics, were found to be negligible compared to the signal and the total amount is less than 0.26±0.08 and 1.90±0.21 events respectively. Summarizing, observation of Z boson pair production at the LHC is possible with the ATLAS detector already in the first years of operation. This study has also assisted understanding the effect of the total and irreducible backgrounds to the Higgs boson production observability through its decay to four leptons which is expected if the Higgs mass lies in the intermediate region, $120 < m_H < 600\ GeV$. It was shown that the backgrounds affect mainly the low mass region. The next step to complement this analysis would be to increase the Monte Carlo statistics of the background processes in order to extract their shapes and develop methods to estimate them from real data.

Bibliography

[1] O. Brüning et al.. **LHC Design Report**. **v.1 : the LHC Main Ring**(CERN-2004-003-V-1), 2004.

[2] The ATLAS Collaboration. **Detector and Physics Performance Technical Design Report**. *CERN/LHCC/99-14*, **ATLAS TDR 14**, May 1999.

[3] The CMS Collaboration. **CMS Physics Technical Design Report, Volume II: Physics Performance**. *J. Phys. G: Nucl. Part. Phys.*, **34**:995–1579, 2007.

[4] The ALICE Collaboration. **ALICE Technical Proposal for a Large Ion Collider Experiment at the CERN LHC**. *CERN /LHCC / 95–71 LHCC / P3*, December 1995.

[5] The LHCb Collaboration. **LHCb technical proposal**. *CERN-LHCC-98-4*, 1998.

[6] Ab. Djouadi. **The Anatomy of Electro–Weak Symmetry Breaking. Tome I: The Higgs boson in the Standard Model**. *arxiv:hep-ph/0503172 v2*, May 2005.

[7] ALEPH Collaboration, DELPHI Collaboration, L3 Collaboration, OPAL Collaboration, and The LEP Working Group for Higgs Searches Boson. **Search for the Standard Model Higgs boson at LEP**. *Physics Letters B*, **565**:61–75, July 2003.

[8] The ATLAS Collaboration. **ATLAS Technical Proposal**. *LHCC/94-43;LHCC/P2*, December 1994.

[9] The ATLAS Collaboration. **The ATLAS Experiment at the CERN Large Hadron Collider**. *ATL-COM-PHYS-2007-102*. Submitted to JINST.

[10] W.-M. Yao et al.. **The Review of Particle Physics**. *Journal of Physics*, **G33**(1), 2006 and 2007 partial update for 2008.

[11] ATLAS Collaboration. **ATLAS magnet system: Technical design report**. *CERN-LHCC-97-18*, 1997.

[12] A. Dudarev et al.. **First full-size ATLAS barrel toroid coil successfully tested up to 22 kA at 4 T**. In *IEEE Tr. Appl. Superconductivity*, **15(2)**, pages 1271–1275, 2005.

[13] C. Beriaud et al.. **Quench Behavior of the ATLAS Barrel Toroid**. In *Paper presented at IEEE International Magnet Technology Conference*, 2007.

[14] The ATLAS Collaboration. **ATLAS Inner Detector Technical Design Report**. *LHCC/97-16;LHCC/97-17*, April 1997.

[15] The ATLAS Collaboration. **ATLAS Liquid Argon Calorimeter Technical Design Report**. *LHCC/96-41*, December 1996.

[16] The ATLAS Collaboration. **ATLAS Tile Calorimeter Technical Design Report**. *LHCC/96-42*, December 1996.

[17] The ATLAS Collaboration. **ATLAS Muon Spectrometer Technical Design Report**. *LHCC/97-22*, June 1997.

[18] Y. Arai and J. Christiansen. **Requirements and Specifications of the TDC for the ATLAS Precision Muon Tracker**. *ATLAS Internal Note, MUON-97-179*, May 1997.

[19] M. J. Woudstra. *Precision of the ATLAS muon spectrometer*. PhD thesis, 2002.

[20] C. Adorisio et al.. **Study of the ATLAS MDT Spectrometer using High Energy CERN combined Test beam Data**. *ATL-MUON-PUB-2008-005*, 2008.

[21] ATLAS Computing Group. **ATLAS Computing: Technical design report**. *ATLAS TDR–017, CERN-LHCC-2005-022*, 2005.

[22] R. Brun, F. Rademakers, Ph. Canal, I. Antcheva, and D. Buskulic. *The ROOT Manual 5.16*. http://root.cern.ch/, July 2007.

[23] T. Sjostrand, S. Mrenna, and P. Skands. **PYTHIA 6.4 Physics and Manual**. *hep-ph/0603175, FERMILAB-PUB-06-052-CD-T*, March 2006.

[24] J. Alwall, P. Demin, S. Visscher, R. Frederix, M. Herquet, F. Maltoni, T. Plehn, D. L. Rainwater, and Tim Stelzer. **MadGraph/MadEvent v4: The New Web Generation**. *arXiv:0706.2334*.

[25] F. Paige, S. Protopopescu, H. Baer, and X. Tata. *Manual: ISAJET 7.78 A Monte Carlo Event Generator for pp, $p\bar{p}$ and e^+e^- Reactions*, 2001.

[26] S. Agostinelli et al.. **GEANT4 : A Simulation toolkit**. *Nuclear Instruments and Methods in Physics Research Section A*, **506**(3):250–303, July 2003.

[27] Ketevi A. Assamagan et al.. **Report of the AOD Format Task Force**. *ATL-SOFT-PUB-2006-011; ATL-COM-SOFT-2006-018; CERN-ATL-SOFT-PUB-2006-011*, December 2006.

[28] F. Akesson et al.. **ATLAS Tracking Event Data Model**. *ATL-SOFT-PUB-2006-004*, July 2006.

[29] B. Di Girolamo, B. Dotti, A. Giangiobbe, V. Johansson, P. Pribyl, and L. Volpi. **Beamline instrumentation in the 2004 combined ATLAS testbeam**. *ATL-TECH-PUB-2005-001, ATL-COM-TECH-2005-001*, 2005.

[30] B. Di Girolamo, M. Gallas, and Th. Koffas. **ATLAS Barrel Combined Run in 2004 Test Beam Setup and its evolutions**. *EDMS Note, ATC-TT-IN-0001, EDMS ID:406980*, February 2005.

[31] D. Fassouliotis et al.. **The Wiring of 30.000 MDT-BIS tubes at the University of Athens**. *ATLAS-MUON-PUB-2006-014*.

[32] Th. Alexopoulos et al.. **The Quality Assurance Quality Control of the Monitored Drift Tubes at the HEP Laboratory of the National Technical University of Athens**. *ATL-MUON-2001-019*.

[33] Th. Alexopoulos et al.. **A Quality Assurance and Quality Control (QAQC) Procedure of the Monitored Drift Tubes (MDT) for the BIS-Chambers of the ATLAS Muon Spectrometer**. *IEEE Transactions on Nuclear Science*, **49**:2484–2487, October 2002.

[34] S. Dedousis et al.. **ATLAS muon precision chamber construction at the University of Thessaloniki**. *IEEE NSS-MIC 2000, Lyon, France, 15-20*, pages 5/16–5/20, October 2000.

[35] K. Bachas et al.. **The construction and the quality assurance-quality control of the 112 MDT-Barrel Inner Small precision chambers of the ATLAS Muon Spectrometer**. *Nuclear Instruments and Methods in Physics Research*, **A 581**:198–201, October 2007.

[36] M. Virchaux. **Muonbox: a full 3D tracking programme for Muon reconstruction in the ATLAS Spectrometer**. *ATL-MUON-97-198; ATL-M-PN-198*, 1997.

[37] W Lampl et al.. **Calorimeter Clustering Algorithms : Description and Performance**. *CERN-ATL-COM-LARG-2008-003*, 2008.

[38] M. Aleksa. **private communication**.

[39] D. L. Mateos et al.. **A Bayesian Method for Estimating the Energy Loss of Muons in Calorimeters**. *ATL-COM-MUON-2008-007*, 2007.

[40] K.Nikolopoulos et al.. **Muon Energy Loss Upsteam of the Muon Spectrometer**. *ATL-MUON-PUB-2007-002; ATL-COM-MUON-2006-019*, September 2006.

[41] K.Assamagan et al.. **Muons In Calorimeters: Energy Loss Corrections and Muon Tagging**. *ATL-COM-MUON-2008-009; CERN-ATL-COM-MUON-2008-009, ATLAS CSC NOTE*, 2008.

[42] J. Lindhard. *Mat.-Fys. Medd.*, **28**(8), 1954. Kgl. Danske Videnskab. Selskab.

[43] J. Lindhard et al.. *Mat.-Fys. Medd.*, **33**(14), 1963. Kgl. Danske Videnskab. Selskab.

[44] H. H. Andersen and J. F. Ziegler. **Hydrogen: Stopping Powers and Ranges in All Elements – The Stopping and Ranges of Ions in Matter**. *Pergamon Press, New York*, **3**, 1977.

[45] D. E. Groom, N. V. Mokhov, and S. I. Striganov. **Muon Stopping Power and Range Tables 10 MeV-100 TeV**. *Atomic Data and Nuclear Data Tables*, **78**:183–356, July 2001.

[46] L.D. Landau. *J. Exp. Phys. (USSR)*, **8**, 1944.

[47] F. Bauer et al.. **ATLAS 2004 Combined Test Beam results:Muon Chamber Alignment and Muon Reconstruction**. *ATL-COM-MUON 2006-012*, 2006.

[48] G. Schlager. *The Energy Response of the ATLAS Calorimeter System*. PhD thesis, 2006.

[49] K. Bachas and S. Hassani. **http://alxr.usatlas.bnl.gov/lxr/source/atlas/Reconstruction/RecoTools/TrackInCaloTools**.

[50] A. Salzburger. **The ATLAS Track Extrapolation Package**. *ATL-SOFT-PUB-2007-005*, December 2007.

[51] W. Lampl et al.. **Digitization of LAr calorimeter for CSC simulations**. *ATL-LARG-PUB-2007-011*, November 2007. https://twiki.cern.ch/twiki/bin/view/Atlas/CaloReconstructionTools.

[52] G. J. Gounaris, J. Layssac, and F. M. Renard. **New and Standard Physics contributions to anomalous Z and γ self-couplings**. *Physical Review*, **D62**(073013), October 2000.

[53] R. W. Brown and K. O. Mikaelian. **W^+W^- and Z^0Z^0 pair production in e^+e^-, pp $p\bar{p}$ colliding beams**. *Physical Review*, **D19**:922, February 1979.

[54] B. Mele, P. Nason, and G. Ridolfi. **QCD radiative corrections to Z boson pair production in hadronic collisions**. *Nuclear Physics*, **B357**:409, 1991.

[55] J. Ohnemus. **Hadronic ZZ, W^-W^+, and $W^\pm Z$ production with QCD corrections and leptonic decays**. *arXiv:hep-ph 9403331v1*, March 1994.

[56] L. Dixon, Z. Kunszt, and A. Signer. **Helicity amplitudes for $O(\alpha_s)$ production of W^+W^-, $W^\pm Z$, ZZ, $W^\pm\gamma$, or $Z\gamma$ pairs at hadron colliders**. *arXiv:hep-ph/9803250v1*, March 1998.

[57] J.M.Campbell and R.K.Ellis. **Update on vector boson pair production at hadron colliders**. *Physical Review*, **D60**, December 1999.

[58] L.Dixon, Z.Kunszt, and A.Signer. **Vector boson pair production in hadronic collisions at $O(\alpha_s)$: Lepton correlations and anomalous couplings**. *Physical Review*, **D60**, December 1999.

[59] J. Pumplin, D.R. Stump, J. Huston, H.L. Lai, P. Nadolsky, and W.K. Tung. **New Generation of Parton Distributions with Uncertainties from Global QCD Analysis**. *hep-ph/0201195*.

[60] P. Bartalini, A. Drozdetskiy, A. Korytov, G. Mitselmakher, A. Sherstnev, and H. Stenzel. **NLO vs. LO: kinematical differences for signal and background in the $H \to ZZ^* \to 4\mu$ analysis**. *CMS-NOTE-2006-130; CERN-CMS-NOTE-2006-130*, June 2006.

[61] C.Zecher, T.Matsuura, and J.van der Bij. **Leptonic Signals from off-shell Z Boson Pairs at Hadron Colliders**. *DESY 94-062*, April 1994.

[62] R. Bonciani et al.. **NLL resummation of the heavy-quark hadroproduction cross-section**. *Nuclear Physics B*, **529**(1-2):424–450, September 1998.

[63] S. Frixione, B.R. Webber, and P.Nason. **Matching NLO QCD and parton showers in heavy flavour production**. *JHEP,hep-ph/0305252*, **7**:308, 2003.

[64] B.P.Kersevan and El.Richter-Was. **The Monte Carlo Event Generator AcerMC version 3.4 with interfaces to PYTHIA 6.3, HERWIG 6.5 and ARIADNE 4.1**. *TPJU,hep-ph/0405247*, June 2004.

[65] J.M. Campbell and R.K. Ellis. **An update on vector boson pair production at hadron colliders**. *Physical Review*, **D60**:113006, May 1999.

[66] `https://twiki.cern.ch/twiki/bin/view/Atlas/ElectronReconstruction`.

[67] M. Wielers. **Photon Identification with the ATLAS detector**. *ATL-PHYS-PUB-99-016*, October 1999. https://twiki.cern.ch/twiki/bin/view/Atlas/ElectronReconstruction.

[68] G. Feldman and R. Cousins. **Unified approach to the classical statistical analysis of small signals**. *PHYSICAL REVIEW D*, **57**(7), April 1998.

[69] The ATLAS Collaboration. **Diboson Physics Studies With the ATLAS Detector**. *ATL-COM-PHYS-2008-041, ATLAS CSC NOTE*, 2008.

Acknowledgements

There are not enough words to express how grateful I am to my supervisor Chara Petridou. From the very first moment when, almost 4 years ago, I knocked on her office's door and told her that I wanted to start a PhD, she provided me with endless help and support. Her great research and academic experience and her ability to lead pioneer research in physics not only did it make me feel secure when I was coming accross problems and questions in my work, but it also made me feel that I did the best choice returning back to Greece and starting a PhD in the physics department of AUTH under her supervision. If I could count the hours she has spent answering my questions, explaining things and working with me I'm sure it will sum up to many many months...! And she always did that with the best mood and enthusiasm! I still remember my first visit to CERN and how she introduced me to doing research. I guess it must have been her experience that she knew how to motivate me more and push me to do things I didn't thought I could do! I want to thank her for giving me the opportunity to start and complete this PhD, for her guidance during all these years and for baring my moods especially when I had to give talks. But apart from work, I'm grateful for the trust and the warmth with which she surrounded me all these years, which is really hard to find in a person and I will definitely never forget. I have enjoyed not only working with her but also the innumerable talks, fun times and her friendship. I am really lucky to have been her PhD student. Thank you "dear supervisor"!

It's also difficult to find the words to thank Rosy Nikolaidou for everything she did for me all this time. I'm grateful for the things I learned from her and the work she did for this thesis, a big part of which would not be possible to finish if it wasn't for her. Although when I started this PhD my research experience was practically non-existent, she believed in me probably more than I believed in myself and she supported my efforts in all possible ways. Working with Rosy at CERN was really some of my favourite times during the PhD years. Always willing to hear and help me. She is an excellent physicist, extremely organized and has a fantastic sense of humour. It was a great fortune not only to work with Rosy but also that I had the opportunity to meet her, because apart from all the things I have 'earned' from our collaboration, above all, I have met a wonderful person and 'earned' a real friend.

Thank you "Master"!

I'm also grateful to Samira Hassani. She was the one to introduce me to the world of the ATLAS software providing me with the means to do the work I finally did and sitting by her side I learned things I would have never learned on my own. Her contribution to this thesis is inestimable and many times I followed her wise advices on analysis and code writing which made my life a lot easier. I would also like to thank Samira for all her support, for always being willing to answer stupid questions and for being a person I could always rely on and trust. It was a real pleasure to collaborate with Samira and I'm lucky that apart from a collaborator she has also become a dear friend! Thank you Samira!

I owe many thanks to Ketevi Assamagan first of all for the many times he helped me with TrackInCaloTools providing me magical code snippets that would kill my innumerable bugs and for being such a nice guy to talk to and work with!

I also owe many thanks to my ATLAS group in Thessaloniki for the work we did together but also for creating such a friendly environment which I enjoyed greatly! To Dimos Sampsonidis for his help, friendship and for letting me use his office as if it was my own. To Athanasia Krepouri for her valueable help especially during the first years and for being such a good friend, to the bright young physicist Christos Anastopoulos the best "ice-breaker" in the group, to Electra Christidi who although she joined the group when I was about to finish we did a lot of nice work together in the diboson stuff and to Dimitris Iliadis for the hundreds of fun and serious talks and for becoming a good friend in such a short time! Many thanks to the people in the laboratory of nuclear and particle physics and special thanks to the people in my committee, Tasos Liolios and Professor Mary Zamani.

Many thanks to Jean-Francois Laporte for helping me on various aspects of the work on the testbeam and the athena software. He is really one of the best physicists I've ever met, not to mention that he is also a very kind and cool guy! And also many many thanks to the rest of the Saclay guys for their help, for accommodating me in their CERN office and for the wonderful days I spent in Paris in 2005.

I also need to thank Nektarios Benekos for his help and for the warmth with which he was always treating me when I was at CERN. He is one of the persons that although I didn't know for a long time I always felt really close and appreciate.

Thanks also to Giulio Usai and Tarcisio Del Prete for many useful discussions on the calorimeters.

Starting my PhD was the reason for starting a great friendship with Christos Lampoudis who has become a best friend of mine. We have shared so many times and situations that I don't know what to recall first. The clean-room era, ψηλέ έχει σωλήνες ? The time at CERN, έχεις ψωμί ακόμα ψηλάκη ? The coffee times, or sharing the office in the department? Thank you Christo for being such a good friend and a constant reason for making me laugh!

A huge thanks I need to say to my father and my sister because with their love they supported me especially morally to do this PhD although I have been away physically. And to my dear aunt Mary who is always a reference point in my life.

Last but not least, I am grateful to a wonderful woman. To Dina for her endless love and patience. She has always stood by my side especially during the hard times and my bad moods with remarkable strength and composure and at the same time I was doing my PhD she was also doing her own 'PhD' on supporting and understanding me. This thesis is dedicated to you.

Curriculum Vitae

Konstantinos Bachas

Aristotle University of Thessaloniki

Department of Physics, Nuclear and Particle Physics Laboratory

12454 Thessaloniki

Tel: (+30) 2310-998877

E-mail: Konstantinos.Bachas@cern.ch

Education

- 5/2004 - : PhD thesis
  Aristotle University of Thessaloniki, Greece
  Thesis Title: *Studies of the ATLAS Muon Spectrometer with Testbeam and simulated data*
  Supervisor: Prof. Chariclia Petridou

- 9/2002 - 9/2003: MSc thesis
  The University of Manchester, UK
  Thesis Title: *Studies of Inter-Strip Capacitance in a Silicon Detector*
  Supervisor: Dr.Ian Duerdoth

- 10/1996 - 6/2002: BSc in Physics
  Aristotle University of Thessaloniki, Greece

Work experience

- 1/11/2004 - 30/6/2008 Research Associate - Aristotle University of Thessaloniki

- 1/12/2003 - 30/6/2004 Research Associate - Aristotle University of Thessaloniki

Publications

1. K. Bachas, Ch. Petridou. Drift properties of the MDTs in the H8 Test Beam. ATL-MUON-2005-014; ATL-COM-MUON-2005-002; CERN-ATL-MUON-2005-014, Cern 17 Jan 2005.

2. K.Bachas, S.Hassani, J.F.Laporte, R.Nicolaidou, Ch.Petridou, D.Sampsonidis. Search for catastrophic muon energy losses in combined testbeam data. ATL-COM-MUON-2006-023; Nuclear Physics B (Proc. Suppl.) 177-178 (2008) 320-321

3. K. Bachas et al. The construction and the quality assurance, quality control of the 112 MDT-Barrel Inner Small precision chambers of the ATLAS Muon Spectrometer. Nucl. Instrum. Methods Phys. Res., A 581 (2007) 198-201

4. A. Krepouri, K. Bachas, Ch. Anastopoulos, R. Nicolaidou, Ch. Petridou, D. Sampsonidis, The performance of the ATLAS innermost MDT muon precision tracker in cosmic rays and in positron and muon beams, Nuclear Science Symposium Conference Record, 2006. IEEE, Oct. 29 2006-Nov. 1 2006, Volume: 2, Pages: 1017-1020

5. M. Aleksa, K. Bachas, R. Lafaye, J-F Laporte, R. Nicolaidou, Ch. Petridou, D. Sampsonidis. ATLAS H8 Testbeam data analysis combining information from the Liquid Argon Calorimeter and a Monitored Drift Tube muon tracking chamber. Nucl. Instrum. Methods Phys. Res., A 572 (2007) 117-119

6. C. Adorisio et al. Study of the ATLAS MDT Spectrometer using High Energy CERN combined Test beam Data. ATL-COM-MUON-2007-013. Geneva, CERN, 2007

7. K.Bachas, S. Hassani. Track based software package for measurement of the energy deposited by muons in the calorimeters of the ATLAS detector. Submitted to Journal of Physics Conference Series (JPCS).

8. K.Bachas et al. Diboson physics studies with the ATLAS detector. Nuclear Physics B (Proc. Suppl.) 177-178 (2008) 255-257

9. K. Bachas et al. Diboson Physics Studies With the ATLAS Detector. ATL-COM-PHYS-2008-041, ATLAS CSC NOTE 2008

10. K. A. Assamagan et al. Muons In Calorimeters: Energy Loss Corrections and Muon Tagging. CERN-ATL-COM-MUON-2008-009, ATLAS CSC NOTE 2008

Professional Memberships

- 2007-present. Board secretary of the postgraduate and doctoral student's association of the Aristotle University Physics Department
- 2006-2007. Board member of the postgraduate and doctoral student's association of the Aristotle University Physics Department
- 2004-present. Member of the Hellenic Society for the Study of High Energy Physics

Conferences, presentations and courses attended

Conferences:

- 1st ARTEMIS Annual Meeting, Chalkidiki, Greece, 27-28/9/2007
- CHEP, Victoria, Canada, 2-7/9/2007
  Poster presentation: 'Track based software package for measurement of the energy deposited by muons in the calorimeters of the ATLAS detector'
- Hadron Collider Physics Symposium 2007, La Biodola, Isola d'Elba (Italy), 20-26/5/2007
  Poster presentation: 'Diboson physics studies with the ATLAS detector'
  Poster presentation: 'Studies of catastrophic muon energy losses in ATLAS H8 combined testbeam data'
- Nuclear Science Symposium Conference Record, 2006. IEEE, Oct. 29 2006-Nov. 1 2006: Poster presentation:'The performance of the ATLAS innermost MDT muon precision tracker in cosmic rays and in positron and muon beams'
- X Pisa Meeting on Advanced Detectors, La Biodola, Isola d'Elba (Italy), 21-27/5/2006
  Poster presentation: 'Testbeam BIS Muon Tracking Chamber - Liquid Argon Colorimeter Combined Reconstruction'
- Atlas Physics Workshop, Rome, 6/2005

- HEP Workshop, Giannena, Greece, 13/4/2006
  Oral presentation: 'ATLAS Combined Testbeam - 2004 Muon Detector - Calorimeter combined reconstruction'

- HEP Workshop, Thessaloniki, Greece, 23/4/2004
  Oral presentation: 'First look for catastrophic energy losses of muons with ATLAS Testbeam data'

Presentations:

- Trigger and Physics Week, CERN, 5/6/2007, "Status of TrackInCaloTools"

- Reconstruction Integration Group(RIG), CERN, 30/1/2007, "A tool for energy loss measurement in the calorimeters"

- ATLAS Overview Week, CERN, 5/10/2006: "Results from Muon and Combined Muon Testbeam activities"

- Muon Week, CERN, 5/9/2006: "Status of TrackInCaloTools"

- Muon Week, CERN, 11/4/2006: "Status of the tool for Muon Energy losses in the Calorimeters"

- Software Week, CERN, 4/3/2006: "Update on muon energy losses in the calorimeters"

- ATLAS Week, CERN, 20/2/2006: "A tool for muon energy losses in the calorimeters"

- Physics Week, CERN, 27/10/2005: "First look at BIS chamber data and low energy runs with TileCal-MDT chambers"

- Muon week, CERN 20/4/2005: "Study of the combined H8 2004 data using the Tile-cal and Muon Spectrometer info"

- Testbeam Workshop, CERN 16/12/2004: "t0 and maximum drift time results of barrel MDTs"

- Rutherford Appleton Laboratory, Oxford 15/7/2003: "Time dependence of Inter-Strip Capacitance"
- Many presentations within the Diboson working group meetings
- Some presentations within the Muon Combined Performance and Software group meetings
- Some presentations within the H8 testbeam weekly meetings in summer 2004

Courses:

- European School of High Energy Physics in Aronsborg, Sweden, 18 June - 1 July 2006.